

Oil & Natural Gas Technology

DOE Award No.: DE-FC26-04NT42107

Final Report

Harsh-Environment Solid-State Gamma Detector for Down-hole Gas and Oil Exploration

Submitted by:
General Electric, Global Research Center
1 Research Circle
Niskayuna, NY 12309

Prepared for:
United States Department of Energy
National Energy Technology Laboratory

November 11, 2007



Office of Fossil Energy

Disclaimer

This report was prepared as an account of work sponsored by an agency of the United States Government. Neither the United States Government nor any agency thereof, nor any of their employees, makes any warranty, expressed or implied, or assumes any legal liability or responsibility for the accuracy, completeness, or usefulness of any information, apparatus, product, or process disclosed, or represents that its use would not infringe privately owned rights. Reference herein to any specific commercial product, process, or service by trade name, trademark, manufacturer, or otherwise does not necessarily constitute or imply its endorsement, recommendation, or favoring by the United States Government or any agency thereof. The views and opinions of authors expressed herein do not necessarily state or reflect those of the United States Government or any agency hereof.

Phase II - Final Report:

Harsh-Environment Solid-State Gamma Detector for Down-hole Gas and Oil Exploration

DOE Award Number: DE-FC26-04NT42107

Project Manager (DOE NETL): Gary Covatch

Authors List (GE*): Peter Sandvik (Principal Investigator), Stanislav Soloviev, Emad Andarawis, Ho-Young Cha, Jim Rose, Kevin Durocher, Robert Lyons, Bob Pieciuk, Jim Williams and David O'Connor

Report Period Start Date: November 14, 2005

Report Period End Date: August 11, 2007

*Jim Williams and David O'Connor are with GE Energy's Reuter-Stokes (Twinsburg, OH).
The other authors are with GE Global Research (Niskayuna, NY).

Table of Contents

Table of Contents	4
Table of Figures	5
List of Tables	9
List of Acronyms.....	10
Abstract	11
Introduction	12
1. Task 8 - Fabrication of 4H-SiC APDs for system development	15
1.1. APD Modeling	15
1.2. Design and fabrication of next generation APDs.....	19
1.3. APD dark current analysis	24
1.4. Electrical characterization of APDs	29
1.5. Yield Testing	30
1.6. Optical measurements.....	33
1.7. Materials Studies	39
2. Task 9 - Development of APD arrays and device packaging	41
2.1. Single die with 16 APD devices	41
2.2. APD array of 16 individual dies	42
2.3. Gamma Detector Assembly	49
3. Task 10 - Evaluation of reliability of APD devices	50
4. Task 11 - Development of reflector and optical coupling design	54
5. Task 12 - Development of full crystals of selected scintillator material.....	61
5.1. Optical Modeling Of Scintillators	61
5.2. BaSiO ₄ crystal	62
5.3. Cs ₂ NaPrCl ₆ crystal.....	68
5.4. Lanthanum halide (LaX ₃) crystals.....	73
6. Task 13 - Development of prototype amplification system	79
6.1. APD signal model	79
6.2. Electronics Architectures	81
7. Task 14 - Assembling and evaluation of full detector system	85
8. Task 17 - Suggestions and recommendations for improving performance of the APD gamma sensor	91
Appendix A - Phase II Statement of Work	94
Appendix B – List of Publications	97

Table of Figures

Figure 1. At left, data reported by the USA Today (10-17-05). At right, an estimate of the temperature incurred while drilling versus local temperature gradient.	12
Figure 2. Gamma sensor system concept.	13
Figure 3. Geometric layout of the mesa structure from iteration 1 and 2 APDs (left), and the electrical field profile as simulated in Silvaco (right).	15
Figure 4. Simulated electric field profile for two SiC APDs using ATLAS.	16
Figure 5. Simulated I-V relationships (left) for two structures (right).	17
Figure 6. Absorption coefficient plot for SiC taken from Xiangyi Guo's PhD dissertation, University of Texas at Austin, 2005.	18
Figure 7. The quantum efficiency model results for the initial APD structure. At left, the QE components from the various layers and at right, the calculated responsivity.	19
Figure 8. Summary figures showing the Gen III APD design.	20
Figure 9. Cross-section of new APD structure.	21
Figure 10. Illustration of a cross-sectional view of SiC APD Gen III.	21
Figure 11. SEM images of SiC APDs (upper left corner of the device) after being exposed to electrical arcing at high applied voltages.	23
Figure 12. Current-voltage relationships for various sized APDs (left) and from 1x1 mm ² devices located in the center, middle and edge of the wafer. These devices were fabricated in iteration 2 (task 5) of phase I.	24
Figure 13. Blocking voltage histogram of the 268 tested devices of 1 mm sq in size.	
Figure 14. Current-voltage (I-V) measurements on a iteration 2 SiC APD as a function of temperature.	25
Figure 15. Leakage current at 1000 V as a function of device size.	26
Figure 16. Leakage current at 400 V as a function of device size.	26
Figure 17. Variation in leakage currents for APD with the same size (750 μm on a side).	27
Figure 18. EBIC image of single APD	27
Figure 19. (a) EBIC signal line-scans and (b) 3D-image reversal map of EBIC signal intensity normalized.	28
Figure 20. Correlation between defect densities and leakage currents.	28
Figure 21. EBIC images and corresponding surface images after KOH etching taken at different regions.	29
Figure 22. Capacitance voltage characteristics for SiC APDs with an area of 5.54 x 10 ⁻³ cm ² (left) and the voltage versus 1 over capacitance squared (right).	30
Figure 23. Yield distribution of 10 nA voltages in the HM-19 wafer (1 mm ² quadrant).	31
Figure 24. Yield distribution as shown in Figure 23 in greater detail.	31
Figure 25. Leakage current measurements, showing current versus reverse bias of Gen III APDs (left) and photocurrent measurements at different wavelengths (right)...	32
Figure 26. I-V characteristics of 500 by 500 micron APDs from the Gen II (left) and Gen III (right) iterations.	33

Figure 27. Quantum efficiency of GE's SiC APD L7-29 (iteration 2) as measured by the team of Prof. Joe Campbell.....	34
Figure 28. Gen II (left) and Gen III (right) APD measurements of quantum efficiency versus wavelength (nm).....	35
Figure 29. Leakage and photocurrent vs. temperature of 1x1 mm ² APDs.....	35
Figure 30. Zoomed in breakdown curve of dark current against temperature for (a) 1x1 mm ² and (b) 0.75x0.75 mm ² APDs.....	36
Figure 31. Responsivity as function of wavelength and temperature for a yielded SiC APD. The quantum efficiency levels are shown in the dotted lines.	37
Figure 32. Band structure of 4H SiC after Ref.	38
Figure 33. Optical photo of the APD under test (left) and under reverse bias (right).....	39
Figure 34. Luminescence as a function of wavelength from the diodes, after forward biasing at levels shown in the inset.	40
Figure 35. Quarter wafer with arrays showing pass/fail results. The upper left is the center of the wafer.	42
Figure 36. Kapton film on a frame showing several different array designs. In the center, two array designs have been successfully populated with SiC APDs.	43
Figure 37. A photograph of a 4x4 SiC APD array packaged using the flex process described above. A quarter shows the size of the disk, which has a 1 inch diameter.	45
Figure 38. APD array sub-mounts from the first iteration ('gen 1'). Various metals as well as various layout geometries were prototyped to make the process as robust as possible.....	46
Figure 39. Gen 2 APD sub-mount build, showing several arrays on a Kapton frame. At left, the front side is shown, while the back-side is shown at right.	47
Figure 40. Magnified pictures of the radial "snowflake" layout (shown above) and the rectangular grid layout (below).	48
Figure 41. Concept figure of the third generation sub-mount build, showing the flex interposer, which connects the array to the electronics board for integration to the gamma sensor prototype.....	49
Figure 42. Dark Currents of individual APDs on Sub-Mount with Flex Board.	50
Figure 43. APD reliability testing, showing the APD electrical properties as a function of time.	51
Figure 44. APD reliability testing using multiple I-V sweeps at room temperature.	51
Figure 45. APD reliability testing at 200 °C. Here, 200 I-V cycles were performed over a ~15 hour period.	52
Figure 46. Testing of APDs showing the voltage (left) and current (right) levels as a function of time.	53
Figure 47. Currents of five APDs tested at 220°C for 400 hours.	53
Figure 48. Current of selected APD tested at 220°C for 1,400 hours.	54
Figure 49. Tool designed to realize thin films of optical coupler materials for study.	55
Figure 50. UV transmission of several candidates before exposure to high temperature.	56
Figure 51. Material A at 0 (left) and 24 (right) hours of exposure to 225 °C in air.	57

Figure 52. Transmission characteristics of the optical coupler candidates after various times at elevated temperature in air.....	58
Figure 53. The transmission of the Dow optical gel is shown as a function of wavelength.	59
Figure 54. Optical transmission of an optical gel as a function of wavelength. The red curve is of a blank substrate (reference) and the blue and black curves are of two actual samples.	60
Figure 55. At left, the substrate with APDs (4x4 array) surrounded by the UV reflective coating. At right, the reflectance versus wavelength for the Al-coating.....	60
Figure 56. Scintillator shape components (left) and features (right) that were explored in various models to study their effects on light extraction.....	61
Figure 57. Picture of BaSiO ₄ crystal growth from the CUNY sub-contract team.	63
Figure 58. Light output of scintillator materials that are presently a backup for BaSiO ₄ material.....	63
Figure 59. Comparison of scintillator materials, including the "alternative" material, which is a backup to Ba ₂ SiO ₄	64
Figure 60. Figures from CCNY - CUNY showing progress with BaSiO _x growth.	65
Figure 61. Optical properties of Ba ₂ SiO ₄ . Transmission shown in the top graph, and a corresponding plot of the emission spectra on the bottom. The x-axis is in nanometers.....	67
Figure 62. Optical reflectance of the barium orthosilicate material versus wavelength (nm).....	68
Figure 63. Ball and stick model of Cs ₂ NaPrCl ₆	68
Figure 64. Emission intensity as a function of wavelength for Cs ₂ NaPrCl ₆ , as reported in Physical Review B, volume 67, article 115102 (2003).	69
Figure 65. Photo of the initial trial growth of Cs ₂ NaPrCl ₆ . The adjacent rule has units of inches.	69
Figure 66. Optical properties of Cs ₂ NaPrCl ₆ . The red line shows absorption data while the blue line shows emission spectra from a 254 nm source.	70
Figure 67. Relative light output, integrated from 250 to 400 nm, for Cs ₂ NaLa _{1-x} Pr _x Cl ₆ as a function of Pr/La mole fraction.	71
Figure 68. Pulse height spectrum of Cs ₂ NaPr _{0.4} La _{0.6} Cl ₆ excited with ¹³⁷ Cs (at left), and with excited with ²² Na (right).	72
Figure 69. Scintillator testing setup used for elpasolite materials study.	73
Figure 70. LO measurement of Cs ₂ NaPr _{0.4} La _{0.6} Cl ₆ relative to BaF ₂ for 662 keV.	73
Figure 71. LaX ₃ sample compounds light output intensity as a function of wavelength. Some of the properties of this material are compared with the presently used NaI in the subsequent figure.	74
Figure 72. quantum efficiency spectra of LaCl ₃ and LaBr ₃ crystals.	75
Figure 73. Quantum efficiency multiplied by gamma ray absorption factor for 1/2 inch crystal.....	76
Figure 74. Product of QDE*QE*Absorption in .5 in crystal at 700 KeV.	76
Figure 75 QDE*QE*absorb*photons/MeV for 1/2 inch dia. by 1/2 inch long crystal.....	77
Figure 76. 230 C QDE*QE* photons/MeV*absorption factor	78

Figure 77. Light output of LaBr ₃ crystal within a band of 320-380 nm.....	78
Figure 78. Equivalent noise charge (in electrons) versus the shaping time (in seconds) on the y and x-axis, respectively.....	81
Figure 79. Signal conditioning block diagram.....	82
Figure 80. Circuit simulation of the above arrangement.....	83
Figure 81. Four arrangements realized in hardware form for testing with an oscilloscope.....	84
Figure 82. Amplification electronics output in response to a pulse generator.....	84
Figure 83. Schematic drawings of set-up for an optical test.....	85
Figure 84. (a) photograph of APD array mounted on the electronic board, (b) scope image of dark counts.....	86
Figure 85. Dark current and optical gain curves of the APD array vs. applied voltage. ...	87
Figure 86. Optical responses of the APD array to the laser pulses.....	87
Figure 87. Optical responses of the APD array to the laser pulses at different optical gains.....	88
Figure 88. Top view of gamma sensor prototype.....	88
Figure 89. Reverse side of prototype, external wiring attached.....	89
Figure 90. Completed gamma detector in housing.....	90
Figure 91. I-V curves of packaged Array 016-M5, before and after housing.....	90
Figure 92. Schematic drawings of an experimental set-up for testing the gamma detector.....	91
Figure 93. APD responsivity and LaBr _x crystal emission spectra.....	91
Figure 94. Slide from CREE presentation at last ICSCRM meeting on October, 19 2007 demonstrating development of SiC substrate with a low defect density.....	93
Figure 95. Dark counts and Signal pulse amplitude distribution.....	93

List of Tables

Table 1. Summary of wafers used in the Gen III APD lot.	22
Table 2. Summary of the materials under study for optical coupling.	56
Table 3. Summary of scintillator modeling of various features as shown in Figure 56... ..	62
Table 4. Compositional analysis of the barium orthosilicate samples from CUNY.	66
Table 5. Table of some scintillator properties of LaX_3 materials doped with Ce compared to NaI.....	74
Table 6. Summary of input parameters to the electronics model.....	80

List of Acronyms

APD - avalanche photodiode

CPS - counts per second

EBIC - electron beam induced current

EDX - electron dispersive x-ray

ENC - electronic noise charge

ICP-RIE - inductively coupled plasma enhanced reactive ion etching

MWD - measurement while drilling

MOCVD - metalorganic chemical vapor deposition

NaI - sodium iodide

OWD - oil well drilling

PET - positron emission tomography

PMT - photomultiplier tube

SAM - separate absorption and multiplication

Si - silicon

SiC - silicon carbide

SIMS - secondary ion mass spectrometry

WBG - wide bandgap

UV - ultraviolet

Abstract

The goal of this program was to develop a revolutionary solid-state gamma-ray detector suitable for use in down-hole gas and oil exploration. This advanced detector would employ wide-bandgap semiconductor technology to extend the gamma sensor's temperature capability up to 200°C as well as extended reliability, which significantly exceeds current designs based on photomultiplier tubes. In Phase II, project tasks were focused on optimization of the final APD design, growing and characterizing the full scintillator crystals of the selected composition, arranging the APD device packaging, developing the needed optical coupling between scintillator and APD, and characterizing the combined elements as a full detector system preparing for commercialization. What follows is a summary report from the second 18-month phase of this program.

Introduction

This report highlights progress made in the second phase of the Down-Hole Gamma Sensor program, as performed by General Electric. The first 18-month phase progress has been detailed in a sister report, and those results and progress are not repeated here.

The goal of this program was to develop a revolutionary gamma sensor system, capable of long-term operation at temperatures up to 200 °C and above for long durations. The need for such a system is explained by the Department of Energy's Deep Trek initiative¹, which is aimed at the development of new technologies to aid in oil exploration in more remote, harder to reach locations around the world. Recent data shows important figures, attesting to the need for more robust, down-hole drilling technology as shown in Figure 1.

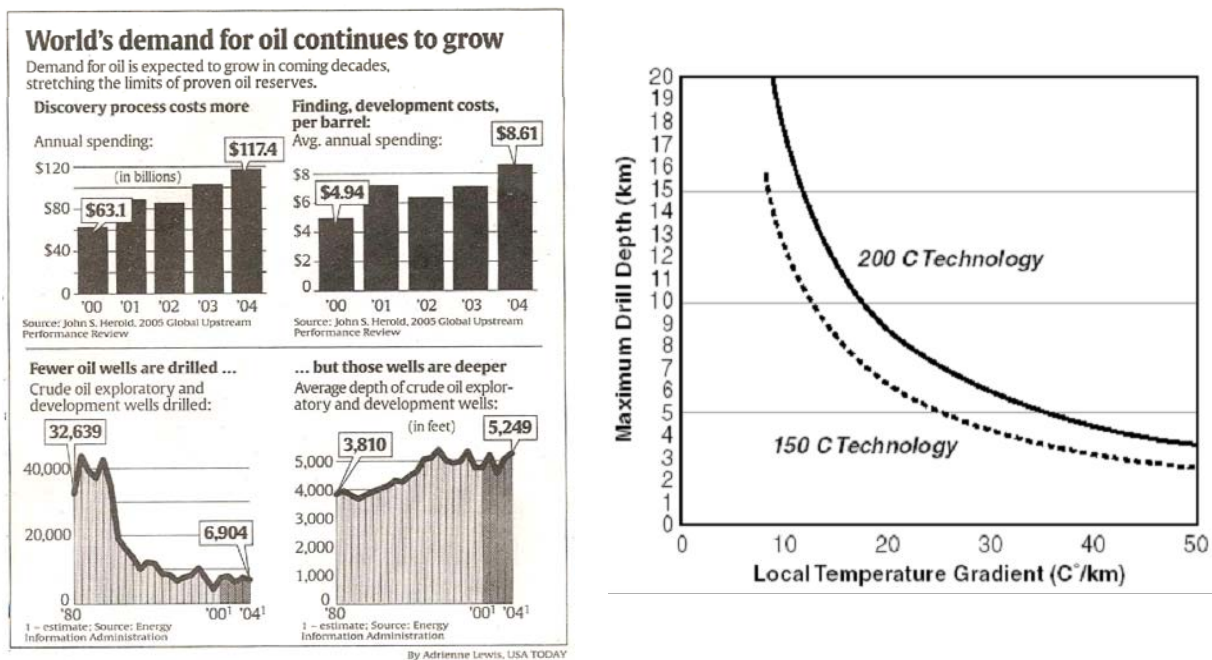


Figure 1. At left, data reported by the USA Today (10-17-05). At right, an estimate of the temperature incurred while drilling versus local temperature gradient.

As shown in Figure 1 at the left, the average depth of exploratory wells has grown over 1,000 feet over the past 25 years, a trend which is expected to continue. While each

¹ http://www.netl.doe.gov/technologies/oil-gas/E&P_Technologies/AdvancedDrilling/DeepTrek/

well location may have a different temperature dependency as a function of depth, a general rule of thumb may be applied in which the temperature increases with depth roughly between 10 and 50 °C/1,000 meters. In Figure 1 at the right, a comparison of maximum drill depth is shown between two different technologies with capability to operate at 150 and 200 °C. An operating temperature increase of just 50 °C would enable substantially deeper drilling.

To help visualize the gamma sensor that was developed, a graphic was prepared that illustrates one version. This is shown in Figure 2.

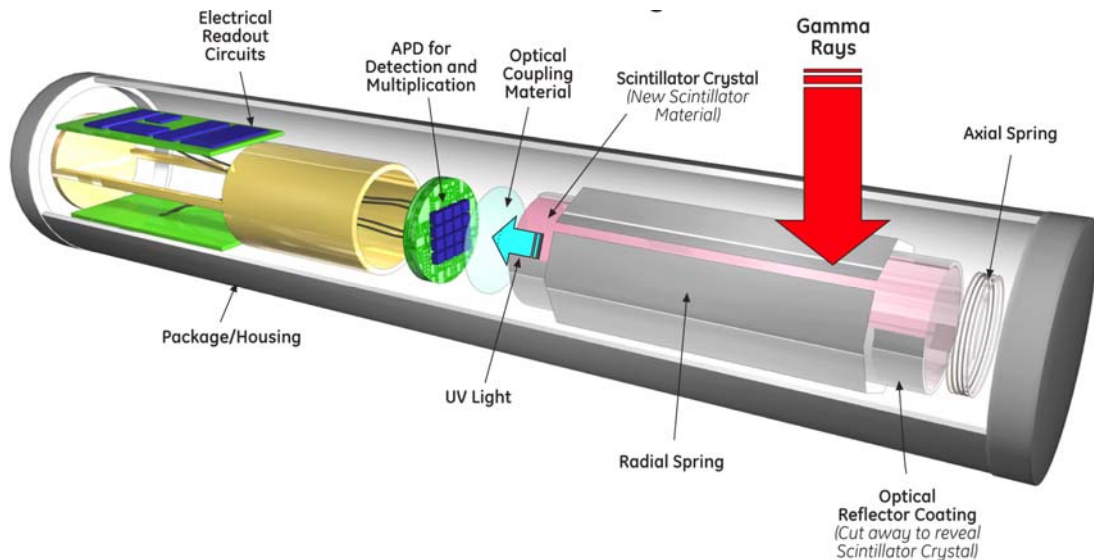


Figure 2. Gamma sensor system concept.

Here, the scintillator is shown on the right as a cylinder. Axial and radial springs are used in the current product to help hold the scintillator in place. Surrounding the scintillator is a thin sheet of teflon, which helps prevent UV light generated in the scintillator from escaping into the package and being lost before collection in the APDs. Optical coupling material, shown between the scintillator and the APD array will help reduce losses by reducing the change in index of refraction going through the various media. An array of APDs is shown with amplifying electronics on the other end, with appropriate packaging to support its operation in high temperatures.

In Phase 2, two GE groups continued to develop this new gamma sensor system together, GE Global Research (Niskayuna, NY) and GE Reuter-Stokes (Twinsburg, OH), the latter a company that sells gamma sensor systems and other down-hole equipment to exploration companies. The Phase 2 Statement of Project Objectives for this project is included as Appendix A.

What follows in this report is a task by task description of the Phase 2 work done over the 18-month contract period, with the three month no-cost extension.

Questions regarding this report and/or project should be directed to Peter Sandvik at GE Global Research via (518) 387-4166 or sandvik@research.ge.com.

1. Task 8 - Fabrication of 4H-SiC APDs for system development

This task (Task 8 in the Statement of Project Objectives) followed directly from the progress made in Task 5 of Phase I. Optimizing the device design and fabrication process, the team continued to evaluate the Iteration 2 APDs to benchmark the yield as well as delineate surface from bulk leakage current.

1.1. APD Modeling

An additional activity was the modeling of APD structures using a software package called Silvaco. This program uses a finite element approach to simulate the electric field profile in a chosen mesa structure. An example of this is shown in Figure 3. The colors show the electric field level, with the axes in microns. It is noted that in the above model, a 10 micron thick SiO₂ layer has been added above the entire mesa.

This simulation is useful as a variety of semiconductor parameters may be modified in order to better understand the nature of the leakage current observed in devices. In particular, Figure 3 illustrates that at the corner of the mesa where the beveled edge meets the vertical portion of the sidewall, the electric field raises quickly (as shown by the red region). According to the model, the mesa may be subject to early breakdown close to the surface, lowering the signal to noise performance of the device.

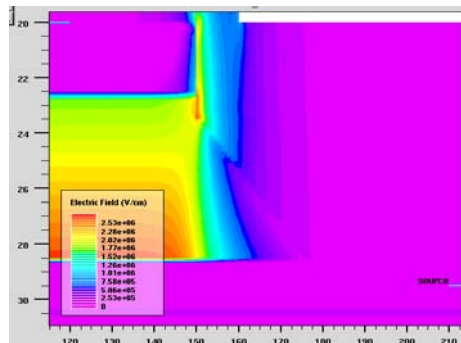


Figure 3. Geometric layout of the mesa structure from iteration 1 and 2 APDs (left), and the electrical field profile as simulated in Silvaco (right).

In the next generation of APDs, the structure was redesigned in order to eliminate the corner feature by modifying the doping profile in such a way that the electric field at the corner is very low ($\ll 1$ MV/cm).

One of the key challenges was the selection of a ~ 5 micron thick structure that should result in low noise. The reason for the reduction in thickness in the design is due to the

surprisingly high electric field profiles predicted by the model in our present design APDs. Figure 4 shows a comparison of the electric field profile near a breakdown voltage of a partially beveled and fully beveled mesa for the same epitaxial structure shown in Figure 3. The simulations compare two separate absorption, charge and multiplication (SACM) region devices at 1100 V reverse bias with a partially beveled (left) and fully beveled (right) sidewall.

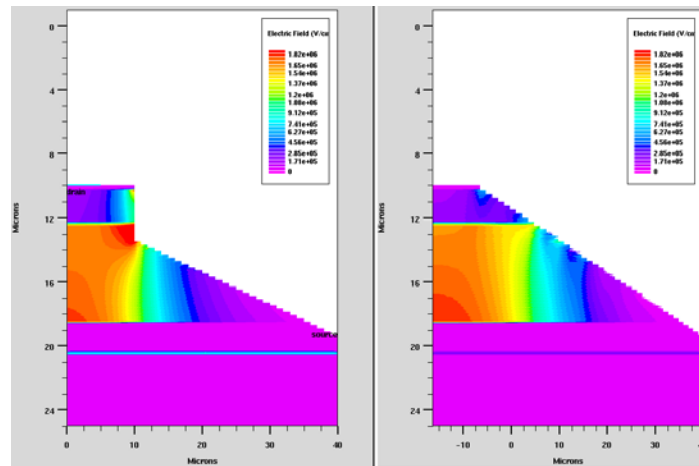


Figure 4. Simulated electric field profile for two SiC APDs using ATLAS.

From the figure, it is readily observed that near the transition from the beveled edge to the vertical edge (at left), the electric field is very large, near 2 MV/cm. While this does not ensure poor device performance, the high field if sustained over time may result in physical degradation to the surface of the devices, and therefore the dark current in the APDs. In comparison, the fully beveled structure (at right) has a greatly reduced field near the edge of the mesa.

The thicker APD structure affords a lower device capacitance and better physical separation of the APDs. However, it was found from Phase I experiments on very thick, SAM structure devices, even in devices with low surface leakage, the absorption layer of the device is likely fully depleted, leading to higher leakage currents.

From Figure 12, it can be seen that breakdown in the device is observed at a reverse bias of ~ 1250 V, which is in good agreement with the MathCAD analytical model discussed in the Phase I Final Report. However, there is a large increase in dark current well before breakdown, starting at approximately 600 V. It is suspected that this is related to the reach-through voltage of the device. This is the voltage at which the absorption layer becomes depleted, and the ensuing current becomes substantially larger, in this case likely leading to a high level of dark current.

Reach-through is therefore not desired, especially when the minority carrier diffusion length in the absorption layer is sufficiently larger than the thickness of the layer. In that case, photogenerated carriers should diffuse on their own into the charge layer, and be swept up towards the multiplication region.

As this total structure is approximately five microns in thickness, the entire mesa can be beveled during the fabrication, thereby mitigating the risk of high electric fields near the transition of the mesa from angled to vertical sidewall.

It is also noteworthy to mention perhaps the most important layer with respect to the structure's breakdown and reach-through voltage sensitivity is the charge layer. As an illustration of that, Figure 5 shows a comparison plot of the expected current-voltage relationship. The red and blue I-V curves correspond to the two structures, reach-through (R.T.) and non R.T., respectively.

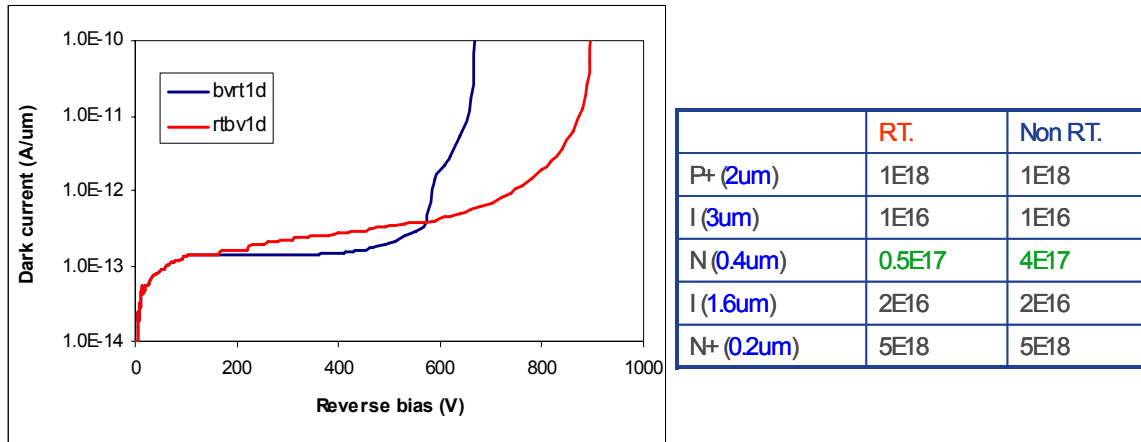


Figure 5. Simulated I-V relationships (left) for two structures (right).

While there is a major change in the breakdown voltage, the general shape of the I-V curve before breakdown is the most important feature for comparison. For the reach-through structure (shown in red), a large increase in current is expected prior to breakdown as the absorption layer depletes.

Another important consideration when arriving at the epitaxial structure shown in Figure 3 was the thickness of the absorption layer. While a thick absorption layer is desired to ensure complete collection of the photons in the range of interest, a thinner layer will lend itself more readily towards a fully beveled mesa. The past structure used a two micron thick absorption layer, and resulted in reasonable quantum efficiency at ~300 nm as shown in Figure 27. At a first glance, given the absorption coefficient of 4H SiC as shown in Figure 6, a reduction of 0.5 μm in thickness should not lead to a significant reduction in the absorption and therefore quantum efficiency of the devices.

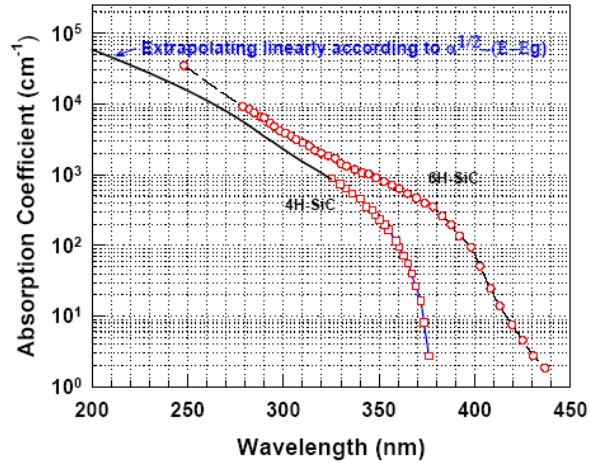


Figure 6. Absorption coefficient plot for SiC taken from Xiangyi Guo's PhD dissertation, University of Texas at Austin, 2005.

Models developed for a QE estimation included one-dimensional continuity equations for minority carriers and photocurrent generation in the depletion region. The estimated optical characteristics as a function of wavelength are shown in Figure 7. A maximum quantum efficiency of 60% and a maximum responsivity of 140 mA/W were calculated at a wavelength of approximately 300 nm.

Wafers for the third generation of APDs were purchased from both Cree Research (Durham, NC) and Intrinsic (Dulles, VA). To confirm the epitaxy layer thickness and doping levels were in agreement with those specified in the order, secondary ion mass spectrometry (SIMS) was performed, which makes measurements of the type and concentration of the atoms in the tested material. Taking the doping profile, the home-built model described in earlier reports was used to predict the profile of the electric field, as shown on the top. For a peak electric field of ~ 2.3 MV/cm, calculated values are: a capacitance of ~ 30 pF, a gain of ~ 185 , an excess noise factor of 7.6 and an ionization coefficient of 0.03.

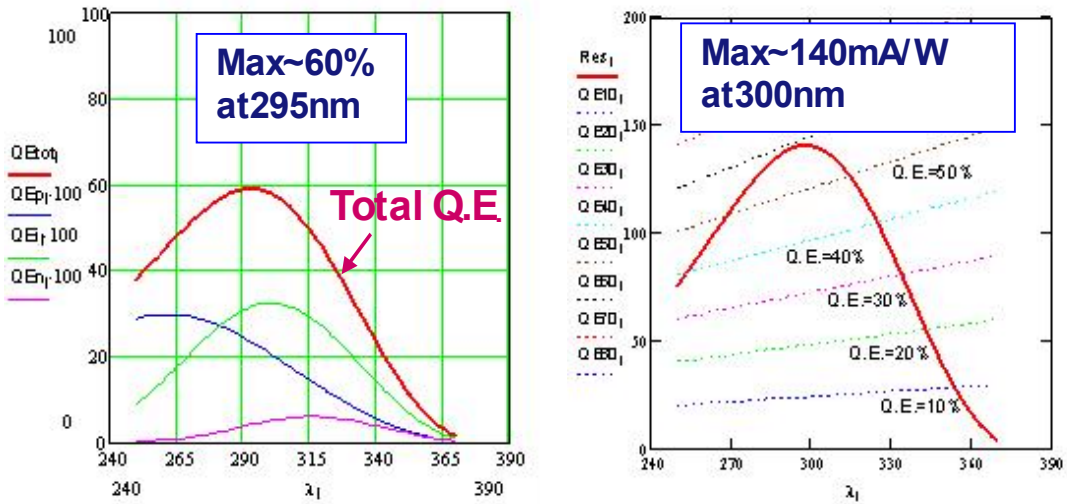


Figure 7. The quantum efficiency model results for the initial APD structure. At left, the QE components from the various layers and at right, the calculated responsivity.

1.2. Design and fabrication of next generation APDs

The design layouts of the APDs are summarized in Figure 8. The top left shows the wafer level layout of the features, the top right shows a single APD, the bottom left shows the APD array feature and the bottom right shows the test element features.

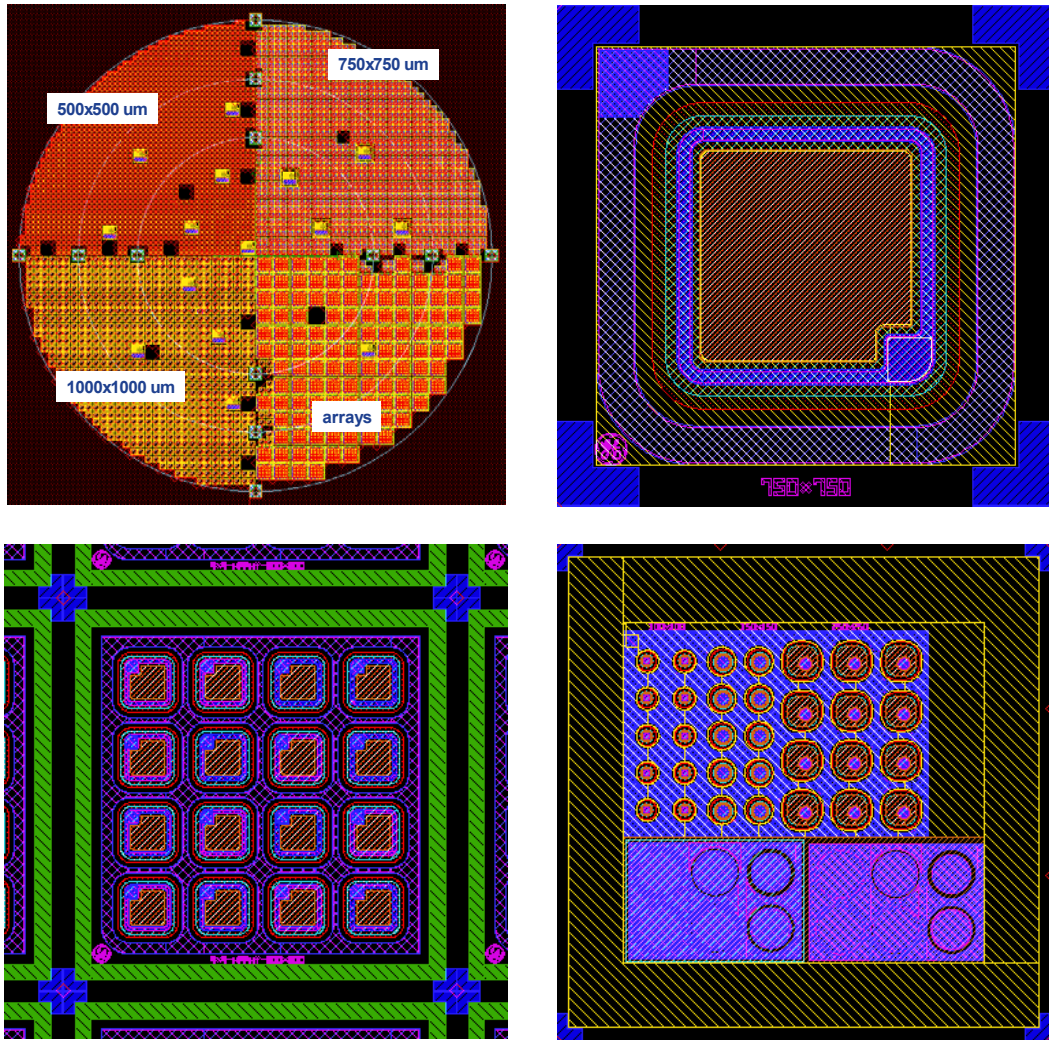


Figure 8. Summary figures showing the Gen III APD design.

The design of the Gen III APDs was modified from previous versions in a couple of important ways. First, the total thickness of the epitaxial layers was reduced for two reasons: to decrease the breakdown voltage to <800 V and to eliminate the vertical mesa sidewalls surrounding the depleted space charge region. Second, in order to reduce the slope angle of the mesa sidewalls, $\delta < 10^\circ$, the radius of the mesa structure was expanded to 35 microns as suggested by results of experiments performed earlier. Third, the distance between the p-contact edge and the edge of the passivation layer, a , was increased up to 20 microns in order to eliminate possible arcing effect. These modifications are illustrated with the help of Figure 9.

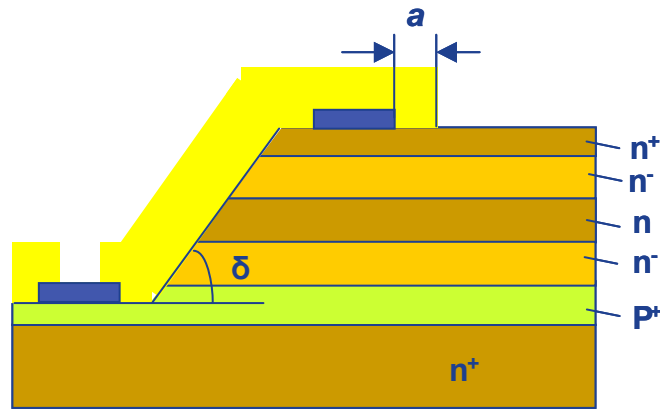


Figure 9. Cross-section of new APD structure.

A cross-sectional view of a completed APD is illustrated in Figure 10. The actual opening on the pad metal for n-contact is located in the opposite edge of the device to maximize the distance from the opening on p-contact.

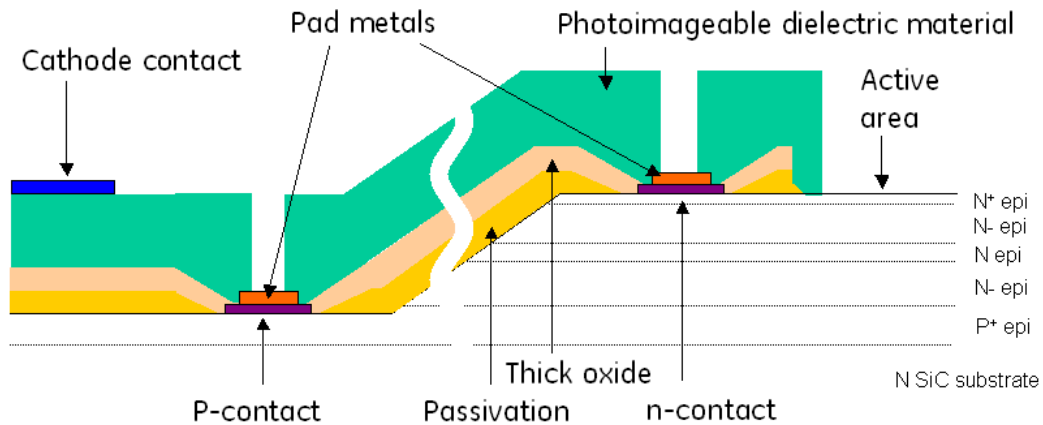


Figure 10. Illustration of a cross-sectional view of SiC APD Gen III.

To support this fabrication process and the modifications involving new steps, short loop experiments were performed to validate new processes. The first short loop (SL.086) was to verify that Ar pretreatment can be incorporated into ICP etch. It was suggested that Ar pretreatment could improve the etched surface by suppressing the micromasking problem (see Phase I Final Report). Since the etch rate of photoresist

mask was critical in our etch process, the etch rate of photoresist during Ar pretreatment was found from this short loop. The second short loop (SL.087) was to verify conditions for metal deposition on top of photoimageable dielectric material.

The fabrication of the third iteration of silicon carbide (SiC) avalanche photodiodes (APDs) was completed. Table 1 shows the wafers used.

Table 1. Summary of wafers used in the Gen III APD lot.

Wafer #	Substrate	Epi-layers	Type	Doping	Thickness
HM-19	4H-SiC, n-type, Research grade, 3" dia., 8 deg off-axis, .015-.028 ohm-cm, Low Micropipe Grade (<15 μ pipes/cm ²), both sides polished, with five layers of epi	epi 1	p-type	2e18	2 microns
		epi 2	n-type	7.5e15	2.7 microns
		epi 3	n-type	4e17	0.45 microns
		epi 4	n-type	7.5e15	1.35 microns
		epi 5	n-type	4e18	0.2 microns
HM-21	same as above	as provided, the same as above			
HM-05	CREE substrate 4H-SiC, 8 deg off, 3" dia, with GE epi	epi target was the same as above			
AH-06 SY	SiCrystal substrate 2" dia, 4H-SiC 8 deg off, with GE epi	epi target was the same as above			

Some issues that arose during fabrication include:

1. One of the 2-inch wafers with GE epitaxy failed during the ICP etching process as the etch rate was much higher than expected. Initial surface roughness differences from the other wafers could be a possible explanation, which was about +/-0.1 μ m as measured vertically. Another difference in that wafer was its smaller diameter (2 inches), while all other wafers, including the dummy wafer, were 3 inches in diameter. This second difference in diameter is important as different chucks are used in the ICP procedure for these different sized wafers, and likely influence the plasma properties significantly. To address this problem, in the future, the same size sacrificial SiC wafer may be used in order to adjust ICP etching conditions.
2. While the p-type contacts had a low-resistance as desired, the n-type contacts showed rectifying characteristics. The contact resistance and specific contact resistivity of the p-type contacts were <20 Ω -mm and <4 Ω -cm², respectively, with a sheet resistance of ~10000 Ω /□. Re-annealing using two RTA systems did not improve the n-type contact behavior. It was suspected that there might have been a thin oxide layer between the n-type contact metals and the SiC surface. We therefore attempted to remove the contact metals, however, as this was unsuccessful, the process was continued without further treatments. It should not pose a significant problem under high reverse biases, however.

3. The HM-05 wafer fell inside the sputtering tool due to a mechanical malfunction and was broken into two pieces. Only the larger piece was continued in the process.
4. Metal adhesion on a thick dielectric layer was tested in a separate short loop experiment. The first two trials at this resulted in the metal pads lifting off during a wire bonding process and thus a new short loop will be performed to solve it.

Two wafers, HM-19 and HM-21, were then cut into four quarters. The quarters with APD arrays went back to the cleanroom for an additional metallization step while other pieces with single APDs were tested on automatic probe station for selecting “good” devices to be packaged.

Scanning electron microscope (SEM) studies of our earlier made devices which have been subjected to electrical arcing from high applied voltages (> 800 V) show consistent failure in a particular part of the device as shown in Figure 11.

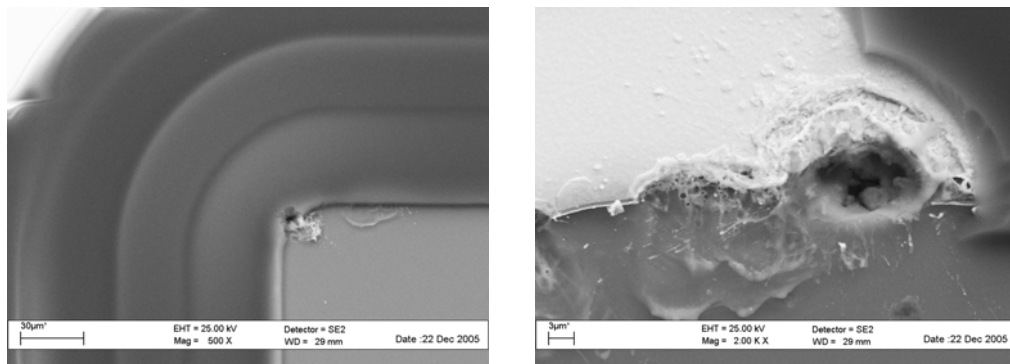


Figure 11. SEM images of SiC APDs (upper left corner of the device) after being exposed to electrical arcing at high applied voltages.

Here, arcing regularly damaged the upper left hand corner of the devices, following the path of shortest distance between the p-type contact pad and the top of the mesa. To address this issue, two changes in the devices were implemented. First, a very thick (>10 μm) photoimageable dielectric material will be deposited over the sidewall of the mesa in order to enhance the passivation in the most critical areas. Second, the device was enlarged in such a way that the lateral distance between the electrodes was increased. Those changes, along with a thinner epitaxial design eliminated this issue, which was described in more detail in the Phase I Final Report.

1.3. APD dark current analysis

Figure 12 shows two plots of several APDs' current-voltage measurements. At the left, several different size devices were measured and predictably, the smaller the device, the lower the leakage current that was observed. At right, three representative devices were measured from the center of a SiC wafer, the middle (radius-wise) and the edge of a wafer. These three parts highlight the likely minor variations in epitaxial doping and thickness across the wafers' diameter, which impact the breakdown voltages observed. An excellent summary work that explored this issue for SiC APDs is available from Guo et al.²

Distribution of blocking voltages measured at 10 nA is shown in Figure 13. This histogram indicates that a total yield of APD devices with an area of 1 mm² demonstrated avalanche behavior was more than 70%.

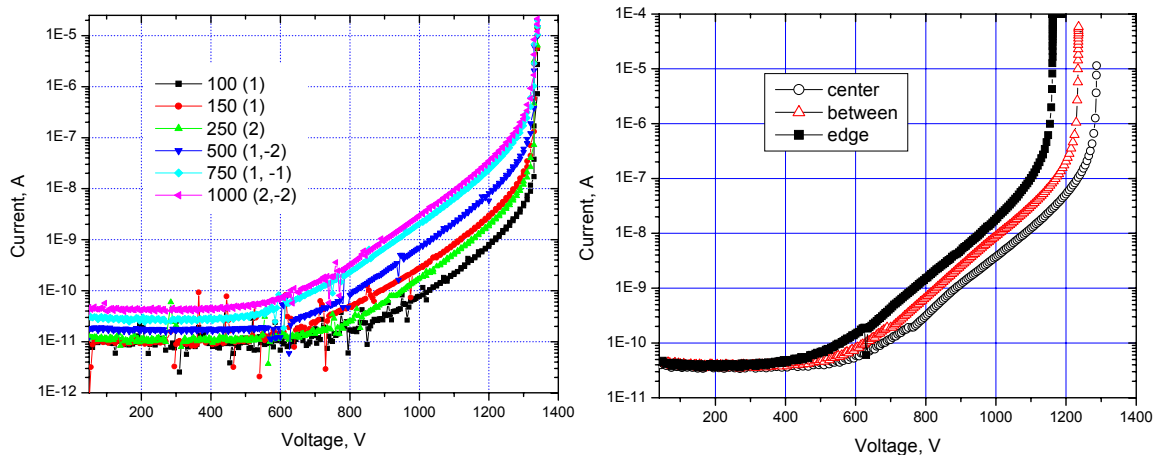


Figure 12. Current-voltage relationships for various sized APDs (left) and from 1x1 mm² devices located in the center, middle and edge of the wafer. These devices were fabricated in iteration 2 (task 5) of phase I.

The dark current in the devices also varies as a function of temperature, in a manner consistent with the behavior observed in past works for 4H SiC.^{3,4} Figure 14 shows at least two important features. First, the lower voltage leakage, consistent with what's shown for voltages of 1100 and below, increases with increasing temperature. While this is to be expected as higher temperatures result in larger numbers of free carriers, an important test is what occurs to the current at voltages closer to the breakdown (near 1200 V below). In this case, the breakdown voltage is shifting to higher voltages with increasing temperatures, suggesting that scattering in the semiconductor plays an important role. This is desirable as these devices will need to operate at high

² Guo et al., *IEEE J. of Quant. Elect.*, 41, p. 1213, 2005.

³ Burr et al., *Proc. of MRS Fall Meeting*, 742, K7.8, 2002.

⁴ Konstantinov et al., *App. Phys. Lett.*, 73, p. 1850, 1998.

temperatures. If the breakdown were to decrease with increasing temperature, the current in the APDs would be subject to large spikes thereby forcing much more difficult performance from the amplifying electronics that will be connected to the APDs.

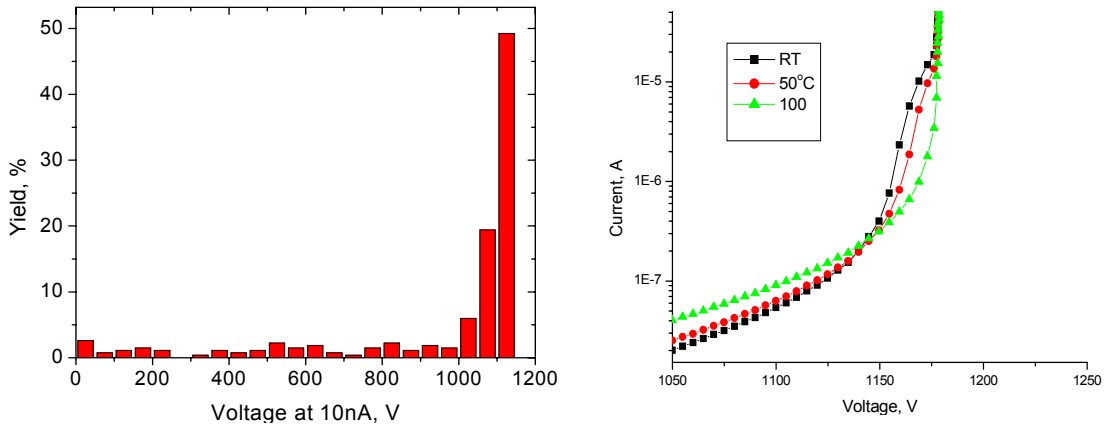


Figure 13. Blocking voltage histogram of the 268 tested devices of 1 mm sq in size. Figure 14. Current-voltage (I-V) measurements on a iteration 2 SiC APD as a function of temperature.

Continued current-voltage (I-V) studies were leading towards an attempt to find a statistical relationship between current levels as a function of area and periphery dimensions.

Analysis of the leakage current as a function of device size showed that the bulk leakage component is dominant at $U > 600V$ (see Figure 15) since the measured data fit a second order curve, while surface leakage is dominant at $U < 600V$ (see Figure 16) since the measured data fit a linear curve. Modeling of the electric field distribution for given structure suggested that at a reverse bias of $\sim 600V$, a depletion region in the absorption layer reached the cap layer. This may be associated with the significant increase in leakage current at $> 600V$.

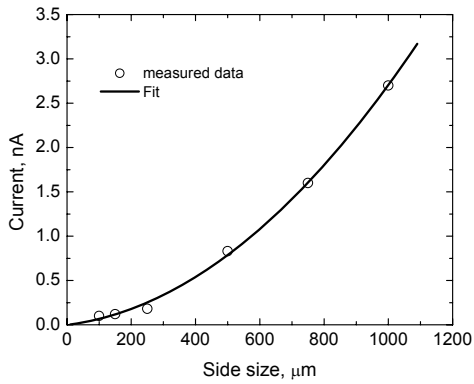


Figure 15. Leakage current at 1000 V as a function of device size.

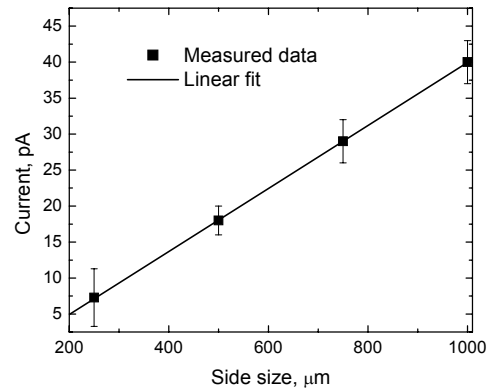


Figure 16. Leakage current at 400 V as a function of device size.

In order to investigate such a variation, electron beam induced current (EBIC) was used to establish a correlation between leakage current and major types of defects in the substrate. For the tested devices having 750 μm on a side, the variation in leakage current in the region just prior to breakdown was approximately an order of magnitude, as shown in Figure 17. Figure 18 shows a typical EBIC image of a SiC APD. There were two types of dislocations which could be easily distinguished in the images based on shape: threading (spots) and basal plane (comet-like) dislocations. Based on intensity of the EBIC signal (the contrast of defects in the images), it was possible to differentiate “gray” and “black” dark spots associated with threading dislocations. This difference in contrast of threading dislocations was defined by a image processing algorithm, and is associated with different values of EBIC signals that depend on recombination rates of charge carriers at these defects. Thus, these defects might affect leakage current levels in different ways.

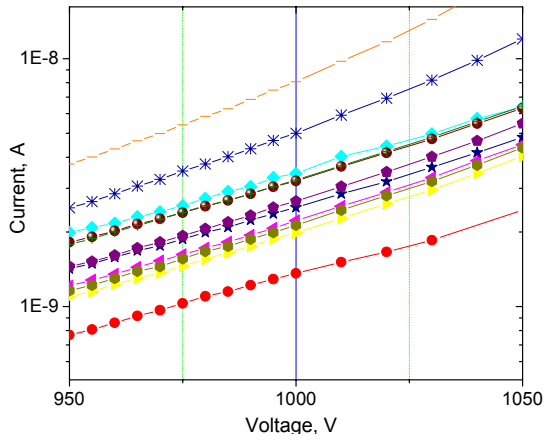


Figure 17. Variation in leakage currents for APD with the same size (750 μ m on a side).

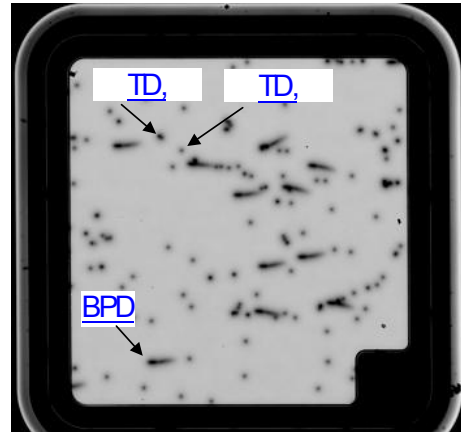


Figure 18. EBIC image of single APD

Using image processing software, densities of “black” and “gray” threading dislocations as well as basal plane dislocations were obtained (based on peak intensities as shown in Figure 19) and correlated with leakage currents of the corresponding APDs as shown in Figure 20. The results suggest a strong effect of threading dislocations on dark current. Moreover, in spite of the fact that a density of “gray” spots was much higher than the density of “black” ones, the effect of the “black” spots is more significant based on the slopes of the fitting curves. Densities of basal plane dislocations were almost the same in each device suggesting that a role of basal plane dislocations was not dominant in the leakage currents of the APDs.

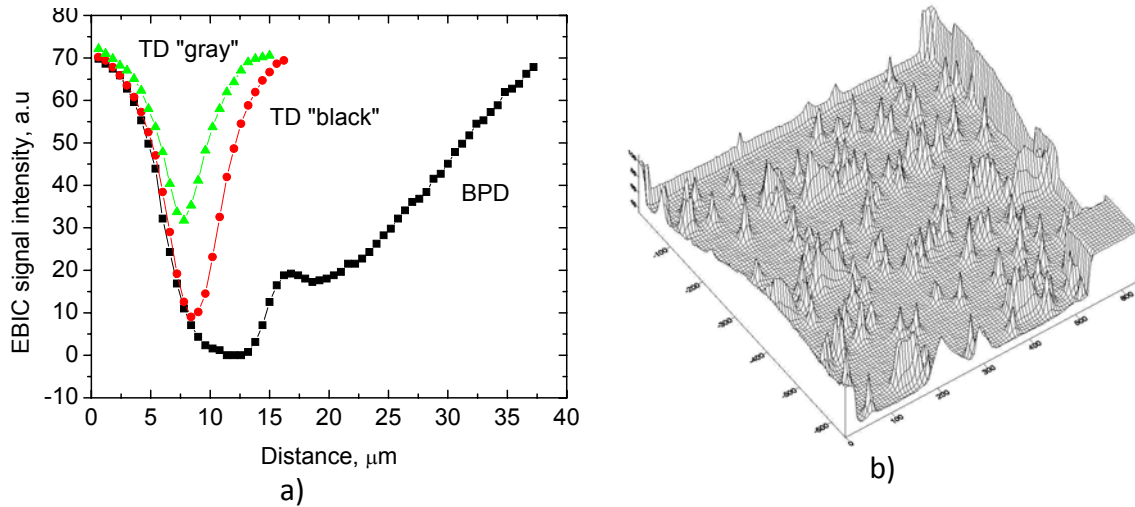


Figure 19. (a) EBIC signal line-scans and (b) 3D-image reversal map of EBIC signal intensity normalized.

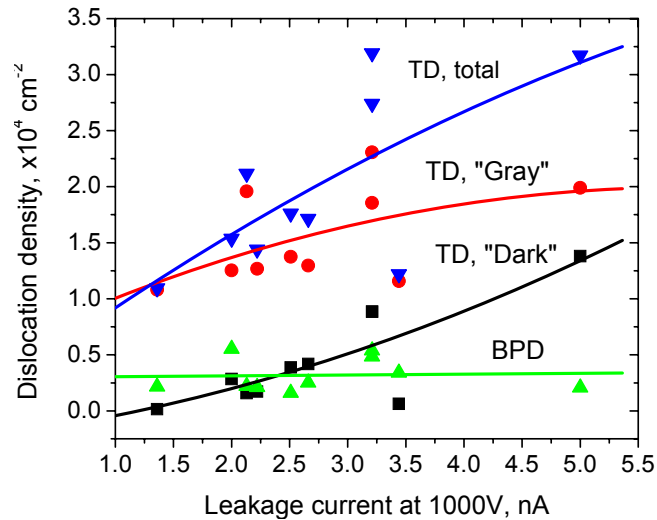


Figure 20. Correlation between defect densities and leakage currents.

In order to identify an origin of defects detected by EBIC imaging, etching the devices in molten KOH was performed.

Figure 21 shows two typical fragments of EBIC images and corresponding surface regions of the samples after etching. In past work, comparisons of etch pit patterns and EBIC dark spots showed a very strong correlation⁵ [3]. Characteristic shapes of the etch pits confirmed the differentiation between basal plane and threading dislocations made based on EBIC patterns. However, a detailed analysis of threading dislocations did not

⁵ S. Maximenko, S. Soloviev, D. Cherednichenko and S. Sudarshan, J. Appl. Phys., Vol. **97**, 013533 (2005).

facilitate the identification of a strong correlation between edge dislocations (ED) and screw dislocations (SDs) and “black” and “gray” spots in EBIC images. In some regions, as shown in Figure 19, “black” spots corresponded to screw dislocations, while “gray” spots corresponded to edge dislocations. At the same time, there were regions where SDs and EDs exhibited EBIC signals with the same intensity.

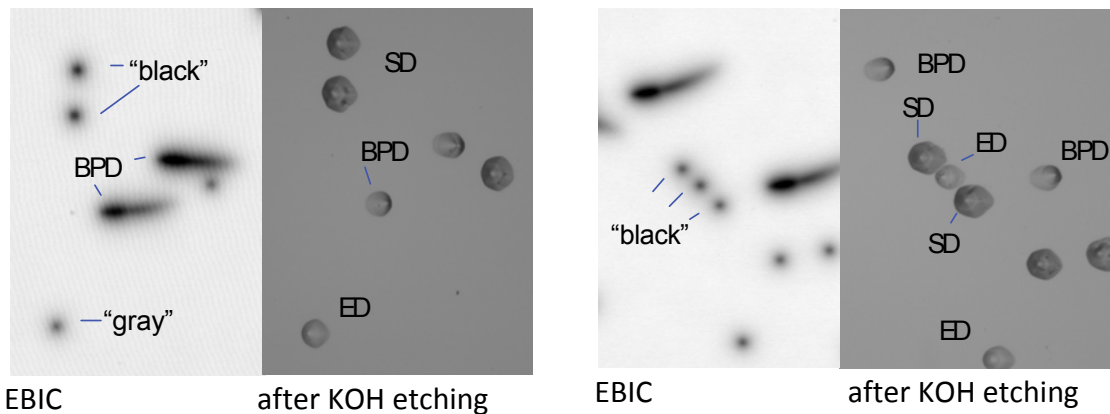


Figure 21. EBIC images and corresponding surface images after KOH etching taken at different regions.

1.4. Electrical characterization of APDs

In parallel, Gen II APDs were studied by Dr. Pavel Ivanov for various properties, under an informal collaboration. Dr. Ivanov looked at I-V properties in detail, focusing on the regime near breakdown. Under his testing, no illumination was observed at current (I) levels of 100 μA and below. Catastrophic breakdown did occur at $I > 100 \mu\text{A}$. This suggested the occurrence of a local breakdown (LBD), perhaps around crystal defect areas. Another indirect evidence of LBD was the observation of small bubbles in the Perfluoro Polyether (dielectric liquid used) under an optical microscope at the mesa edges. The bubbles could be caused by local heat dissipation.

The capacitance-voltage (C-V) properties were then measured by Dr. Ivanov. At a frequency of 1kHz, the curves shown in Figure 22 were taken.

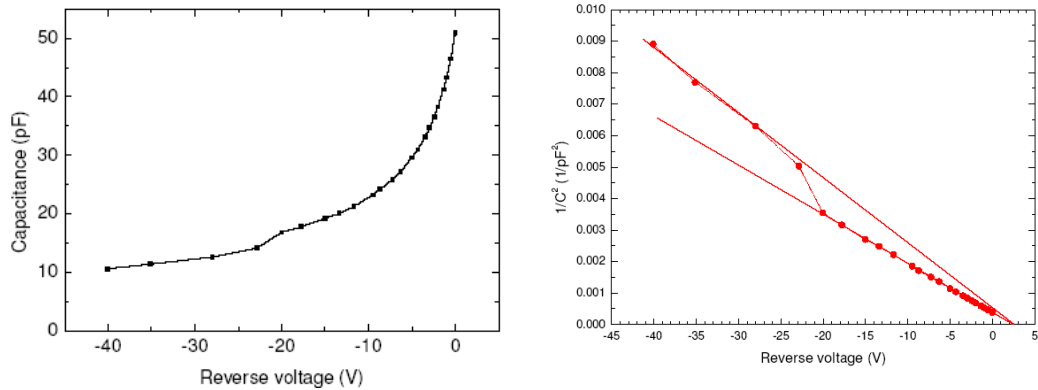


Figure 22. Capacitance voltage characteristics for SiC APDs with an area of $5.54 \times 10^{-3} \text{ cm}^2$ (left) and the voltage versus 1 over capacitance squared (right).

The C_0 value was found to be 51 pF by extrapolating the $1/C^2$ against voltage as shown in Figure 22. A closer look at this figure shows a “knee” in at $\sim 20\text{V}$, resulting in two linear regions. This is likely due to a decrease in the area of the space charge region (SCR) with increasing reverse bias when the SCR expands to reach the region where the mesa sidewall profile goes from beveled to nearly vertical. This feature was changed in the Gen III APDs as it was also found from the modeling (see below) that this 'kink' was likely an area of a very high electric field and possibly a source for premature breakdown.

1.5. Yield Testing

Several tests were done on the Gen III wafers following completion of the fab. The on-wafer tests provided some assessment of the yield of the various wafers, and the various device sizes including the array quadrants. The yield of the devices suggested an improvement from the past, and an example is shown for a quarter of the HM-19 wafer.

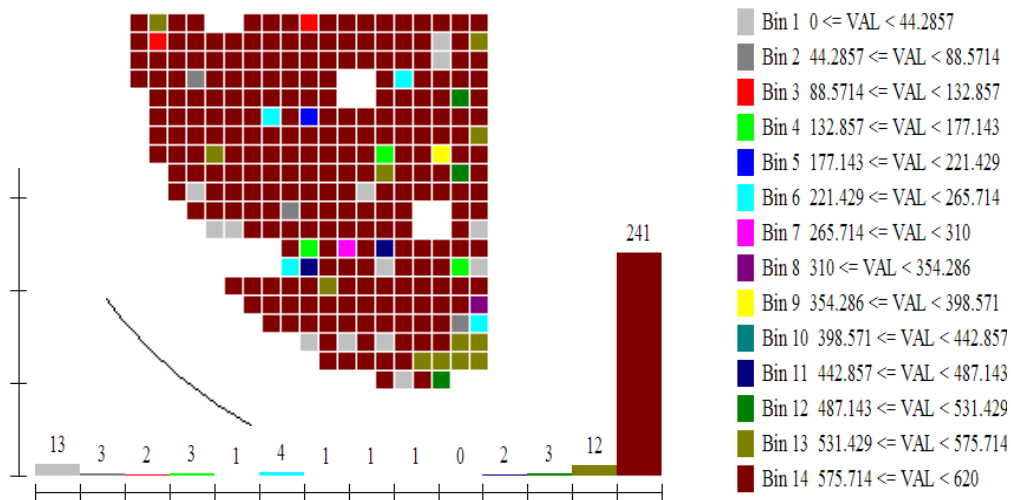


Figure 23. Yield distribution of 10 nA voltages in the HM-19 wafer (1 mm² quadrant).

In the above figure, the majority of the devices fall into the highest region of voltages, namely from ~575 to 620 V. Here, the current reaches a level of 10 nA within that range for over 80% of the parts attesting to the improved uniformity of this wafer and process.

Zooming in to show greater granularity on the yield plot, Figure 24 shows the distribution in 4 volt bins. It is apparent from the figure that within this range, there is a broad distribution of 10 nA voltages. It is also clear from the distribution that there doesn't appear to be any obvious macro-features in the wafer (e.g. epi doping variations from center to edge) that would influence the electrical properties on this scale.

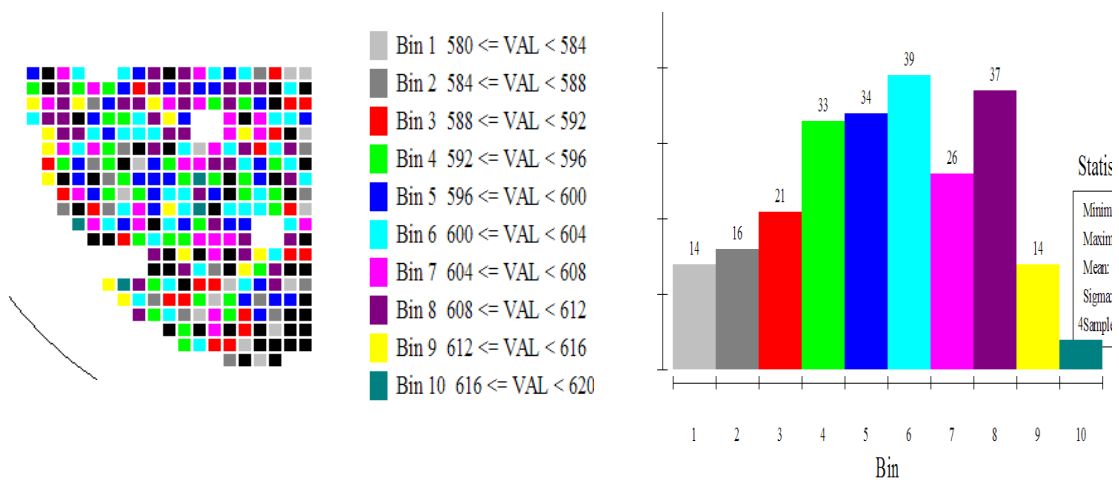


Figure 24. Yield distribution as shown in Figure 23 in greater detail.

It is noteworthy to mention that while there were at least 4 wafers in the Gen III lot, two of the four give breakdown voltages in the region of ~ 650 V, while the other two showed very high leakages on all parts, and breakdown voltages much lower than the target of 650 V. The two wafers with epitaxy obtained from Cree Research were those giving good results, while the two grown at GE Global Research likely had epitaxy deviating significantly from the thickness and doping targets and were therefore not evaluated in much detail. The results going forward will focus exclusively on the two wafers with Cree epitaxy unless noted otherwise.

Prior to dicing the wafers, random single devices with different areas were tested using manual probe station. Initial dark current and photocurrent measurements for the APDs were taken and are shown in Figure 25.

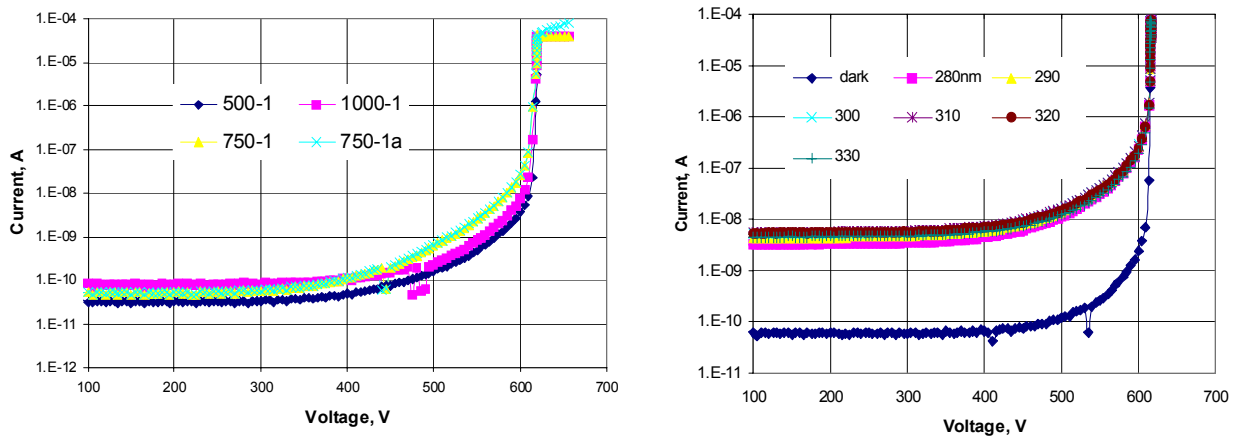


Figure 25. Leakage current measurements, showing current versus reverse bias of Gen III APDs (left) and photocurrent measurements at different wavelengths (right).

The actual avalanche breakdown voltage observed in the Gen III APDs (~ 613 V) is relatively close to the predicted value of 640 V from modeling work. The most likely source of the difference is from variation in the doping concentration of donors in the multiplication n- layer or localized micro-plasma breakdown at the periphery of the mesas and/or in proximity to crystal defects.

The photocurrent plot shown in Figure 25 largely mirrors the dark current, with a clear indication that there is good sensitivity in these devices. No arcing effect was observed during the testing thus far.

These devices, as highlighted above, show greatly improved current-voltage (I-V) characteristics as compared to the last iteration. A key feature that stands out from the plots is the lack of a significant shoulder in the I-V curve near breakdown that was present in the first two iterations of APDs. This difference is shown in Figure 26.

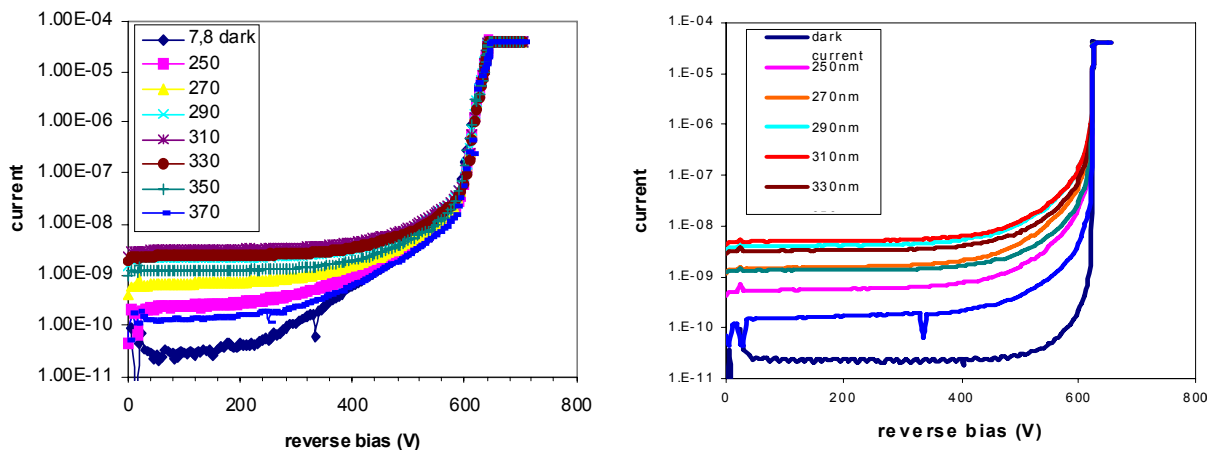


Figure 26. I-V characteristics of 500 by 500 micron APDs from the Gen II (left) and Gen III (right) iterations.

It is believed this is due to the reduction of the electric field in the absorption region, particularly at biases near breakdown. In past devices, electric field profiles as modeled showed the absorption layer becoming nearly or completely depleted, possibly leading to higher leakage levels at high fields.

1.6. Optical measurements

In parallel to the I-V measurements, a selected sampling of APDs were sent to the team of Professor Joe Campbell at the University of Virginia for quantum efficiency measurements and verification of our results. These measurements evaluate the sensitivity of the detectors to UV radiation. The quantum efficiency (QE) is defined as the percentage of incident photons that result in collected carriers, as measured by the photogenerated current, or photocurrent.

Figure 27 shows the typical QE as a function of wavelength throughout the UV. The three lines show the QE at a device bias of 150 V, 50 V and 5 V. The two plots showing 150 V and 50 V measurements are very similar.

While the QE observed in these devices is rather low at low biases, it is likely attributable to the thickness of the device and the loss of photogenerated carriers to recombination prior to reaching the depletion region. Recent modeling studies suggest that thinning the overall structure has several benefits, including the likelihood that the QE will be improved from the low bias peak of ~20%. Past work in SiC photodiodes of significantly thinner structures have shown that peak QEs of greater than 50% should be attainable despite the materials' indirect bandgap.⁶ Similarly, the optical properties show marked improvement as well in comparing Gen II and Gen III APDs. Taking measurements of the approximate quantum efficiency (QE) of Gen II and Gen III APDs yields the comparison shown in Figure 28.

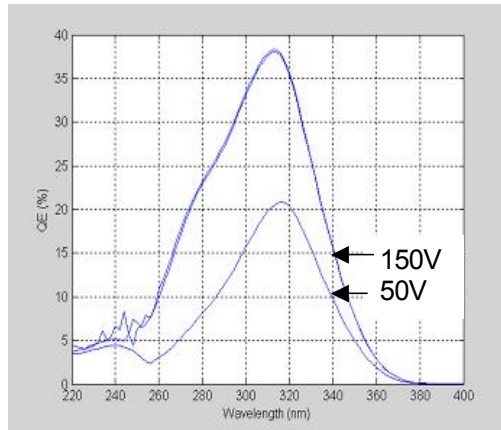


Figure 27. Quantum efficiency of GE's SiC APD L7-29 (iteration 2) as measured by the team of Prof. Joe Campbell.

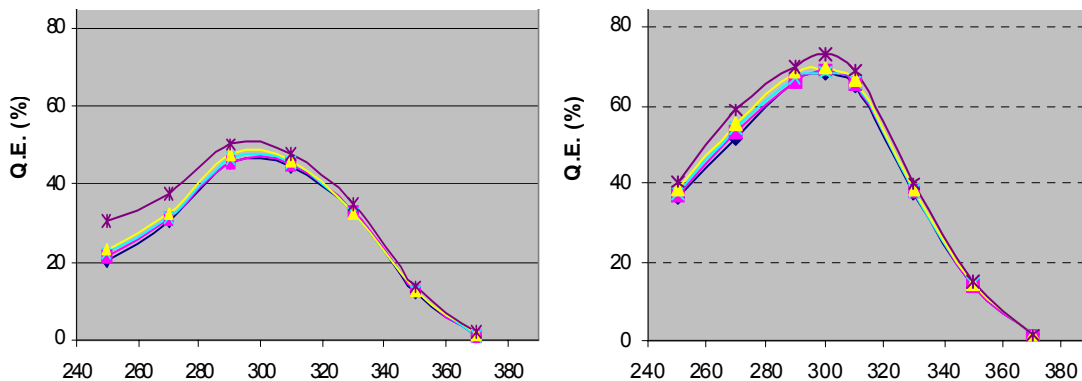


Figure 28. Gen II (left) and Gen III (right) APD measurements of quantum efficiency versus wavelength (nm).

Following the predicted values, the Gen III APDs have a significantly better optical sensitivity throughout much of the UV. Also, testing on the SiC APDs was performed at higher temperature and high electric fields. The leakage current and photocurrents as functions of temperature are presented in Figure 29.

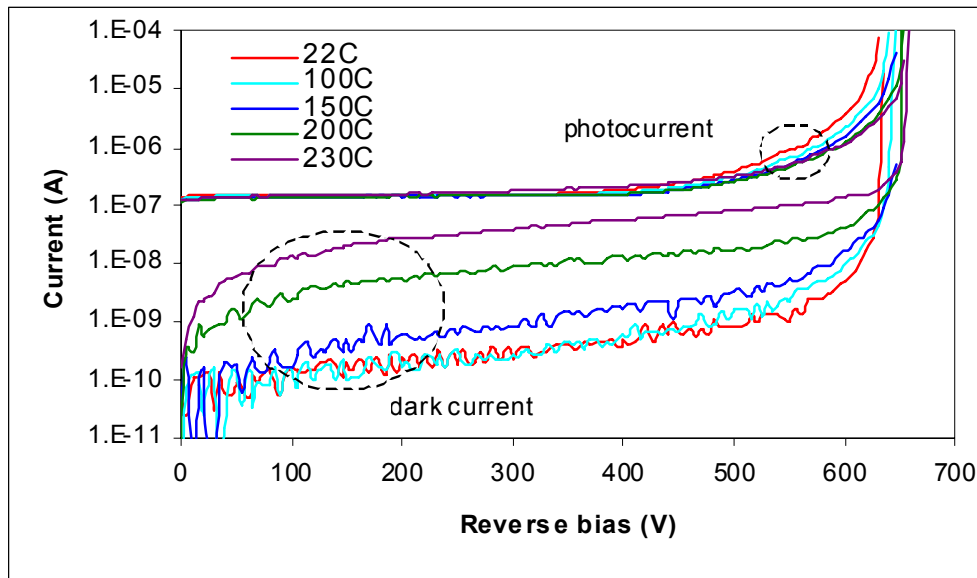
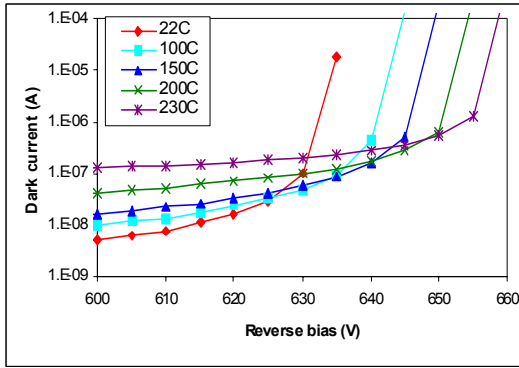


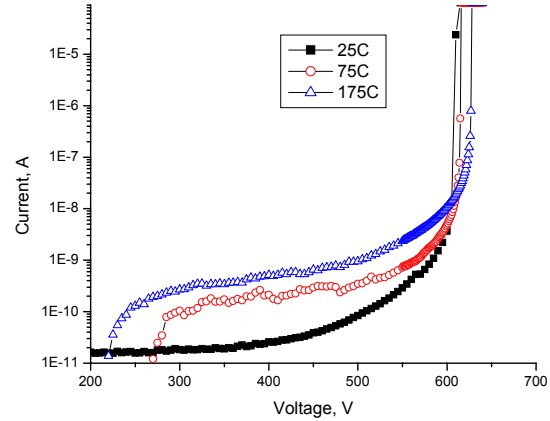
Figure 29. Leakage and photocurrent vs. temperature of 1x1 mm² APDs.

If one zooms into the dark current curves near the breakdown voltages, Figure 30 may be obtained.

⁶ Brown et al., IEEE Trans. on Elect. Dev., **40**, p. 325 (1993).



a)



b)

Figure 30. Zoomed in breakdown curve of dark current against temperature for (a) 1x1 mm² and (b) 0.75x0.75 mm² APDs.

As observed in the literature and in past GE reports, the breakdown voltage increases with increasing temperature. This is a vital behavior as it enables the APDs to be operated at a fixed current level over a range of temperatures without concern that runaway breakdown may occur. Scattering of charge carriers in the SiC likely increases substantially with increasing temperatures requiring a greater potential energy prior to ionization in the device.

Quantum efficiency was measured as a function of wavelength and temperature as shown in Figure 31. The tests were performed on 1x1 mm² die and with 100 V reverse bias. Maximum QE at room temperature was ~47% at $\lambda=290$ nm.

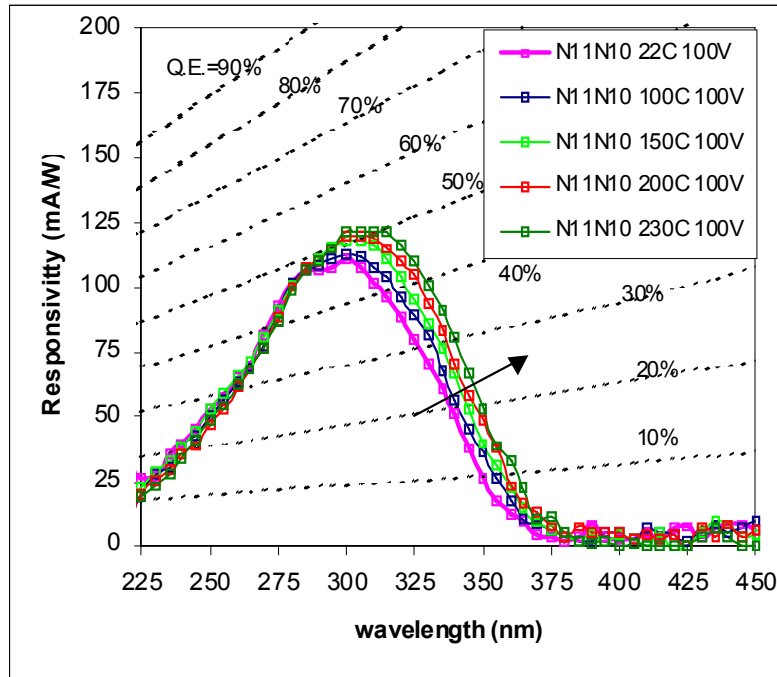


Figure 31. Responsivity as function of wavelength and temperature for a yielded SiC APD. The quantum efficiency levels are shown in the dotted lines.

There are two important observations from this testing. First, the peak wavelength of the detectors' quantum efficiency shifts to the right, lower in energy. Second, the band of wavelengths from ~300 to 375 nm sees a slight increase in quantum efficiency. In both cases, these are desirable traits as the scintillator will be generating much of its output at the lower energy side of this response curve and the higher sensitivity with temperature is welcome as the sensor will likely be subjected to 200 °C and perhaps higher.

These general behaviors have been observed in other works as well, dating back to D. Brown et al., IEEE Trans. Elect. Dev., 1993 (see Ref. 6). However, the reasons for this device behavior have not yet been determined and are likely complex.

The nature of these phenomena has been the subject of discussion internally, and GE presently has no definitive answer. What's partly at cause is the reduction in bandgap with increasing temperatures, a common trait in semiconductors described by Vegard's law or similar. For 4H SiC, this relationship follows:

$$E_g = E_g(0) - 6.5 \times 10^{-4} \times \frac{T^2}{T + 1300} \text{ (eV)} \quad \text{from Ref. } ^7$$

⁷ Yu. Goldberg, M. E. Levinshtein, S. L. Rumyantsev. in *Properties of Advanced Semiconductor Materials GaN, AlN, SiC, BN, SiC, SiGe*, Eds. M. E. Levinshtein, S. L. Rumyantsev, M. S. Shur, John Wiley & Sons, Inc., New York, 2001, 93-148.

where $E_g(0)$ is approximately 3.23 eV and the temperature is in degrees K. However, in applying this relation to the above sensitivity changes with temperature, it only accounts for a relatively small percentage of the shift in the curves. It may help explain the lower wavelength shifts (e.g. 300 nm and below) as the response actually decreases a small amount. More data of this kind can be found at <http://www.ioffe.rssi.ru/SVA/NSM/Semicond/SiC/index.html>⁸.

Given that likely small contribution from the bandgap shift, there is likely another component affecting the observed data. One likely cause is a change in the phonon population with changing temperatures. As 4H SiC has an indirect bandgap, a phonon assisted absorption process is required. The band structure of 4H SiC is shown below in Figure 32 for reference.

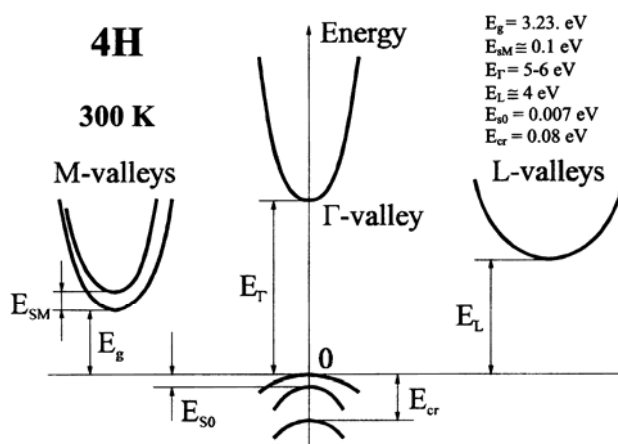


Figure 32. Band structure of 4H SiC after Ref. ⁹.

Closer examination of the band structure in SiC shows a dominant M-valley in the conduction band, where the bandgap of 3.23 eV separates it from the gamma hole maxima. Gamma (Γ) and L-valleys are also present but with conduction band maxima of $\sim 5-6$ eV and ~ 4 eV above the gamma hole band maxima, respectively, which suggests those valleys likely aren't contributing much to the observed changes given their lower energies. Future work will include a literature search of the M-valley phonon behavior to see if that helps elucidate the increase in response at smaller energies than our peak.

⁸ <http://www.ioffe.rssi.ru/SVA/NSM/Semicond/SiC/index.html>.

⁹ C. Persson, U. Lindefelt, and B. E. Sernelius, Band gap narrowing in n-type and p-type 3C-, 2H-, 4H-, 6H-SiC, and Si, *J. Appl. Phys.* **86**, 8, p. 4419-4427 (1999).

1.7. Materials Studies

Detectors

Individual detectors were tested at increasing levels of reverse bias, and a noteworthy observation was made. In the larger devices, while the devices were under probe, the illumination was collected. Figure 33 shows this effect.

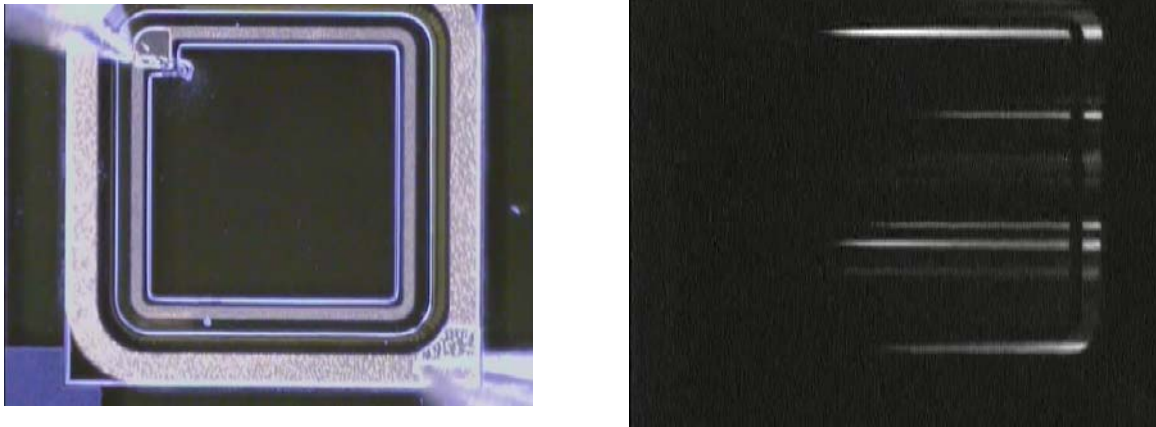


Figure 33. Optical photo of the APD under test (left) and under reverse bias (right).

It is clear from the image on the right, there are horizontal streaks of light being emitted from the diodes while subjected to large, reverse biases. The device was rotated to multiple orientations to verify that the streaks observed were not from an optical effect rather than stemming from the APDs. Upon verifying that the streaks were indeed originating from the APDs in several cases in apparently random arrangements, they were investigated further.

With increasing reverse bias, the streaks observed appeared to grow brighter. Some of the streaks originated in the diode's central active area, while some streaks appeared to run throughout the diode from left to right as in the case of Figure 33.

Initial speculation was that these streaks resulted from recombination events along stacking fault dislocations in the material. Stacking faults are a type of defect that has been the subject of study in SiC, particularly in the area of power devices (see for example, ref 10). Their formation, or in some cases propagation, has been observed a number of times during high forward biases.

¹⁰ S. I. Maximenko and T. S. Sudarshan, J. of App. Phys. **97**, 074501 (2005).

Here, however, what has been puzzling is that these streaks only occur in horizontal lines, and not also at 60 degree variants as one might expect for this hexagonal crystal. No further explanation for these observations is available at this time, although the luminescence from these streaks was recorded as a function of wavelength, and for documentation purposes, it is shown in Figure 34.

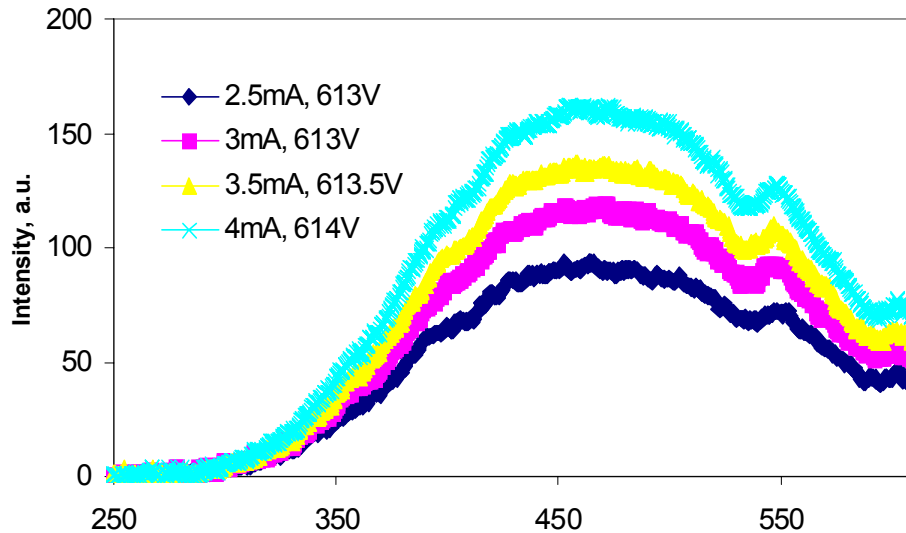


Figure 34. Luminescence as a function of wavelength from the diodes, after forward biasing at levels shown in the inset.

This luminescence very likely consists of a number of peaks, and even identifying which energies are the source of irradiance is a challenging task. This irradiance may be related to luminescence peaks observed from PL or XRD illumination, or they may be originating from other sources. This has been further described by Solovoev.¹¹

Wafer Comparisons

A nice comparison study of globally available SiC substrates was done in part at GE and in part at Dublin City University by the group of Prof. Patrick McNally. This work is summarized in the 2006 ECSCRM paper¹². This paper is included as an appendix (B) if that work is of interest to the reader.

¹¹ S. Soloviev et al., *ICSCRM Proc.* 2007, to be published.

¹² I. Brazil et al. An X-Ray Topographic Analysis of the Crystal Quality of Globally Available SiC Wafers. *Materials Science Forum Vols. 556-557*, pp. 227-230, (2007).

2. Task 9 - Development of APD arrays and device packaging

Two approaches in developing APD arrays were considered in the project. The first approach was to fabricate a single die with 16 APD devices of $500 \times 500 \mu\text{m}^2$ each (see Figure 8), connected in parallel. This approach is kind of standard for Si APD array technology due to a high quality of Si material. However, a defect density ($\sim 10^4 \text{ cm}^{-2}$) in SiC substrate might result in a low yield of large area single dies from a wafer. The second approach was to assemble an APD array on the special carrier from selected single APD dies. This approach is more expensive, however, yield is higher.

2.1. Single die with 16 APD devices

In the current design of APDs, both p- and n-electrodes are located on the top the structure. Thus, an additional metallization layer serving as a common pad for external n-electrode is required for the APD array. P-contacts of single devices were merged in the APD design as shown in Figure 8.

In contrast to the above yield findings, a similar test was done on the HM-21 wafer's array quarter. Here, each box or array is comprised 16 APDs, and the total size of each unit is approximately 2.5 mm on a side. Thus, for each array, there were 16 pass/fail assessments with the pass getting the green square and the fail getting a gray square (Figure 35). Only a few arrays with all 16 detectors showed adequate performance.

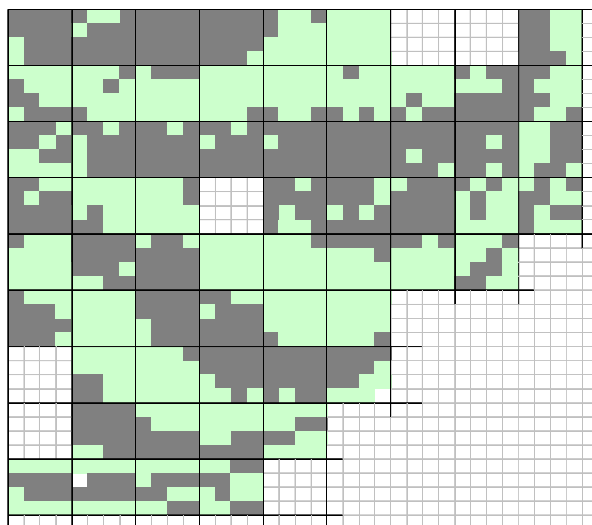


Figure 35. Quarter wafer with arrays showing pass/fail results. The upper left is the center of the wafer.

It is also interesting to note that the diodes did seem to follow some macro-type patterns on the quarter of the wafer, suggesting that the substrate or epitaxy may be playing a significant role in yield (these processes often have center to edge transitions). It is also noted that in the areas with no data, there were test structures. Yield of single die containing an APD array was determined to be too low for use in the device packaging approaches described below; however, the initial designs and approaches were developed to accommodate such die when the yield improves.

2.2. APD array of 16 individual dies

After fabrication of the devices, each device was tested before dicing in order to select “passed” devices for further use in APD arrays.

To accommodate this approach, the team at GE Research developed a packaging process that enables the construction of SiC APD arrays in a robust manner, and that is also flexible in design. The 'flex' packaging processes that were developed at GE Global Research over the past 10-15 years and beyond were identified for this application, and modifications to these approaches were therefore studied here.

The flex packaging process in at least one case utilizes Kapton film as the basis for mounting multiple components and attaching a variety of features (Figure 36). In this way, Kapton, a robust, flexible material may be used essentially as a substrate layer.

Two examples of the flex process that were examined with the goal of ultimately building a rigid substrate (disc) with our APDs are:

Process Option 1 [Power Overlay Chip on Flex; POLCOF]

- Dielectric removed from flex with laser over active area prior to die attach
- Direct chip attach to dielectric substrate
- Requires chemical compatibility with interconnect processing
- Polyimide passivation option [active area protection from chemistry option]
- Single die vs. tiled options available
- Plastic encapsulation and backside feed-thru connections possible

Process Option 2 [HDI Chip on Flex; HDICOF]

- Direct chip (APDs and feed-throughs) attach to dielectric substrate
- Dielectric removed with laser post interconnect processing
- Eliminates active area exposure during interconnect processing
- Relaxes die attach placement accuracy requirements
- Polyimide passivation option [active area protection from ablation]
- Single die vs. tiled options available
- Plastic encapsulation and backside feed-thru connections possible

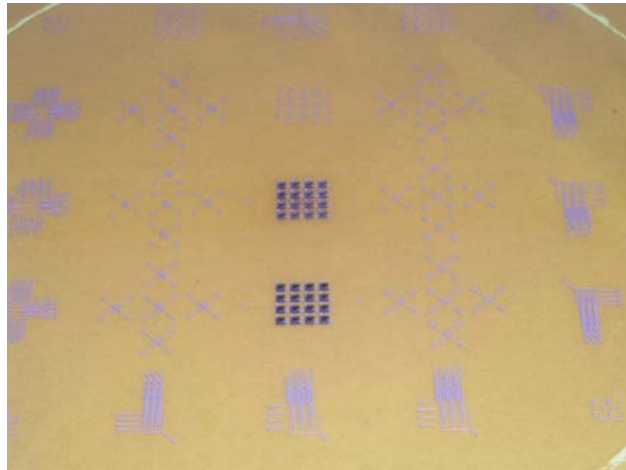


Figure 36. Kapton film on a frame showing several different array designs. In the center, two array designs have been successfully populated with SiC APDs.

In the case of the first option, POLCOF, the process sequence is as follows:

- Apply 14 μ m epoxy adhesive / 25 μ m cover sheet to 25 μ m Kapton
- Laser profile flex for component active area placement
- Remove cover sheet protection layer, attach die, cure adhesive [optional copper feed thru attach, plastic encapsulation – dam/fill epoxy]
- Form μ Via with direct write laser drill

-
- Plasma clean via holes, sputter / electroplate interconnect metal
 - Metal interconnect processing, subtractive etch, direct write laser pattern
 - Post interconnect processing options:
Remove PI passivation with RIE, laser singulate package, plate Ni/Au finish

A high powered laser is used to cut out selected areas of the Kapton, in this case, where the APD active area is located. An alternative to this process is HDICOF, where the main difference is that the die are attached first, then the Kapton holes are drilled.

This HDICOF process is described as:

- Apply 14 μ m epoxy adhesive to 25 μ m Kapton E
- Attach die, cure adhesive
[optional copper feed thru attach, plastic encapsulation – dam/fill epoxy]
- Form μ Via with direct write laser drill
- Plasma clean via holes, sputter / electroplate interconnect metal
- Metal interconnect processing, subtractive etch, direct write laser pattern
- Laser ablate dielectric from active area windows on die
- Post interconnect processing options:
Remove PI passivation with RIE, laser singulate package, plate Ni/Au finish

Both processes were explored in order to identify as many options as possible. After an initial trial, both the POLCOF and HDICOF process were successful. Comparing the two processes, the POLCOF approach was initially considered to be a more conservative option as it allows the active areas to be drilled in the Kapton prior to die attach, thereby reducing any potential damage done to the APDs during laser drilling. Simple I-V testing has led GE to believe that such damage is either not occurring in the HDICOF process, or that it is very small to the extent it has not shown itself in the APDs tested thus far.

A desirable trait of both of these processes is that the detectors may be placed in a variety of arrangements on a substrate, and the substrate itself may be tailored to fit a desired package. As the gamma sensor system fits inside what is essentially a tube, a circular substrate may best fit the package overall as shown in Figure 37 and Figure 38.

The flex package shown below in Figure 37 shows 16 APDs interconnected using the HDICOF process, including the epoxy substrate encapsulation, and then cut from the Kapton frame.

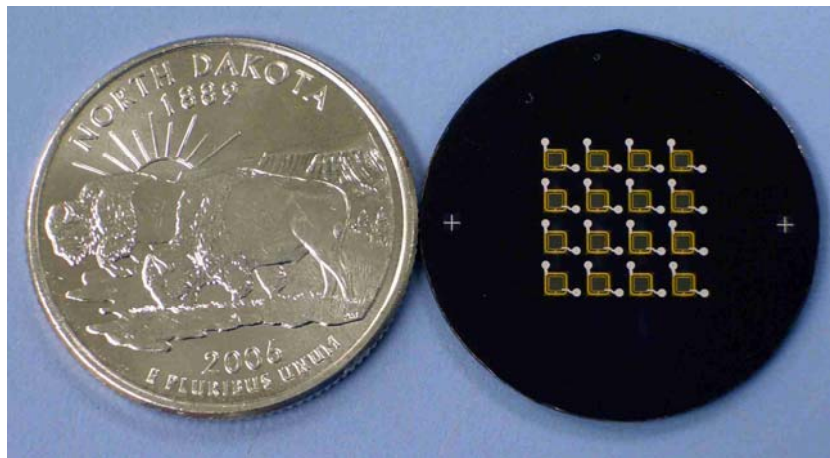


Figure 37. A photograph of a 4x4 SiC APD array packaged using the flex process described above. A quarter shows the size of the disk, which has a 1 inch diameter.

This substrate was made by taking the sheet of populated APDs and forming a disk-shaped substrate by flowing a silica-filled epoxy into a volume defined by a higher viscosity silica-epoxy dam.

A small diameter of the substrate may be preferable towards improving the fill factor (ratio of active area of the detector to the total surface area receiving light from the scintillator) of the array. If a one-inch diameter scintillator crystal is used, it may be beneficial to put as many APDs at the immediate center of the substrate for better light collection. Such array layouts have been explored.

To improve the light collection further, the team considered smaller scintillator diameters (e.g. 1 cm), or possibly forming a tapered and truncated cone of optical coupler material instead of a simple disk. This may be wrapped in Teflon tape to direct as much light as possible from the scintillator to the active regions of the detectors.

The APD array sub-mounts were built in two iterations. In the first iteration, the basic process of patterning the flex packaging material on the top side with the APDs was demonstrated. A picture of these 'gen 1' sub-mounts is shown in Figure 38.



Figure 38. APD array sub-mounts from the first iteration ('gen 1'). Various metals as well as various layout geometries were prototyped to make the process as robust as possible.

Taking completed sub-mounts, testing was performed to validate these parts with exposure to elevated temperature. The test used a convection oven with a N₂ atmosphere. The temperature was maintained at 100 °C for 12 hours and then at 225 °C for over 96 hours. This enabled the evaluation of the plastic, chip adhesive and metal coatings.

Mechanical packages were also tested using 2 adhesive systems, epoxy and acrylic. A summary of this test was the following:

- The plastic molded mechanical samples passed visual inspection post thermal soak in N₂ convection oven (100 °C for 12 hr then 225 °C for 168 hr):
 - The plastic molded mechanical module with epoxy adhesive failed the visual inspection (100 °C for 12 hr then 225 °C for 96 hr)
 - The plastic molded mechanical module with acrylic adhesive passed visual inspection (100 °C for 12 hr then 225 °C for 96 hr)

A second generation build of APD array sub-mounts was then undertaken which extended the first iteration by incorporating an optical reflector in the areas surrounding the APD elements, as well as copper feed-throughs to facilitate contact to the backs of the sub-mounts. In addition, the second build allowed:

- Evaluation of alternate designs as well as a repeat of the gen 1 design

- Evaluation of 0.5 mm and 1.0 mm APD die sizes
- Implementation of an upper level of laminate
- Evaluation of a back-side metal process
- Verification that the ablation process does not change with added metal and dielectric

Figure 39 shows the outcome of the gen 2 sub-mount fabrication process.



Figure 39. Gen 2 APD sub-mount build, showing several arrays on a Kapton frame. At left, the front side is shown, while the back-side is shown at right.

The front side of the sub-mount incorporated a diffusely reflective thin film coating which will reflect light back into the scintillator that doesn't get absorbed by the APD initially. As the fill factor of the APDs is relatively low on the sub-mount, the reflector should help improve the light collection. This process was largely successful in accomplishing the following:

- Plastic encapsulated modules were thinned to 25mils (originally molded to 42 mils thick)
- Back-side copper contacts were exposed
- An aluminum reflector layer was applied to the topside (white coating shown in Figure 39)
- The window-last ablation process was demonstrated
- The radial die array geometry was demonstrated
- 0.5 mm and 1.0 mm die were populated on the two frames

More detail is shown in the magnified photograph shown in Figure 40. The discs are approximately 1 inch in diameter. The back-side of the arrays show the copper pins

where electrical connections will be made. The white aluminum coating is shown on the front, which should enhance the light collection of the APDs.

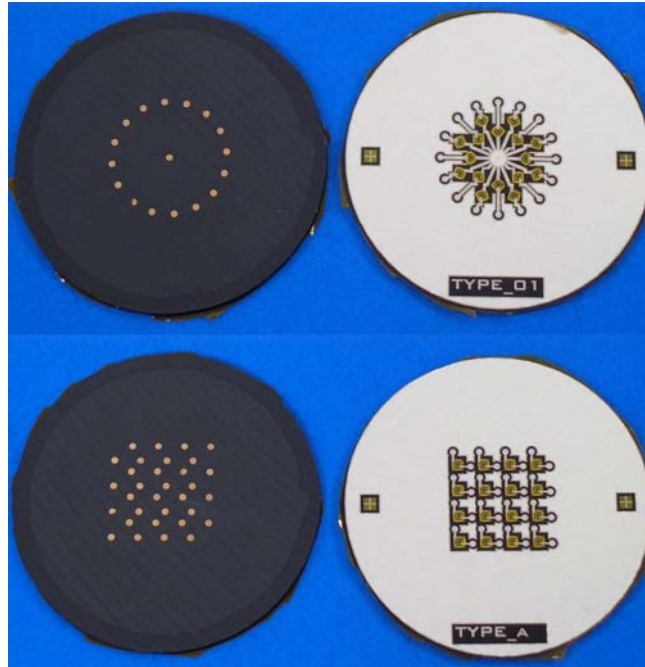


Figure 40. Magnified pictures of the radial "snowflake" layout (shown above) and the rectangular grid layout (below).

Electrical testing was performed on several of these discs in order to evaluate the APD yield post processing. Most of the APDs passed after being integrated into the sub-mount, with about 20% or less failing by showing a short or greatly increased leakage. Further evaluation determined that contamination due to handling was the primary cause of leakage. Removal of mobile ions immediately prior to applying optical coupler should eliminate this issue.

A third sub-mount build was subsequently undertaken, which took the above work further by incorporating the electrical connector to the back of the array along with flex electronics to draw the leads to a series of electronics boards where the back-end amplification takes place.

Alternative approaches were identified for future system optimization, however, the above method uses components and processes that are known from past work. The key additional step in this iteration is the realization of a flex interposer, that enables the traces to bend 90 degrees and facilitates the APDs facing the scintillator.

2.3. Gamma Detector Assembly

Assembly of the complete Gamma detector was accomplished in two phases. Fabrication of the APD array module (described above) and the drive board were completed at GE Research. Final assembly of these components to the scintillator crystal and into the detector fixture was accomplished at GE Reuter-Stokes.

The drive board was populated using components and materials compatible with Pb-free soldering, specifically, SnAgCu solder, which has a melting point of 232 C. While the drive board could be assembled using high-Pb solder, the reflow equipment at GE Research is not capable of reaching the temperature needed. As with the APD arrays, the drive boards should be cleaned to remove any mobile ions post assembly.

The drive boards were connected to the APD arrays through the flex interposer as shown in Figure 41, by hand-soldering, again using Pb-free solder. While the approach proved satisfactory for prototyping purposes, a ceramic transistor header “can” including pins, similar to a TO8 package would provide a much more manufacturable process. Subsequent to assembly of APD arrays to drive boards, the performance of the detectors was quantified.

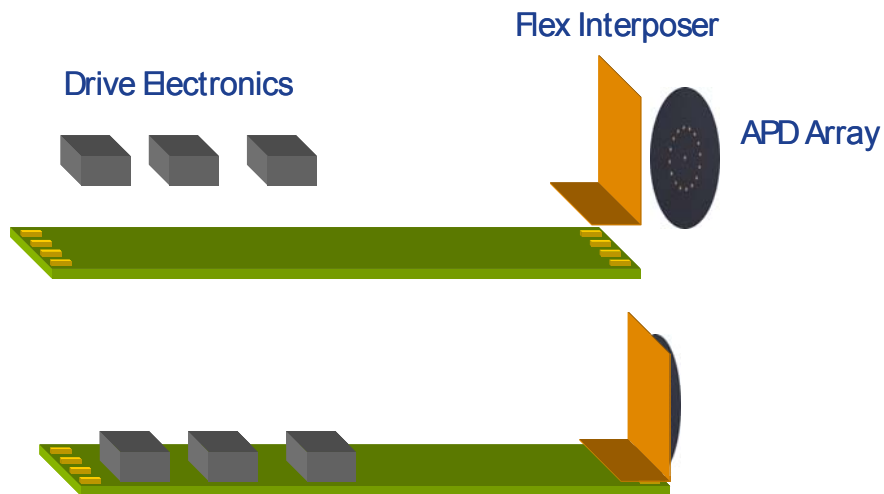


Figure 41. Concept figure of the third generation sub-mount build, showing the flex interposer, which connects the array to the electronics board for integration to the gamma sensor prototype.

Six APD arrays with sixteen individual dies on each sub-mount were fabricated and attached to the flex interposers. Prior to the connecting them to the drive boards,

individual APD device was tested again to verify its functionality. Figure 42 shows typical dark current curves of sixteen APD measured with the flex interposer. These characteristics confirmed good electrical contacts to the individual dies through the flex interposers.

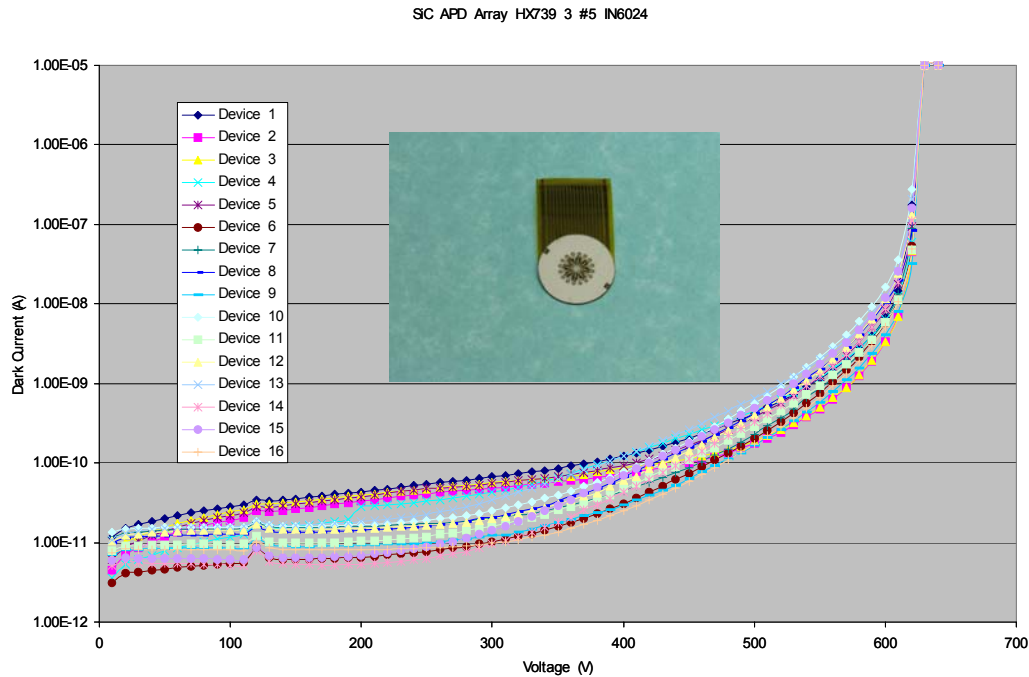


Figure 42. Dark Currents of individual APDs on Sub-Mount with Flex Board.

3. Task 10 - Evaluation of reliability of APD devices

APD testing was performed to better gauge the devices' reliability and repeatability. A test was done to look for drift in the electrical properties of the devices after holding the devices at high biases. Figure 43 (a) shows the APD current (left scale) and voltage (right scale) levels as a function of time for the first five hours. Here, the devices were kept at 220 °C.

A burn-in effect was observed in the first hour of testing, as shown on the left in Figure 46. The exact nature of this is not understood, however, a possible contributor is the self heating internal to the device from the associated power dissipation. During the test, the applied voltage was increased every five hours to set initial currents at 0.1, 0.2, 0.3, 0.5, 1.0 and 1.5 mA. For a period of 30 hours, the device appears very stable even up to current levels of 1.5 mA as shown in Figure 43. The gain level at a current of 1 mA

(or higher) will likely put the device into the regime where the signal to noise ratio is past optimization, thereby limiting it's expected current of operation to several hundred microamps.

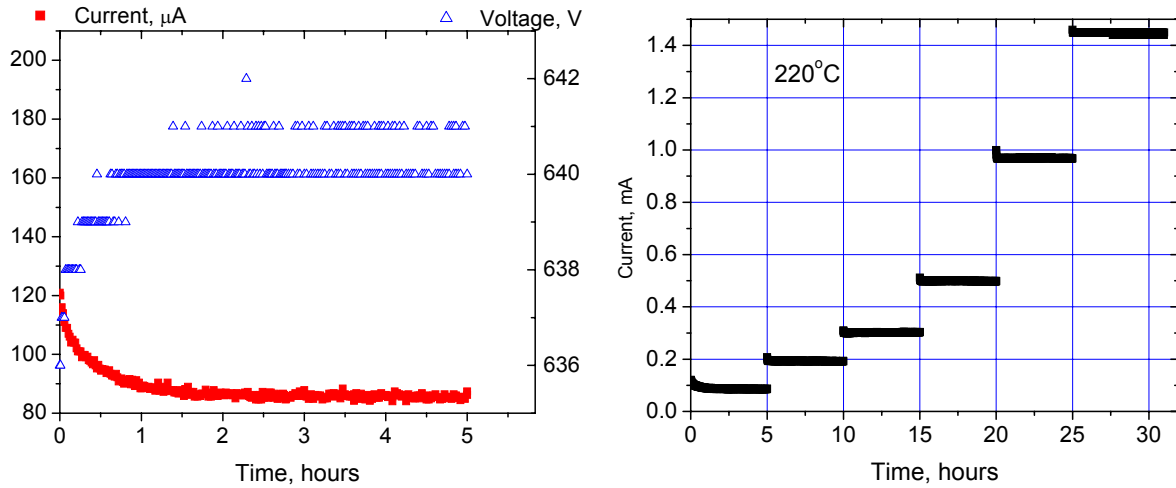


Figure 43. APD reliability testing, showing the APD electrical properties as a function of time.

Additional tests were done using multiple current-voltage (I-V) sweeps, going from zero bias up to a voltage level putting the device well into breakdown. This effectively stresses the APDs in a different way with huge swings in the electric field.

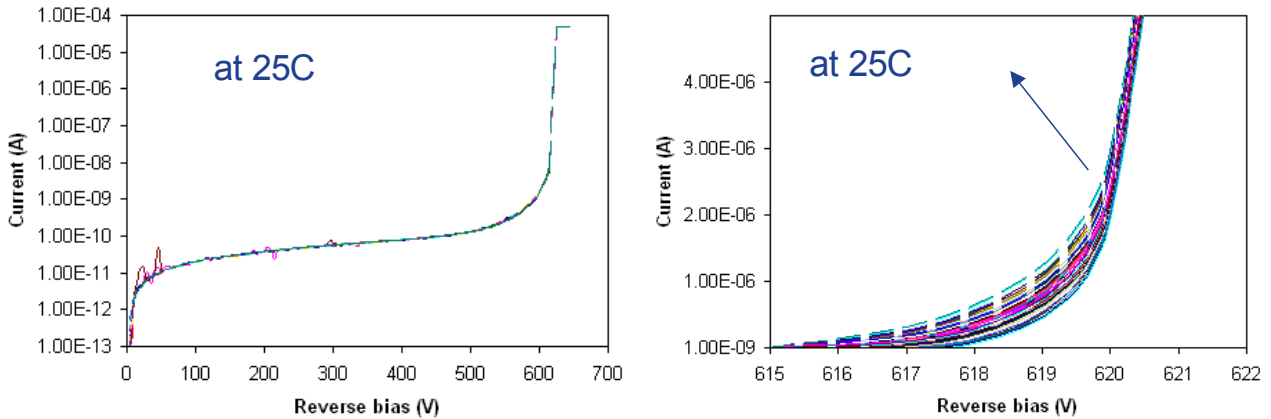


Figure 44. APD reliability testing using multiple I-V sweeps at room temperature.

The testing showed very little electrical drift after as many as 200 sweeps, taking the APDs from zero bias up into breakdown ($\sim 50 \mu\text{A}$ compliance). In Figure 44 at right, the region where the onset of avalanche is shown to shift by approximately 1 V. A similar test was performed while the devices were kept at 200°C , as shown in Figure 45. As the cycles showed very good agreement, only a relatively small deviation is apparent.

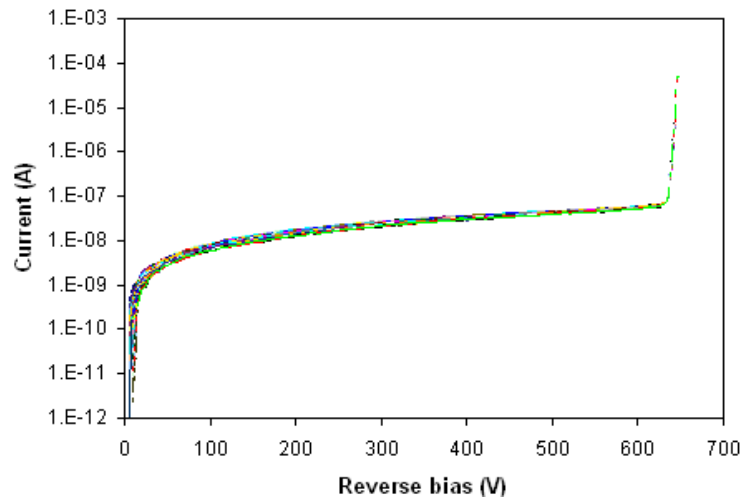


Figure 45. APD reliability testing at 200°C . Here, 200 I-V cycles were performed over a ~ 15 hour period.

Reliability testing of APDs held in breakdown was performed. A curve tracer was used that enables fast current-voltage sweeps up to several hundred volts. Because this tool does not allow for precise measurements, the error bars in this type of measurement are large. In any case, a computer controlled program was used to poll data at selected time periods while the devices were held at selected voltages, currents and as a function of temperature via a hot chuck.

Here, the devices were kept at the voltage and current levels shown in Figure 46. As observed, the APDs appear to be robust for at least periods of 10-12 hours in these preliminary testing.

At left, an apparent burn-in took place before the APDs settled on stable current levels. Less obvious is the same behavior shown on the right, where even at 225°C , the APDs appear to be stable up to ~ 12 hours. The devices have also been cycled multiple times into breakdown and appear to be stable, at least for the best APDs. Some devices don't pass this type of yield test, however, so the overall yield of the APD fabrication process may be somewhat reduced after the above type of validation test.

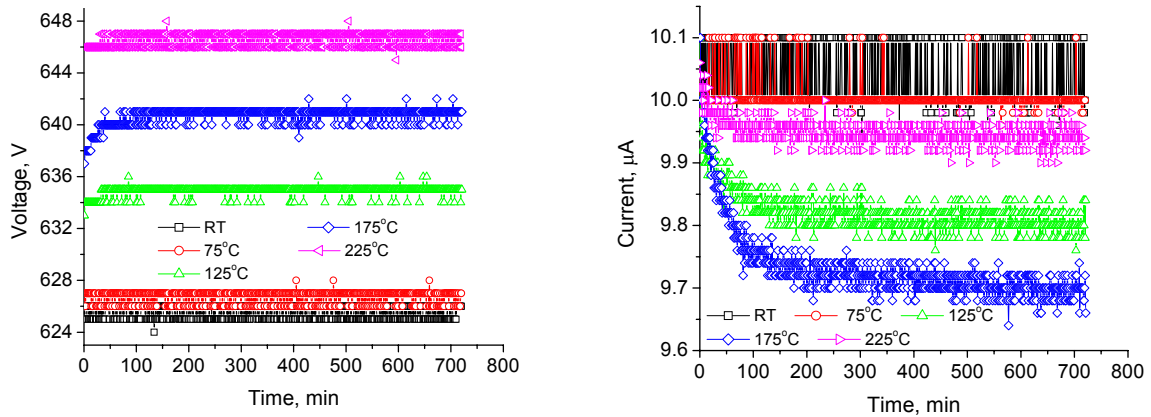


Figure 46. Testing of APDs showing the voltage (left) and current (right) levels as a function of time.

Long-time reliability testing of five selected APDs biased at an avalanche breakdown voltage was conducted for 400 hours at 220 °C. The results shown in Figure 47 demonstrated that all five devices stressed at the currents of $\sim 10 \mu\text{A}$ survived during the test.

Another selected APD was tested at the same conditions. No current drift was observed for 1400 hours. (Figure 48). The test was terminated. Based on measured data, an estimated failure time for such an APD device operations at 220C would be about 4,000 hours.

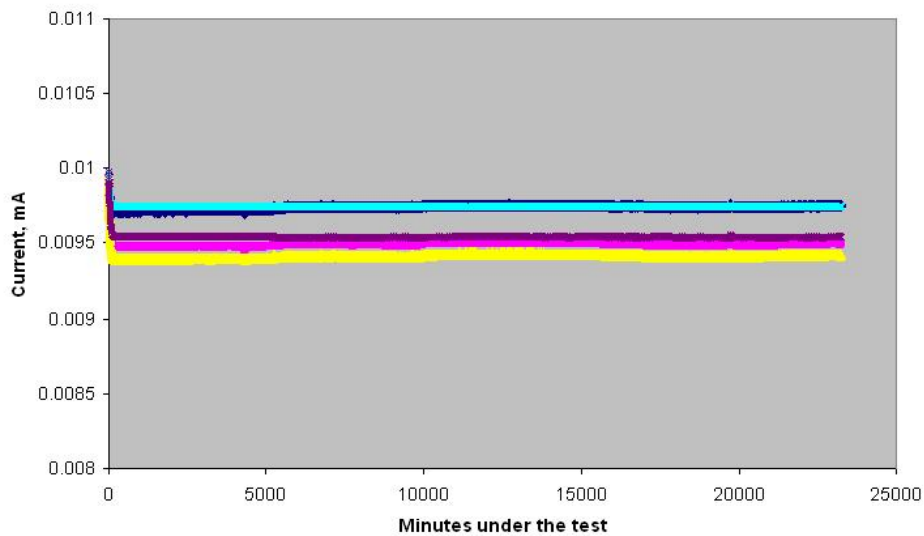


Figure 47. Currents of five APDs tested at 220°C for 400 hours.

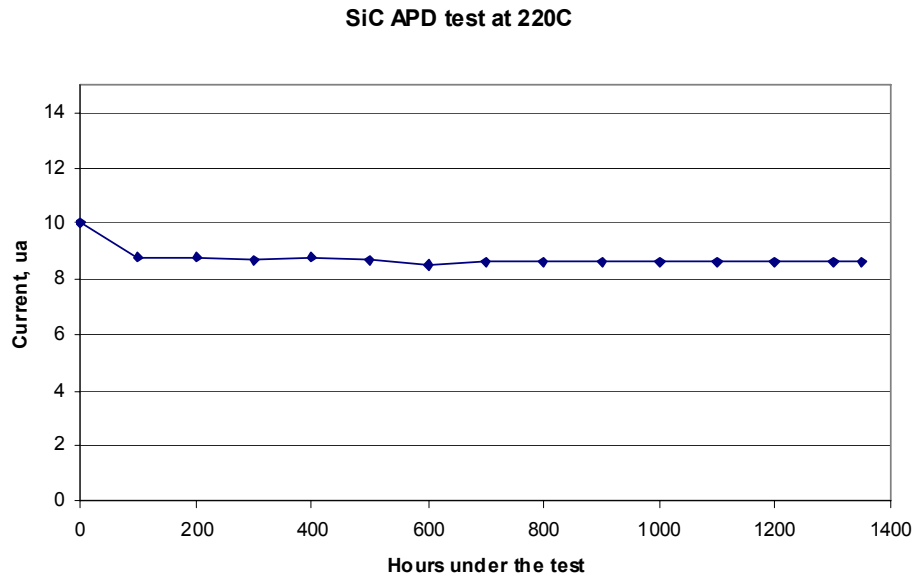


Figure 48. Current of selected APD tested at 220°C for 1,400 hours.

4. Task 11 - Development of reflector and optical coupling design

For the choice of the reflector, teflon has an excellent reflectivity in the UV (~98% at 300 nm). GE Reuter-Stokes uses this in their current gamma sensor and therefore had a well established process for drying and wrapping it around the scintillator, and was for this system. Other optical reflector approaches were considered, but would require major efforts and yield very little improvement from the current material.

For the optical coupler development, 26 materials were reviewed from current and past programs at GE Global Research, and were down-selected to 8 materials. To achieve the down-selection, a comprehensive list of performance criterion in the UV were used including: index of refraction, transparency, stability at 225 °C, thermal cycling stability, cost and several other factors.

In many cases, small test samples of these materials were provided to the team at no charge. The currently used optical coupler was included in the above candidates for testing.

The evaluation of these optical materials was conducted and properties of study included: UV transmission before and after cycling to 225 °C, lap shear strength after 100 thermal cycles going from -40 °C to +25 °C and -40 °C to +225 °C.

For these evaluations, a special tool to realize thin films of optical coupler material was designed and is shown in Figure 49.

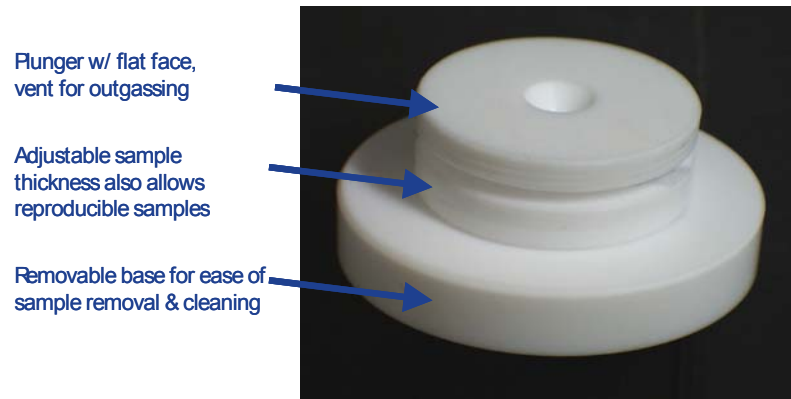


Figure 49. Tool designed to realize thin films of optical coupler materials for study.

The tool facilitates the fabrication of thin film samples of materials for study with good control over their thickness.

The reliability testing of material candidates for use as the optical coupler between the scintillator and the APD array were completed. This testing takes materials provided by various vendors and subjects them to high temperatures (225 °C) for extended periods of time. At chosen exposure times, the samples were removed from the heat and measured for optical transparency. Table 2 shows a list of those materials.

Table 2. Summary of the materials under study for optical coupling.

Cure	Conditions of note:	Cured Thickness (mm)	Initial Transmittance			Time	Temp
			300nm	325nm	350nm		
120' @ 100C		4.039	72.1	78.576	81.366		225 C
240' @ 80C		4.552	0.0084	21.685	61.447	24 hr	225 C
240' @ 90C		4.542	0.0069	17.277	55.556	24 hr	225 C
240' @ 100C		4.781	8.4384	34.699	52.687	192 hr	225 C
120' @ 90C	On order						225 C
None	Note film thickness	0.020	74.468	78.816	82.694		225 C
30' @ 150C	Unable to form void-free						
240' @ 65C		4.505	1.829	14.013	41.069	24 hr	225 C
120' @ 90C		3.902	0.0037	15.006	48.761	24 hr	225 C
120' @ 90C		4.156	0.0056	9.0588	26.02	24 hr	225 C
120' @ 100C	Arrived 6/6/06						225 C

As described in the table, the UV transmission was measured as this is perhaps the most important material characteristic in determining which material will be most suitable for use in the gamma sensor system. Figure 50 shows the measurements of UV transmission for several materials.

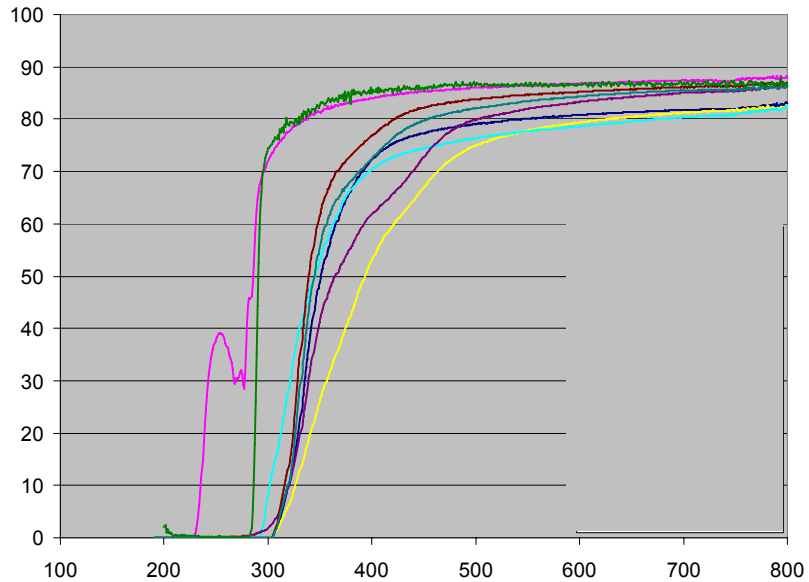


Figure 50. UV transmission of several candidates before exposure to high temperature.

The above table helps illustrate the process by which candidates are ruled out. Following exposure to high temperature, some of the materials degrade optically, and are therefore ruled out. An example of one of those materials is shown in Figure 51.



Figure 51. Material A at 0 (left) and 24 (right) hours of exposure to 225 °C in air.

The following observations were made:

- 1 failed at sample preparation
- 5 more failed after 24 hours @ 225 °C
- 1 more failed after 192 hours @ 225 °C
- 2 new materials are on-order or just received
- 2 materials showed good transmission in the UV

Testing at elevated temperatures of the candidate optical couplers continued beyond 800 hours. Only two materials showed good transparency in the UV (see Figure 52). All other materials either became opaque, or physically disintegrated rendering them useless for the gamma sensor system.

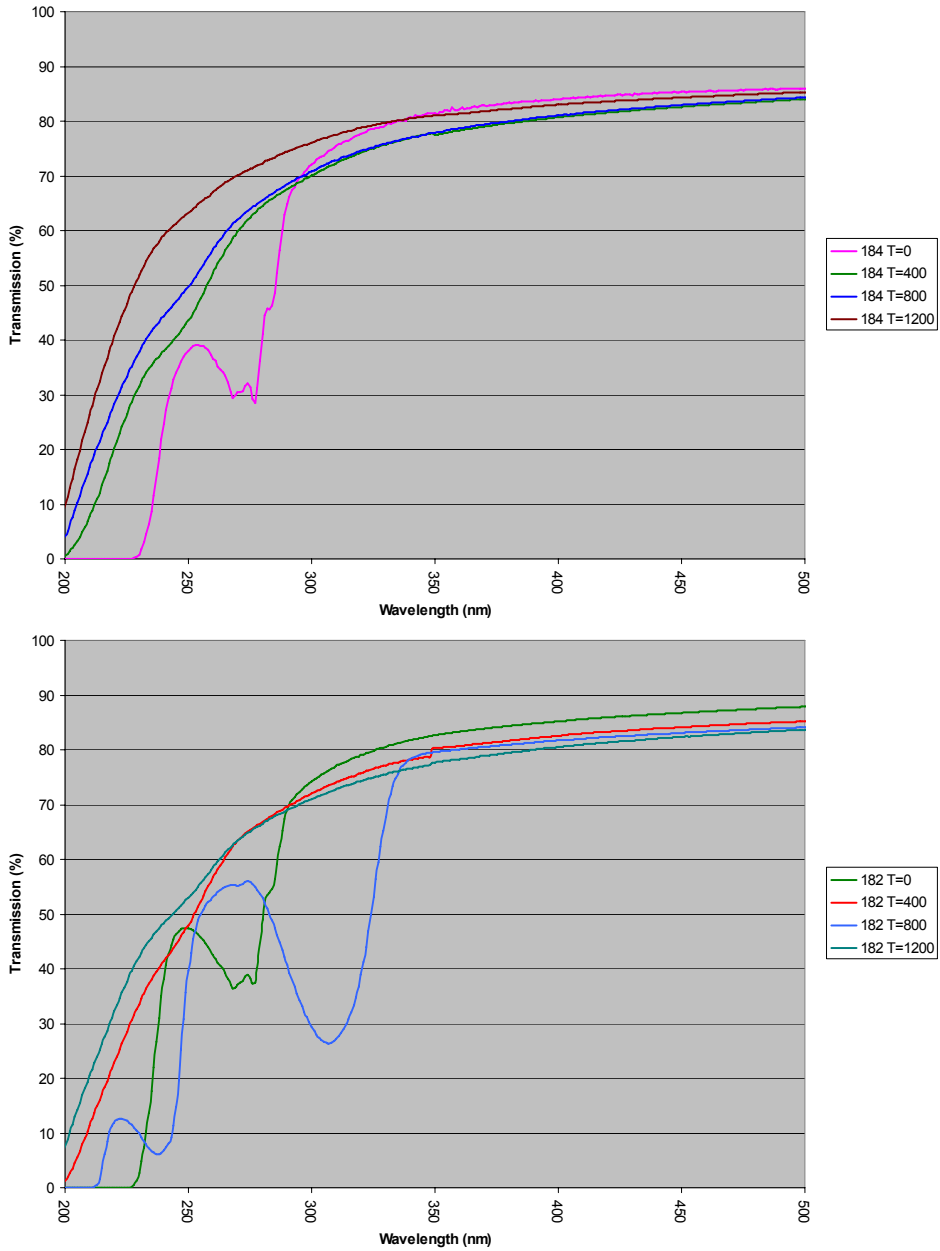


Figure 52. Transmission characteristics of the optical coupler candidates after various times at elevated temperature in air.

In the case of the Material B sample, its transparency in the region of ~270 nm has dropped significantly, making it the less desirable candidate of the two. As with Material C sample, however, its transparency has actually improved. It is suspected this may be due to oxygen gradually leaving the material. The consequence does appear to be that the material becomes more brittle over time. While a more brittle material may not be a problem as once it's integrated into a package, its position will not be changed.

If brittleness does become an issue, a hermetic package may be considered in an attempt to reduce the effect of apparent out gassing of the material.

Optical Fluid

Not shown in the gamma system diagram (**Error! Reference source not found.**) is the optical fluid used to eliminate air gaps between the scintillator and the quartz window, as well as between the optical coupler and the window on the other sides. The index of refraction of the fluid is closer to the optical materials (optical coupler and scintillator) than air, and it helps to cushion the components during vibration. While this fluid has been used in commercial systems, it's UV transparency was not known.

A study was thus done on the presently used gel (from Dow). The transmission was done on the material as received, then again after 12 hours of baking at 200 °C. A small decrease in transmission was observed after initial baking, with a ~5% reduction. However, the UV transmission is good throughout most of the UV.

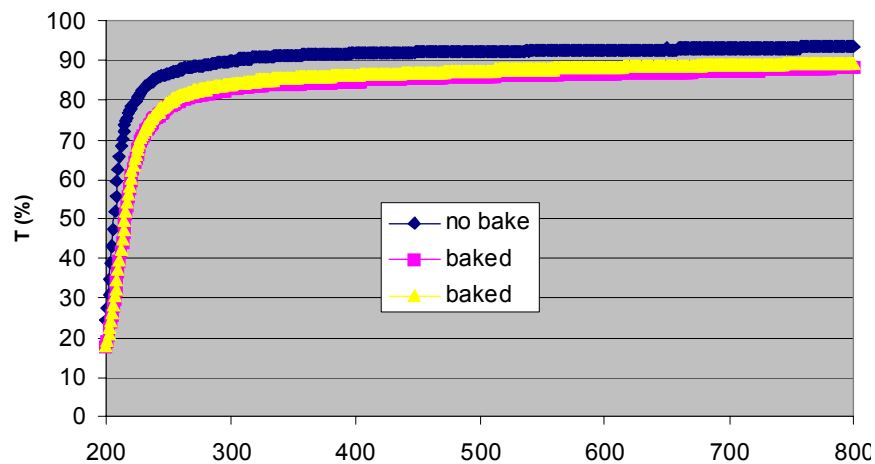


Figure 53. The transmission of the Dow optical gel is shown as a function of wavelength.

As a backup, an alternative material was also studied. This was a highly viscous gel, that required a sandwich be made using two sapphire wafers. The transmission of the sapphire wafer as well as the calculated value for the optical gel is shown in the Figure 57.

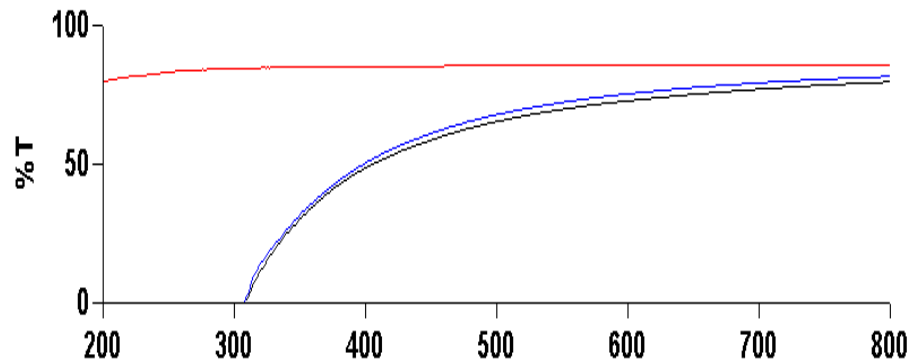


Figure 54. Optical transmission of an optical gel as a function of wavelength. The red curve is of a blank substrate (reference) and the blue and black curves are of two actual samples.

This material is a poor candidate given its very low transmission from 300 to 350 nm, where most of the light received from the scintillator gets used by the APD. This material was subsequently removed from the possible candidates.

Figure 55 shows a picture of the APD sub-mount carrier coated by aluminum film (left) and reflectance spectra measured from the Al-coating (right). A total four samples were measured. As expected, a reflectance of ~45-50% was detected in the primary range of interest.

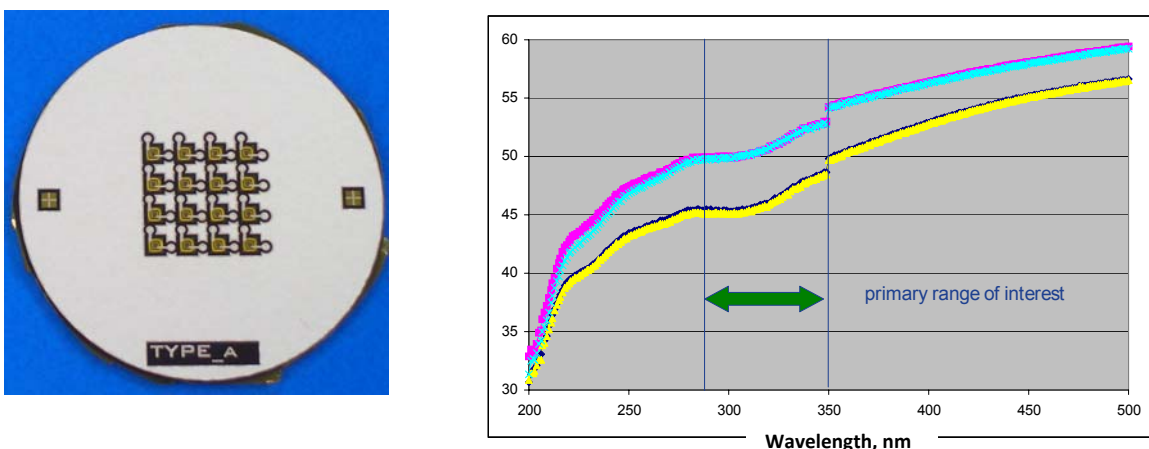


Figure 55. At left, the substrate with APDs (4x4 array) surrounded by the UV reflective coating. At right, the reflectance versus wavelength for the Al-coating.

5. Task 12 - Development of full crystals of selected scintillator material

This task followed directly from the work in Phase I identifying suitable candidate compounds for the scintillator.

5.1. Optical Modeling Of Scintillators

Optical modeling of scintillators was aimed at exploring the effects of surface roughness on the crystals. Keeping the basic cylindrical shape of the scintillator (as used today), the following features were explored as shown in Figure 56.

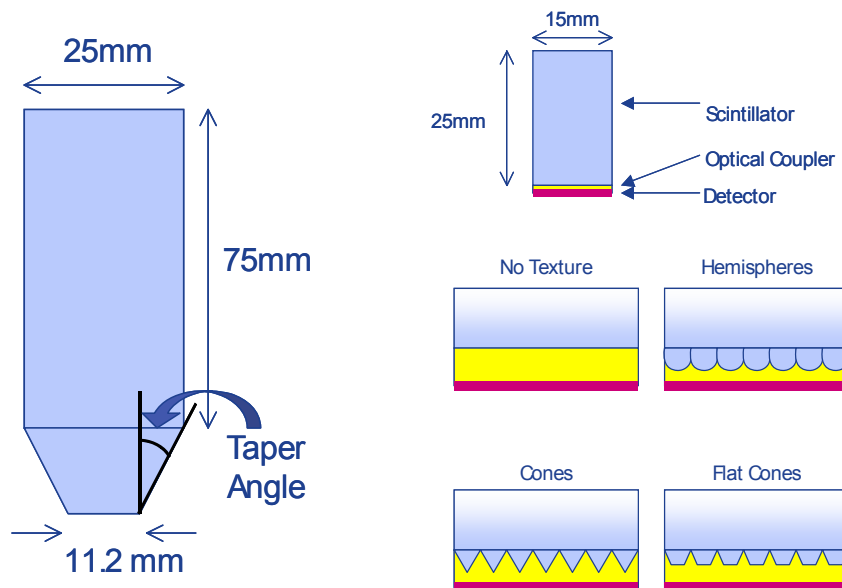


Figure 56. Scintillator shape components (left) and features (right) that were explored in various models to study their effects on light extraction.

An initial and expected finding was that the optical absorption (or transmission) properties were found to play a major role in determining the light extracted from the scintillator. For poor transparency in a given wavelength range of interest (i.e. a foggy

material), the light output on nearly all surfaces is substantially reduced. For spectral applications, where one wishes to determine the energy of the incident gamma ray, the uniformity of the crystal is also of high importance.

Subsequent studies looked at shaping the end of the cylinder in the interest of extracting more light, with feature examples as shown above. There, the following observations were made, as shown in Table 3.

Table 3. Summary of scintillator modeling of various features as shown in Figure 56.

Surface Type		Mean	Std Dev	Mean/Std
None	Smooth	0.637	0.0129	49.4
	Rough	0.607	0.0088	68.7
Hemispheres	R=0.1mm	0.669	0.0104	64.3
	R=1mm	0.656	0.0104	63.1
Cones	$\theta=11.3^\circ$	0.661	0.0083	79.2
Flat Cones		0.660	0.0082	80.7

The conclusion was that textured surfaces (e.g. those with specialized features) gave about 5 to 10% better light extraction. While this gain is helpful, the expected improvement from developing such a capability is moderate. Therefore a decision was made to forego special tailoring of the scintillator features.

5.2. *BaSiO₄* crystal

Following on the work from Phase I, the team at CUNY reported that a BaSiO_x precursor had produced encouraging results, with a crystal that has transparent sections and appears significantly more continuous than the past attempts (Figure 57).

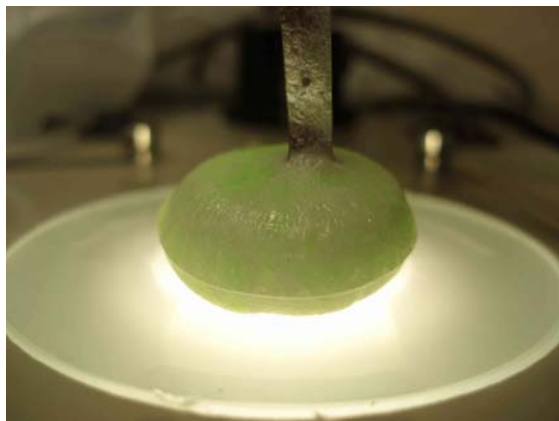


Figure 57. Picture of BaSiO₄ crystal growth from the CUNY sub-contract team.

It was also stated that an alternative set of scintillator materials had been identified for this program, in the event that BaSiO₄ did not avail itself to successful implementation in a system prototype. These materials showed good promise in a number of categories, including emission in the UV as shown in Figure 58.

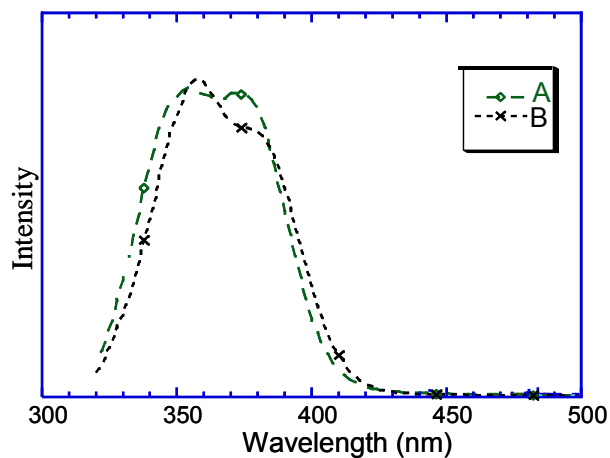


Figure 58. Light output of scintillator materials that are presently a backup for BaSiO₄ material.

Further, these scintillators are intriguing as they possess the potential for improved energy resolution in comparison to the currently used material, NaI, as shown in Figure 59.

	Nal:Tl	Alternative	Ba ₂ SiO ₄
Effective Z	50.44	47.14	51.16
density	3.667	4.58	4.5-5?
refractive index	1.85	about 1.9	1.7-1.8?
primary speed	230 nsec	25 nsec	25-50 nsec
delta E/E at 662 KeV	7%	4%	?
photons/ MeV rm temp	39,000	64,000	?
temp coef. of light output	-.25%/C	-.125%/C	+.23%/C
photons/ MeV at 200 C	22,000	50,000	?
peak wavelength	415 nm	365 nm	310 nm

Figure 59. Comparison of scintillator materials, including the "alternative" material, which is a backup to Ba₂SiO₄.

Those material evaluations were performed by a team led by GE Global Research on a different program, and that material was therefore leveraged as necessary for this project.

The development of barium silicate crystals at our sub-contractor, the City College of New York, was continued. They reported success in improving the crystals, and include the following notes in their summary about the growth process:

- Crystal growth temperature range is 1950-2050 °C
- Using 0.8*Ba₂SiO₄, 0.2*BaB₃O_x and 0.5*Ba₂SiO₄, 0.5*BaB_{1.2}O_x melt compositions
- The biggest problem is that seed crystals partially dissolve in the melt and fall off the holder
- Seed crystals are currently 5-7 mm single crystal regions obtained from polycrystalline boules. Larger seed crystals are needed (>10 mm) to prevent their dissolution.
- X-ray diffraction indicates that barium silicate is phase pure (only accurate to a few %) but transparency confirms that it is phase pure.

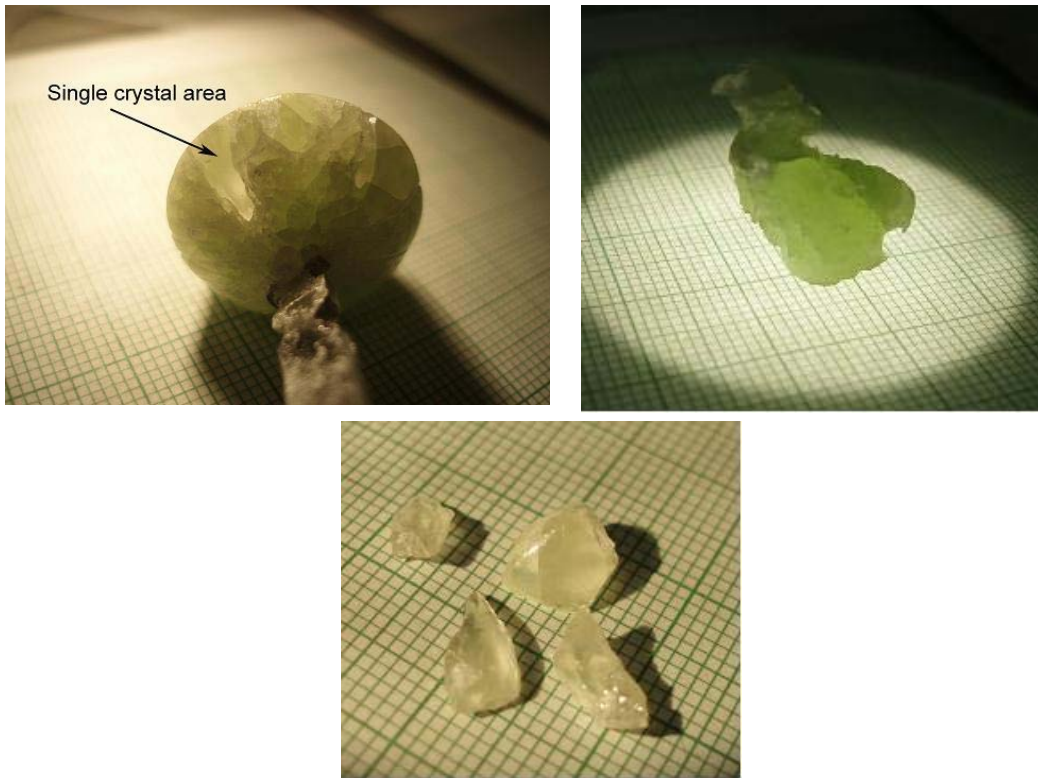


Figure 60. Figures from CCNY - CUNY showing progress with BaSiO_x growth.

In Figure 60, the top left image shows a Pr:Ba₂SiO₄ polycrystal grown on an Ir-plate without pulling. This polycrystalline boule contains large transparent single crystals. The growth rate was ~0.1-0.2 g/h. The top right image shows a Pr:Ba₂SiO₄ polycrystal grown on an Ir-plate using a pulling rate of 0.5 mm/h. Lastly, the bottom image shows Pr:Ba₂SiO₄ single crystals obtained from a polycrystalline boule.

This progress was positive in two highly important respects. First, the crystals showed much greater transparency, and second, the crystals were significantly larger than the initial attempts. While they could not grow crystals larger than 15 mm on a side due to equipment limitations, a steady improvement towards larger area crystals suggested this process may be manufacturable. The growth rates used in the above figures were comparable to currently used scintillators.

Following on the BaSiO_x crystal growth done at CUNY, a series of material characterizations were done to evaluate its potential use.

Basic material properties were first found, including the following:

- unit cell dimensions: 5.772 x 10.225 x 7.513 angstroms
- crystal system: orthorhombic K₂SO₄ type
- refractive indices: 1.63, 1.72, and TBD (couldn't get a clean surface in the third direction)
- measured density of our sample: 5.378 g/cm³
- calculated density: 5.493 g/cm³

Table 4. Compositional analysis of the barium orthosilicate samples from CUNY.

Customer ID	EA sample #	K ± 95% CI	Pr ± 95% CI	Method
Barium Orthosilicate polycrystal	S06-05230A	<0.05	0.32±0.01	1
	S06-05230B	<0.05	0.32±0.01	2
	S06-05230C	<0.05	0.32±0.01	2

Another important study was the evaluation of the emission and absorption properties of this material. Those are shown in Figure 61.

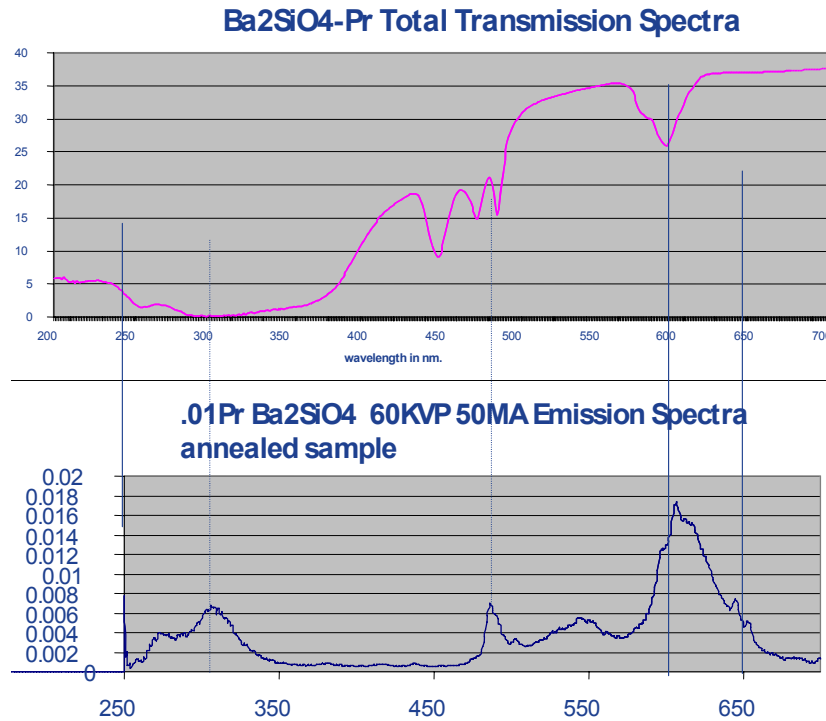


Figure 61. Optical properties of Ba₂SiO₄. Transmission shown in the top graph, and a corresponding plot of the emission spectra on the bottom. The x-axis is in nanometers.

The results show that while the barium orthosilicate emits in the UV as expected from powder studies, the transmission properties are quite poor, suggesting that nearly all of the light emitted in the UV around 300 nm where the SiC detector is very efficient, will be reabsorbed in the scintillator before it escapes the crystal. Before stopping the investigation on this material, the reflectance of these crystals was also explored, as shown in Figure 62.

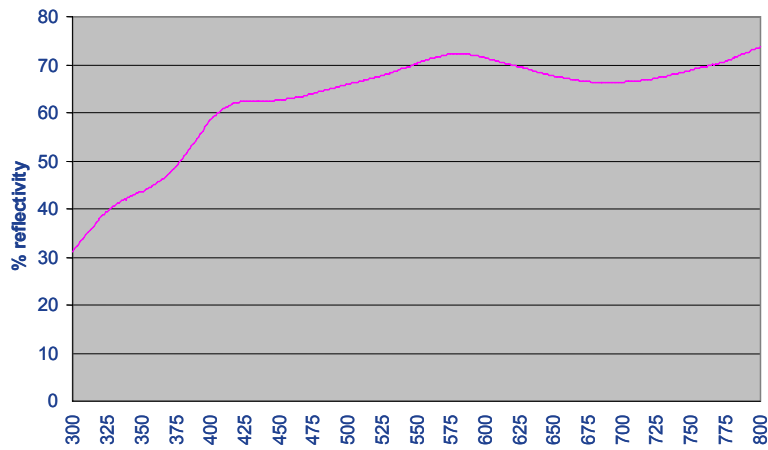


Figure 62. Optical reflectance of the barium orthosilicate material versus wavelength (nm).

Unfortunately, the reflectance measurement confirms that the material is absorbing significantly in the UV, and therefore rendering the material useless for our gamma sensor. This was the conclusion of the study on this scintillator candidate, and the corresponding collaboration and sub-contract work with CUNY.

5.3. $\text{Cs}_2\text{NaPrCl}_6$ crystal

The next candidate was $\text{Cs}_2\text{NaPrCl}_6$. This material had been explored in the past, and literature (see Figure 64) suggested it might have suitable output in the UV as required by the SiC APDs. Its crystal structure, shared with a mineral called elpasolite, is shown below in Figure 63.

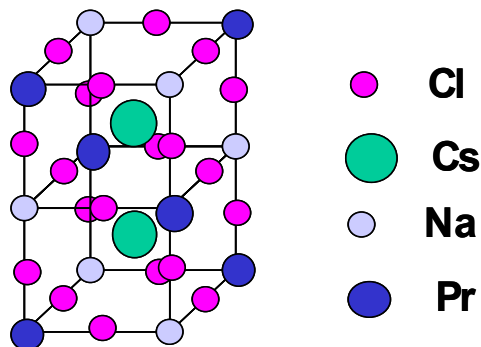


Figure 63. Ball and stick model of $\text{Cs}_2\text{NaPrCl}_6$.

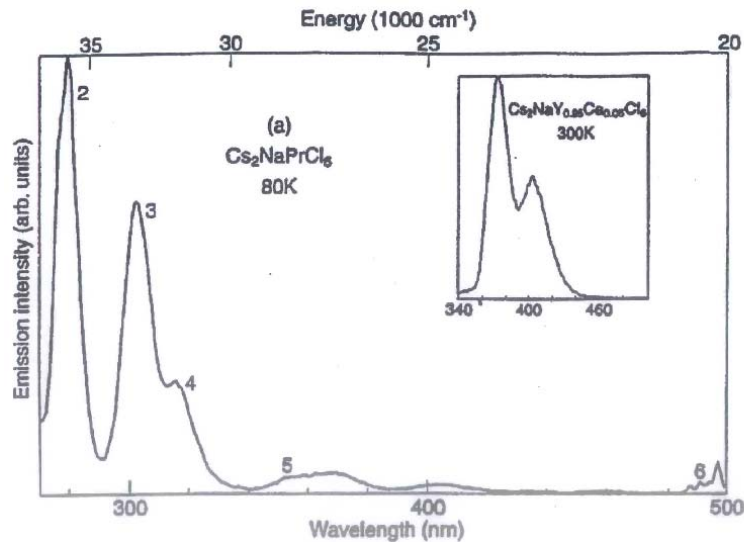


Figure 64. Emission intensity as a function of wavelength for $\text{Cs}_2\text{NaPrCl}_6$, as reported in Physical Review B, volume 67, article 115102 (2003).

This material was particularly interesting as a new 'find' for our study as it appeared much more straight-forward to grow than barium orthosilicate. An initial trial was performed at GE Global Research, and resulted in crystals as shown in Figure 65.



Figure 65. Photo of the initial trial growth of $\text{Cs}_2\text{NaPrCl}_6$. The adjacent rule has units of inches.

The resulting crystal was grown in a period of roughly two weeks, and attained a size of ~1 cm in diameter and was a few cm long. The growth temperature of this crystal was under 1000 °C, making its growth much more feasible than barium silicate while still having a high enough melting point to maintain a robust nature for down-hole drilling. A few cracks were easily observed, which may be due to the removal process from the quartz chamber. Also, although there is some apparent oxidation of this material, looking down the long axis of some of the crystal pieces, one can observe its largely transparent nature, a positive sign for usage in this system.

One disadvantage of this material is its hygroscopic nature, as it quickly absorbs moisture from the air. This requires its production and storage in an inert environment, in a similar fashion to NaI, the main stay scintillator material for gamma sensors currently. Thus, while it may be difficult to handle this material, the current gamma sensor package already had been engineered to address this problem as it's processed and packaged in a dry-room, then sealed in a chamber with a sapphire window, that's transparent into the UV past 200 nm.

Material studies of this new scintillator candidate resulted in the optical spectra shown in Figure 66. While there is strong absorption at wavelengths of 280 nm and below, the emission spectra overlaps nicely with the quantum efficiency of the SiC APDs, and avoids the region of high absorption.

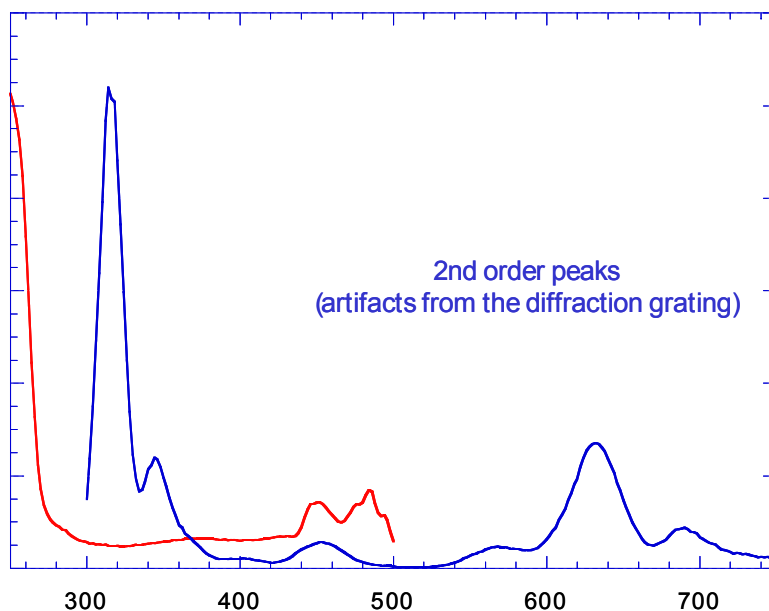


Figure 66. Optical properties of $\text{Cs}_2\text{NaPrCl}_6$. The red line shows absorption data while the blue line shows emission spectra from a 254 nm source.

Further characterization of $\text{Cs}_2\text{NaPrCl}_6$ showed that its output was only 6,000 photons per MeV, which is approximately one-half of the minimum efficiency targeted.

After revisiting the expected material properties and comparing past work done at GE, it was observed that 100% Pr was likely causing significant self-absorption, which may have resulted in a significantly reduced level of light output compared to a $\text{Cs}_2\text{NaLa}_{1-x}\text{Pr}_x\text{Cl}_6$ crystal with $x < 1$.

From the above data, one may observe that while the spectra does not seem to shift substantially in wavelength of emission, the light output drops significantly with decreasing Pr concentration. Figure 67 shows the light output for the five levels of Pr tested in crystal form.

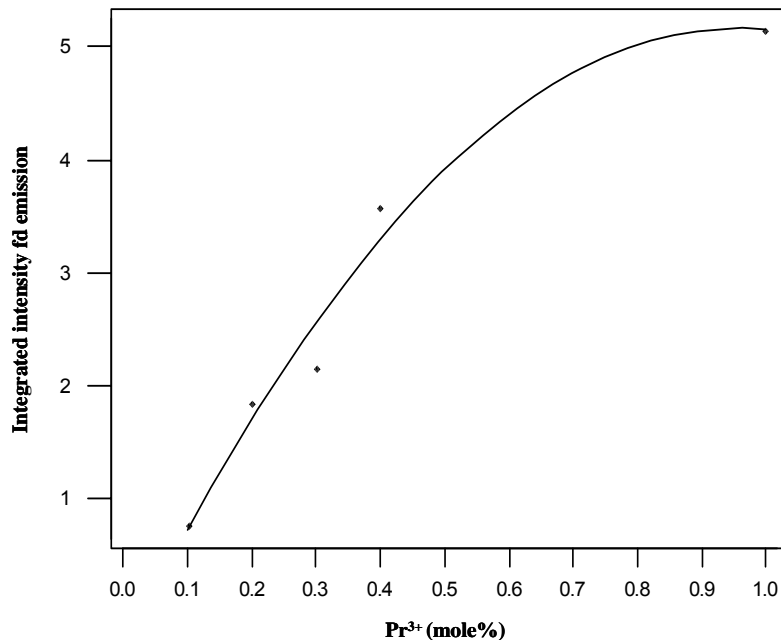


Figure 67. Relative light output, integrated from 250 to 400 nm, for $\text{Cs}_2\text{NaLa}_{1-x}\text{Pr}_x\text{Cl}_6$ as a function of Pr/La mole fraction.

It is important to note that in none of these cases, have the crystals been polished, which may result in a reduction in the observed light output. The tests for optical properties are also complicated by the hygroscopic nature of this material system, requiring a nitrogen atmosphere during all tests and handling.

The next step in this task was to polish the crystal with $x = 0.4$ Pr to determine if the rough surface is limiting the observed light output, and also to accurately assess the

number of photons per MeV we're getting from these materials. If the $\text{Cs}_2\text{NaLa}_{1-x}\text{Pr}_x\text{Cl}_6$ materials do not prove feasible for the gamma sensor prototype either due to low light output or other issues, GE planned to use another scintillator currently under study at GE Global Research.

The last elpasolite material grown ($\text{Cs}_2\text{NaPr}_{0.4}\text{La}_{0.6}\text{Cl}_6$) has been studied for its optical properties. It was subjected to different radiation energies, as shown below in Figure 68.

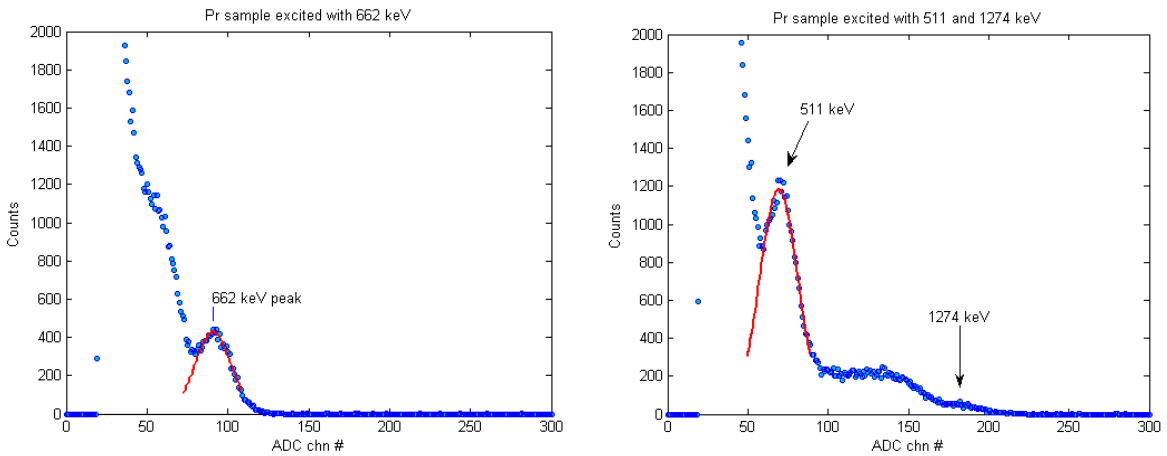


Figure 68. Pulse height spectrum of $\text{Cs}_2\text{NaPr}_{0.4}\text{La}_{0.6}\text{Cl}_6$ excited with ^{137}Cs (at left), and with excited with ^{22}Na (right).

In these measurements, the sample was centered on a H6610 Hamamatsu PMT. A fast 1" \varnothing , 8-stage tube with fused silica window and bialkali cathode was used with a shaping time of 4 μs for the amplifier. The setup is depicted in Figure 69.

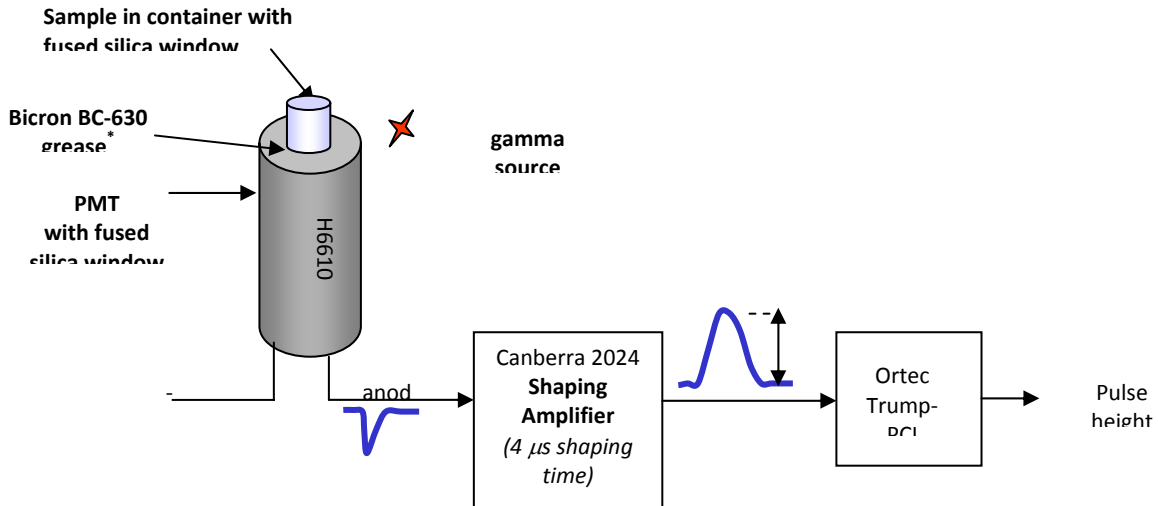


Figure 69. Scintillator testing setup used for elpasolite materials study.

The light output from the $\text{Cs}_2\text{NaPr}_{0.4}\text{La}_{0.6}\text{Cl}_6$ was measured in comparison to BaF_2 , which has a known emission level. That result is shown in Figure 70.

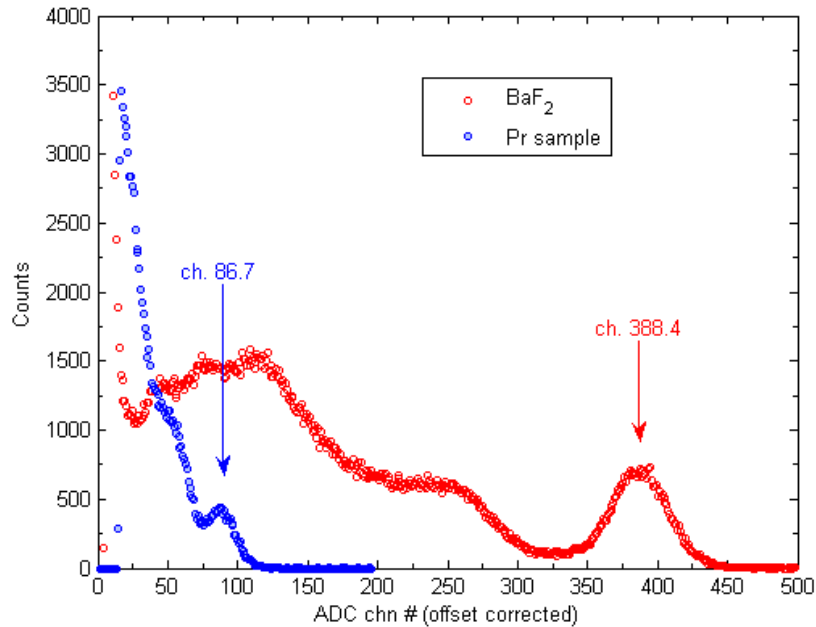


Figure 70. LO measurement of $\text{Cs}_2\text{NaPr}_{0.4}\text{La}_{0.6}\text{Cl}_6$ relative to BaF_2 for 662 keV.

The ratio of the elpasolite emission to that of BaF_2 was approximately 20%, suggesting its light output of the $\text{Cs}_2\text{NaPr}_{0.4}\text{La}_{0.6}\text{Cl}_6$ is approximately 2,400 photons per MeV, making it far too dim for use in the gamma sensor. However, the optical materials used in the measurement were not UV transparent, so it was likely that the full extent of the UV output from this crystal was not captured.

5.4. Lanthanum halide (LaX_3) crystals

With the questionable prospect of the elpasolite materials, our next likely replacement was the lanthanum halide (LaX_3) system. This material system has strong output in the UV, and very high light output overall. Figure 71 shows some light output data for some probably combinations of LaX_3 crystals, and some properties are listed in Table 5.

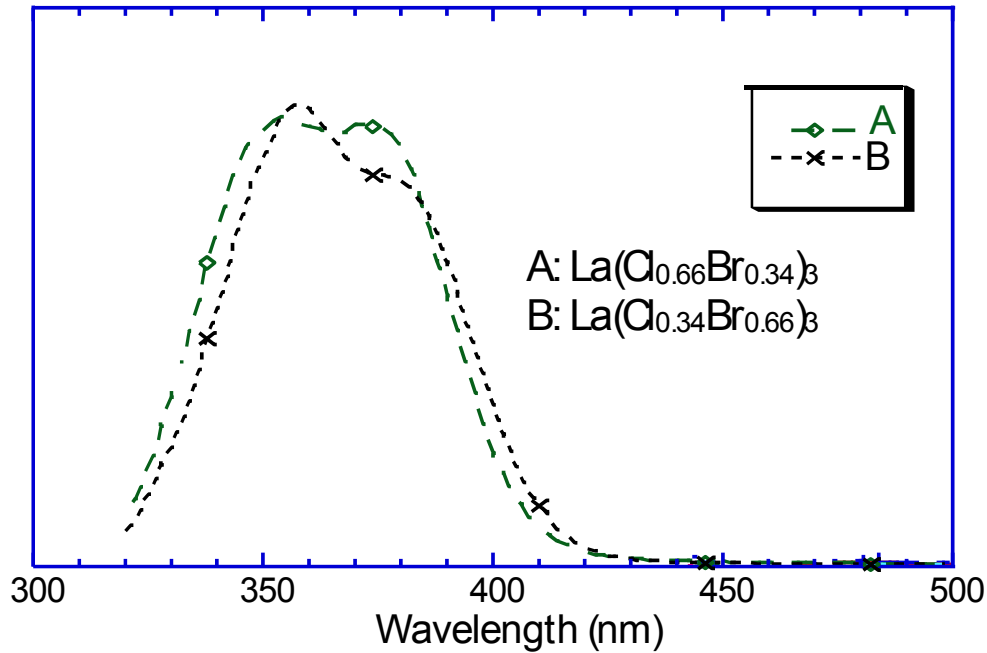


Figure 71. LaX_3 sample compounds light output intensity as a function of wavelength. Some of the properties of this material are compared with the presently used NaI in the subsequent figure.

Table 5. Table of some scintillator properties of LaX_3 materials doped with Ce compared to NaI.

	NaI:Tl	$\text{La}_{.97}\text{Ce}_{.03}\text{Br}_{1.5}\text{Cl}_{1.5}$
Effective Z	50.44	47.14
density	3.667	4.58
refractive index	1.85	about 1.9
primary speed	230 nsec	25 nsec
delta E/E at 662 KeV	7%	4%
photons/ MeV rm temp	39,000	64,000
temp coeff of light output	-.25%/C	-.125%/C
photons/ MeV at 200 C	22,000	50,000
peak wavelength	415 nm	365 nm

The most promising of the properties is possibly the very high light output from these crystals, although the spectral match to the APD will allow only a portion of the emission detected. GE Global Research and GE Reuter-Stokes produced several crystals of this material of 1 inch long by 1 inch diameter.

As it show in Figure 72 LaCl₃ and LaBr₃ crystals have very similar quantum efficiency, but the emission spectra is shifted. The lower density of LaCl₃ results in 17% fewer 700 KeV gamma rays stopped in a 1/2 in. dia. by 1/2 long crystal (Figure 73).

Figure 74 indicates that the spectral response of the APD strongly favors LaCl₃, overcoming its lower density penalty. As shown in Figure 75 LaCl₃ is preferred even after the increased brightness and stopping power of LaBr₃ are taken into account.

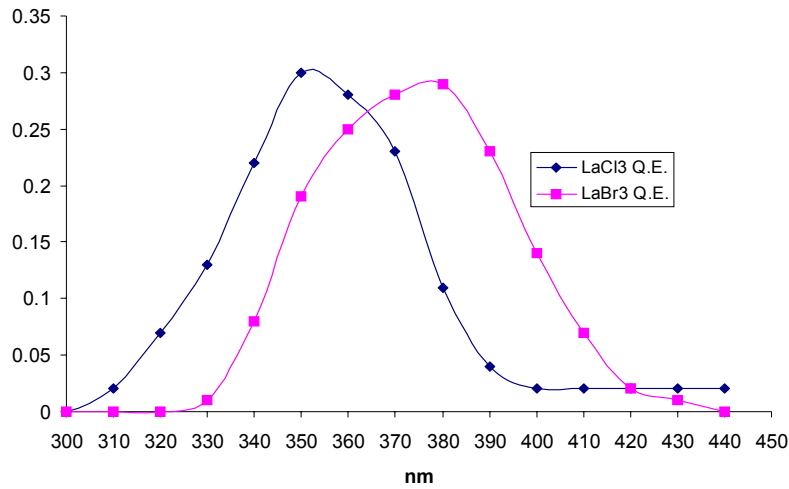


Figure 72. quantum efficiency spectra of LaCl₃ and LaBr₃ crystals.

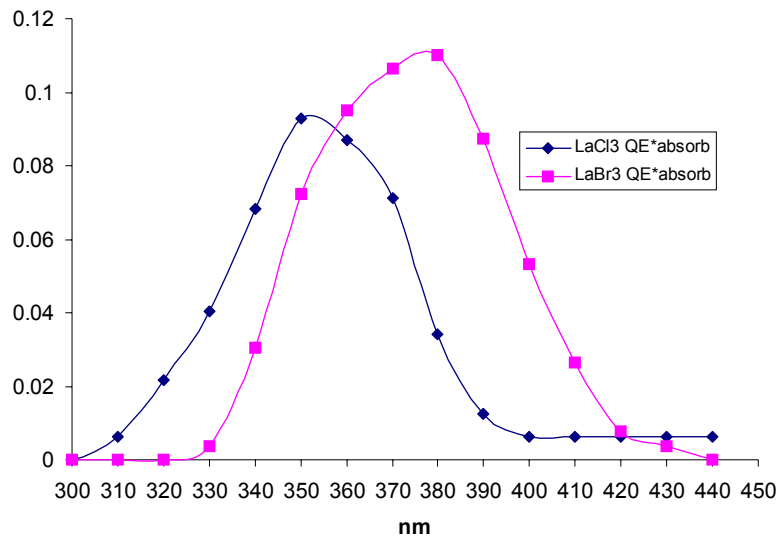


Figure 73. Quantum efficiency multiplied by gamma ray absorption factor for 1/2 inch crystal.

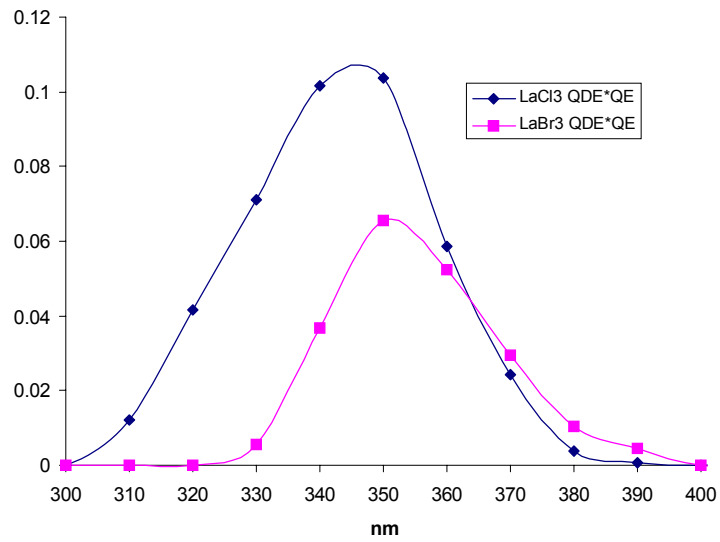


Figure 74. Product of QDE*QE*Absorption in .5 in crystal at 700 KeV.

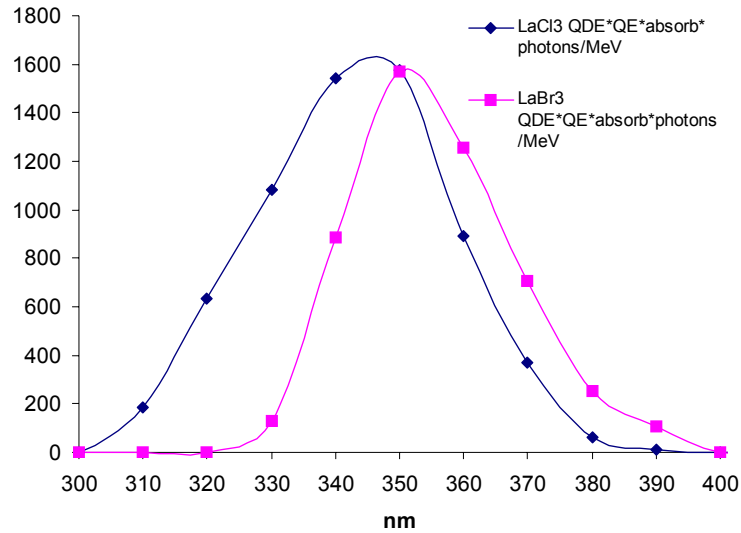


Figure 75 QDE*QE*absorb*photons/MeV for 1/2 inch dia. by 1/2 inch long crystal.

Analysis of the absorption factor for a crystal of 1.2 cm diameter and 1.2 cm long. Is shown in Figure 76. This analysis assumes that the quantum efficiency and photons/MeV changes linearly between LaBr3 and LaCl3. By further examining the known light output properties of LaX₃:Ce compositions (going from X = 100% Cl to 100 % Br), the APD-scintillator combination's system performance was predicted as shown below.

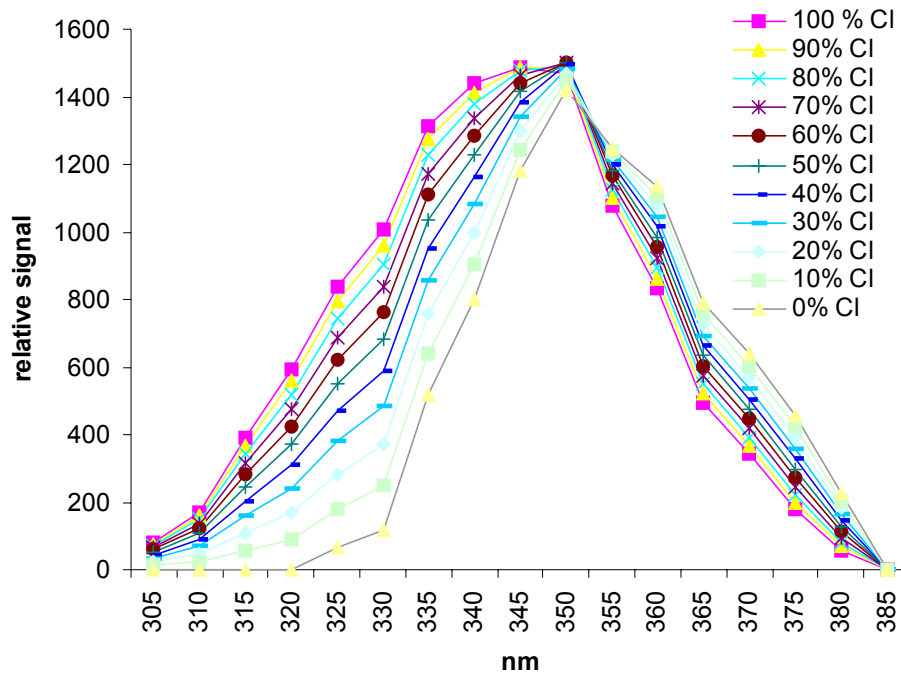


Figure 76. 230 C QDE*QE* photons/MeV*absorption factor

Following on this work, the scintillator crystal, which will be comprised of a 1/2 inch long by 1/2 inch diameter cylinder of $\text{LaBr}_3:\text{Ce}$, was reviewed for its eventual contribution to system performance. Data in the literature suggests that the drop-off in light output with increasing temperature should be relatively small. By extrapolating the observed light output to 200 °C, a reduction of ~21% was expected. The light output from the LaBr_3 crystal within a band of 320-380 nm (matching spectra with 4H-SiC APD) was measured in comparison to BaF_2 , which has a known emission level. That result is shown in Figure 77.

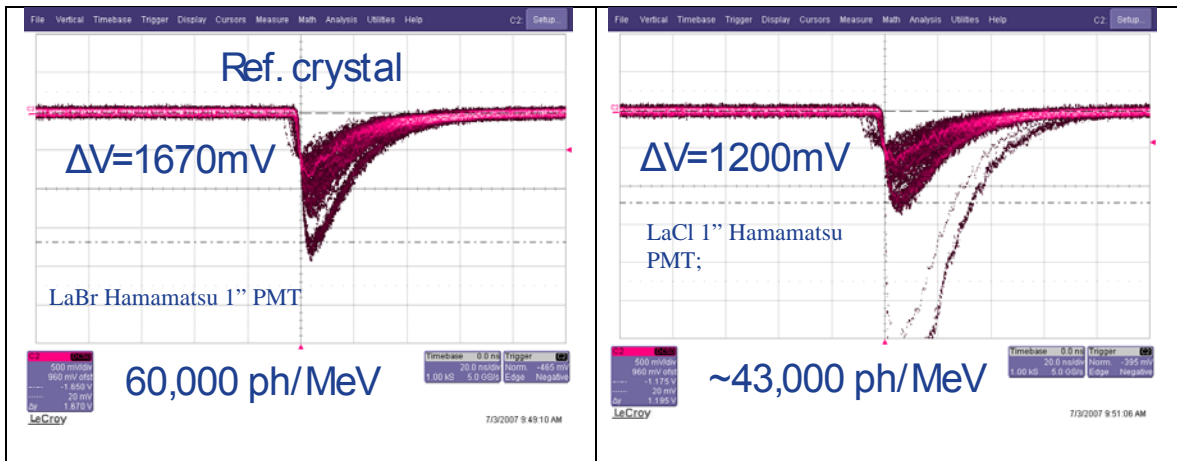


Figure 77. Light output of LaBr_3 crystal within a band of 320-380 nm.

The light output from the LaBr₃ crystal within a band of 320-380 nm was ~30,000 ph/MeV. From this finding, the best composition of the above possibilities is for 100% Cl. There are some limitations on this, primarily due to the difficulty with obtaining large crystals at this early research stage.

6. Task 13 - Development of prototype amplification system

6.1. APD signal model

An electrical model of the detector output with various design parameters was generated. A number of assumptions were made concerning the characteristics of the scintillator, the optical coupling material, the APD and the overall fill factor. These assumptions were continually refined and augmented to improve the accuracy of the model. The generated model was used as the input to the signal conditioning electronics for the purpose of performing the circuit analysis and simulation as well as identifying the various noise and count rate limitations.

The resulting APD model constituted a pulsed current source in parallel with a capacitor equal to the APD capacitance. The DC value of the current corresponded to the APD's dark current, the pulse amplitude corresponded to the charge generated by one gamma event, and the pulse width corresponded to the pulse shaping resulting from the time constant of the scintillator and the APD.

The system performance was limited by the various noise contributions in the system. The following three sources were identified and quantified

1. Detector shot noise
2. Front-end amplifier thermal noise
3. Front-end amplifier flicker noise

The model connected the design and system parameters to these three noise sources. Contributions from each of the noise sources were evaluated to ascertain the impact on the electronics architecture and overall system performance.

The detection limit of the system is constrained by the noise floor in the system, and the shaping time of the sensor interface circuit.

The noise in the system may be divided broadly into two components: voltage noise and current noise. The shaping time of the system affects the contribution of these noise sources differently. For instance, the voltage noise is reduced at longer shaping times.

On the other hand, current noise increases at long shaping times. An optimum point is obtained when the current noise contribution equals the voltage noise contributions. At that optimum point, the lowest noise level is obtained, and, hence, the highest signal to noise ratio.

At low gamma energy levels, a small number of photons are generated in the scintillator. A number of these photons are lost due to the coupling efficiency losses, absorption, and other loss mechanisms. The number of photons that successfully generate electrons in the APD determine the signal that needs to be detected in order to successfully register the gamma event. The higher the energy of the gamma event, the more electrons are transferred to the electronics, and thus the less important the contribution of noise becomes. The noise floor is therefore an important parameter in determining the lowest energy that can be reliably detected by they system.

Parameters such as the detector dark current, detector capacitance, thermal noise of the front-end electronics and the shaping amplifier topology all affect the noise floor of the system and were therefore modeled. Table 6 shows an excerpt of an excel sheet that includes the input parameters of the model.

Based on these parameters, the equivalent noise charge can be calculated as a function of shaping time. Figure 78 shows the noise contribution (in electrons) of a system. It can be seen that for the set of input parameters shown in Table 6, the lowest noise of about 9300 electrons is obtained at a shaping time of $\sim 50 \mu\text{s}$.

The shaping time limits the maximum number of counts that can be registered by the system. For this system, since count rates are expected to be on the order of 200 counts per second, shaping times as long as 1 ms are possible, and thus the electronics can be designed for the optimum shaping time.

Table 6. Summary of input parameters to the electronics model.

Environment		
Temperature	225	Celsius
Detector		
Number of elements	16	
Dark current per element	10	nA
Element capacitance	15	pf
Total dark current	160	
Total detector capacitance	240	
First Amplifier stage		
Frontend bias current	1	nA
Gate capacitance	5	pf

gm	1.00E-02	
Feedback resistor size	10	M Ω
Feedback capacitor	2	pf
Total current	161	nA
Total Capacitance	245	pF
Noise Calcs		
Shot noise	2.27135E-13	A/rHz
Feedback resistor noise	5.24508E-07	V/rHz
Thermal Noise	3.00E-08	V/rHz

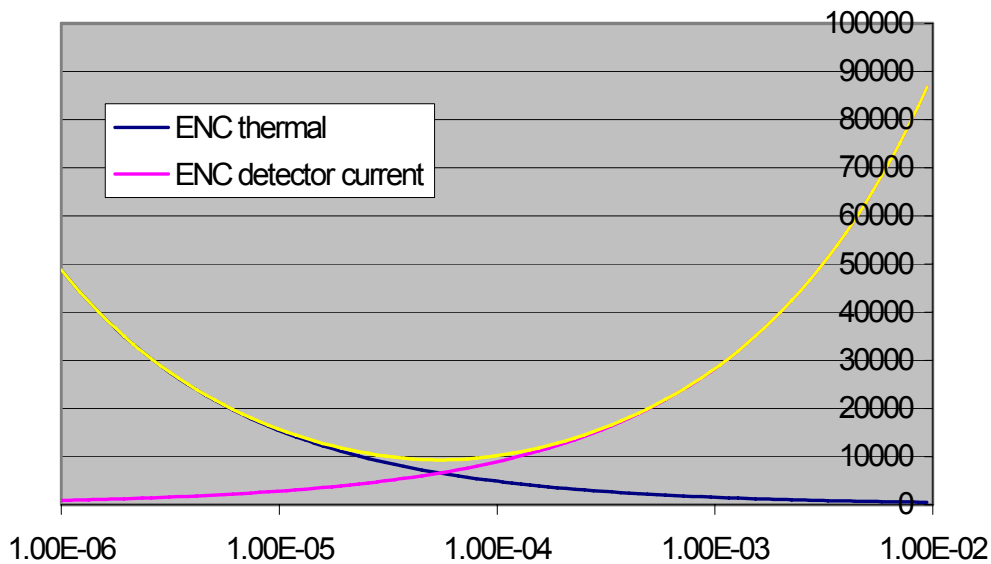


Figure 78. Equivalent noise charge (in electrons) versus the shaping time (in seconds) on the y and x-axis, respectively.

6.2. Electronics Architectures

The overall electronics architecture were identified, performance limits were evaluated, and the overall signal chain simulations were performed. A circuit simulation program based on the Spice simulation engine was used for performing the transient, frequency domain and noise simulations.

The signal conditioning electronics architecture constitutes:

- Charge Sensitive amplifier: integrates the impulse charge from the detector and outputs a step signal.

-
- Pulse shaper: increases SNR and generates trigger for pulse processing
 - Pulse processing: Comparator and event counter

The overall signal conditioning block diagram is shown below in Figure 79.

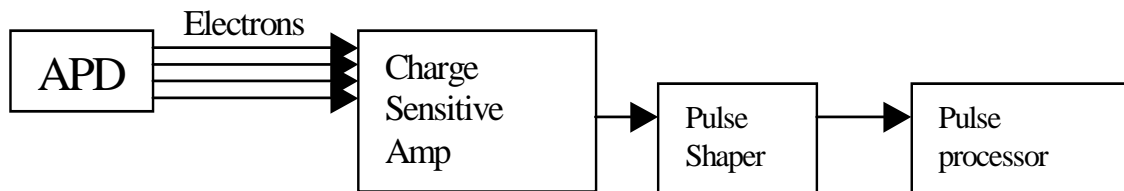


Figure 79. Signal conditioning block diagram.

The signal level at the output of the charge sensitive amplifier depends on the input signal level and the feedback capacitor size. A smaller capacitor is desired for maximum gain, but very small capacitances are not feasible since parasitics begin to dominate.

Because the expected APD output is on the order of a few thousand electrons, it is important to lower the noise contribution whenever possible to ensure accurate event detection. The pulse shaper is a band pass filter that limits the bandwidth of the system, and is tuned to pass the signal of interest in as small a bandwidth as possible to limit the noise contribution.

The pulse processor compares the resulting shaped pulse to a threshold and generates a trigger signal when an event is detected. The trigger then goes to a counter to obtain the number of counts over a given period of time.

Two electronics boards were designed. One had a very low noise input amplifier (reducing the thermal noise contribution from the electronics, and thus favoring shorter shaping times). This design was intended to operate at room temperature for the purpose of characterizing the noise performance at low temperature and also to overall performance of the system assuming no limitations imposed by the availability of high performance high temperature electronic components. The second board was designed to use available commercial off the shelf SOI (silicon on insulator) components, and was intended to demonstrate the capabilities of the system at high temperature using a representative set of available high temperature electronics.

Alternate shaping filters were explored to improve the noise performance. Initial literature survey and analysis showed that a simple CR high pass filter followed by n-stages of RC low pass filters had ~86% of the performance of a theoretically ideal pulse shaper. Thus, improvements on that architecture may result in a marginal gain in noise performance.

With architecture candidates as those shown above, GE have explored multiple simulation tools including SPICE, which allow for a time-domain estimation of signal propagation throughout a given arrangement.

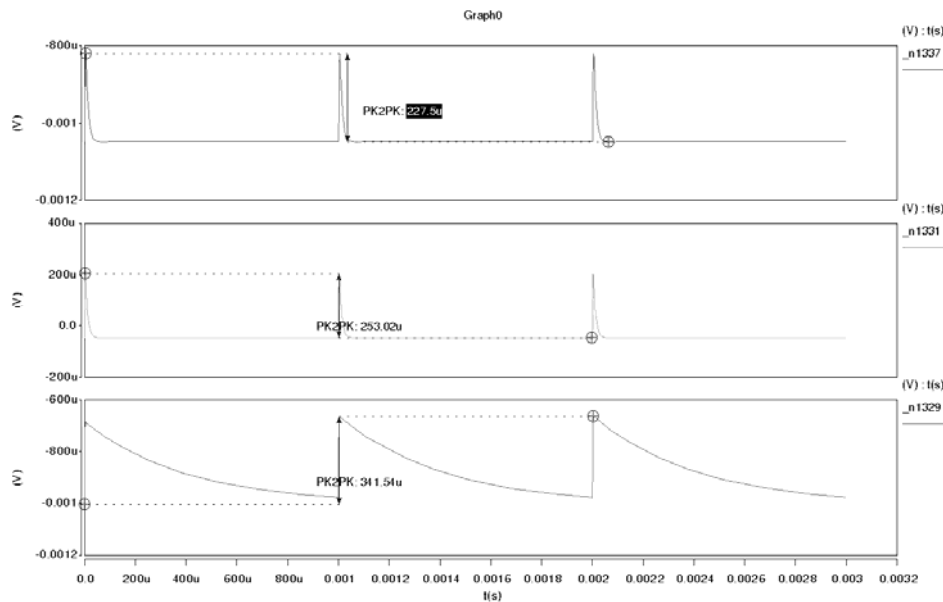


Figure 80. Circuit simulation of the above arrangement.

Since it was anticipated that noise was the limiting factor in the high temperature gamma sensor system, alternate shaper architectures were evaluated. In this application, due to the low count rate, alternate pulse shapers that stretch the event duration may provide added opportunities for more aggressive noise bandwidth reduction. These alternate architectures tended to also increase the electronics complexity, and therefore the efforts on the alternate architectures started with simulating the architectures mathematically first using tools such as Matlab, and then using Saber (a circuit simulation program).

Four electronic amplification schemes were simulated for the in our gamma sensor system, to multiply signals output from the APD for input to the end-user data collection unit.

There is no major advantage or disadvantage to any of these approaches, and as they are straight-forward and a hardware version of all of them was drawn in CAD and realized using standard components. An example of that is shown in Figure 81.

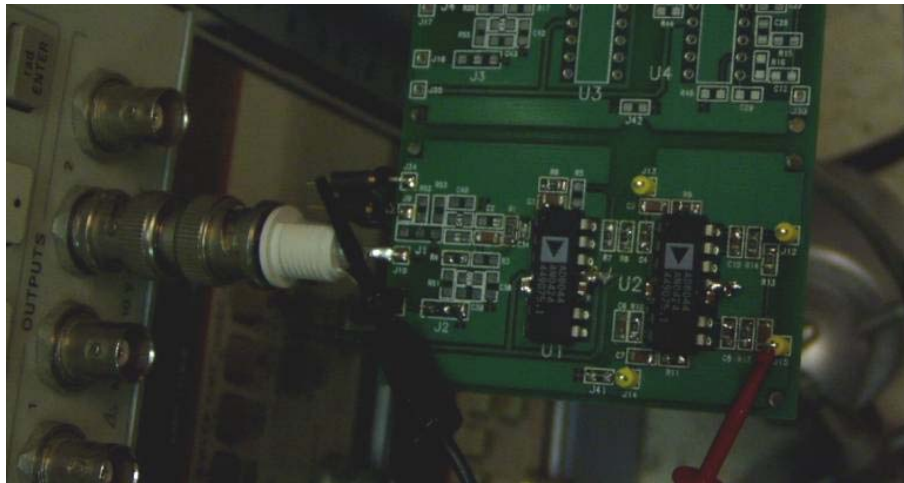


Figure 81. Four arrangements realized in hardware form for testing with an oscilloscope.

The above setup was used to simulate pulses from our APDs. For the charge sensitive amplifier, various levels of currents and voltages were used to examine noise levels observed. An example pulse is shown below for an 'event' or pulse from a pulse generator. Various staging approaches may be explored using this setup along with capacitors at the output. In one case, a 500 μV of input voltage results in approximately 3000 electrons of noise, which is in agreement with our earlier simulations.

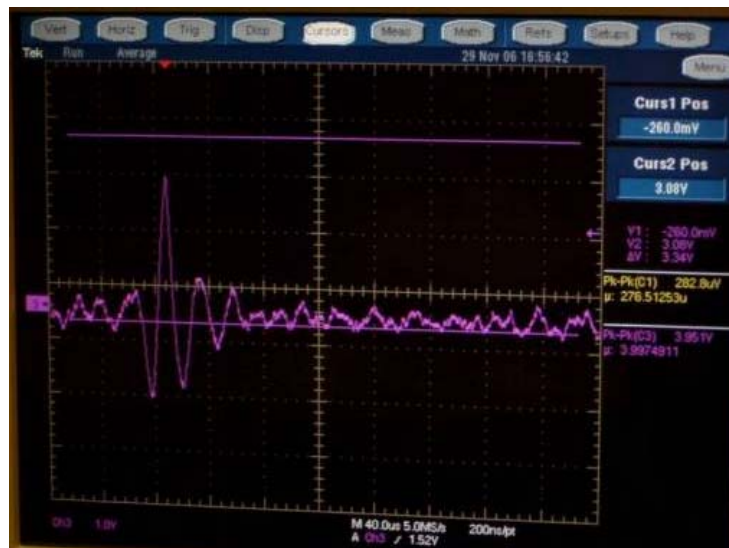


Figure 82. Amplification electronics output in response to a pulse generator.

These electronics were built using standard silicon components, however, they were rated to 150 or 175 °C in general. Thus, corollary versions were built using silicon on insulator (SOI) components which can withstand temperatures of 225 °C.

7. Task 14 - Assembling and evaluation of full detector system

The prototype gamma sensor system was separated into two pieces, namely, a front-end, which included the scintillator crystal and its supporting mechanical supports, optical reflector and the hermetically sealed housing, as well as the back-end, which included the optical coupler, APD array and amplification electronics.

The system uses some of the basic packaging components in GE Reuter-Stokes' commercial systems, and adopts its basic form factor. The final detail remaining in this system design is the connector arrangement that ties the APD array sub-mount (orange disk) to the electronics boards (green and brown). This is done using GE flex electronics technology as shown in Figure 41.

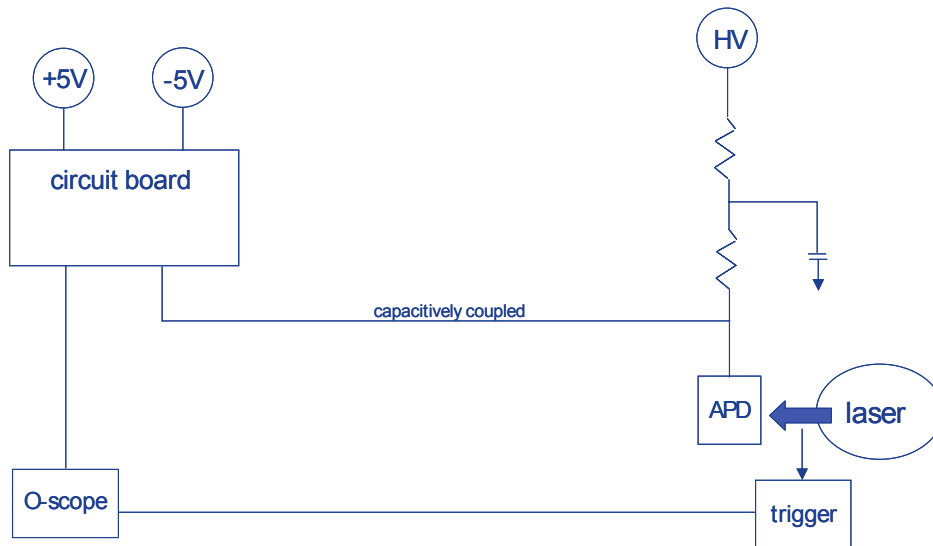


Figure 83. Schematic drawings of set-up for an optical test.

Prior to testing the full system with scintillator crystal, optical tests of the assembled APD arrays with electrical boards were performed using a laser pulse 266 nm photon source of estimated 1,400 photons per pulse. Schematic drawings of the experimental test set-up for such a test is shown in Figure 83.

Figure 84 shows (a) a photograph of the electrical board with mounted APD array on it and (b) a scope image of registered dark counts (noise). The noise remained approximately the same when a high voltage supply slowly stepped up from 10V to 580V. Above 580V, noise slightly increased, and above 610V, noise increases rapidly. At a voltage of 620V current was less than $1\mu\text{A}$ which indicated that no catastrophic APD failure have occurred.

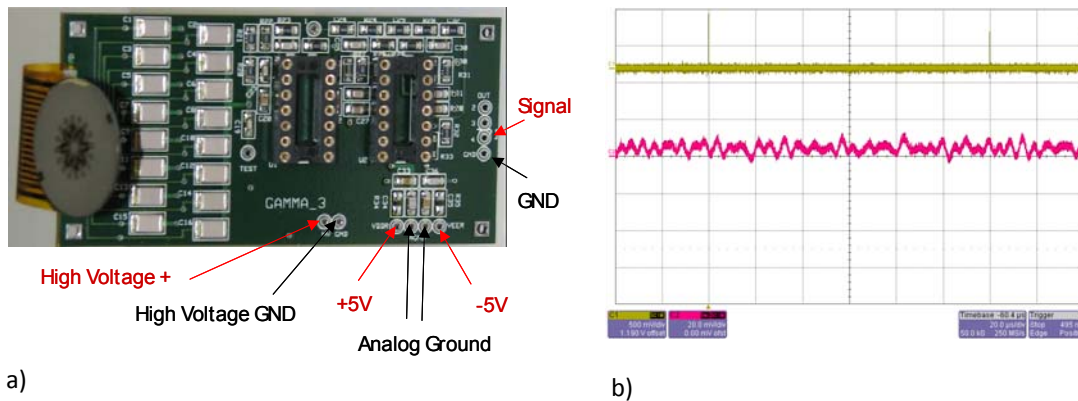


Figure 84. (a) photograph of APD array mounted on the electronic board, (b) scope image of dark counts.

Dark current and optical gain curves of the APD array vs. an applied voltage are shown in Figure 85. Optical gain of the APD array was more than 100 at $U > 610\text{V}$.

Figure 86 shows optical responses of the APD array to the laser pulses (left) and histograms which were made on the o-scope to illustrate the distribution of pulses vs. time (right). Signal-to-noise ratio varied from 1.5 to 2.5, while gain varied from 90 to 200 for different APD arrays (total 6 arrays tested). Minimum number of detected photoelectrons/pulse was found to be ~ 300 and the best threshold between dark counts and laser pulses was at a bias of 605V

Optical responses of the APD array to the laser pulses at optical gains of 100 and 10 are shown in Figure 87. Based on the data we expect the optimum operating optical gain would be between 10 and 100.

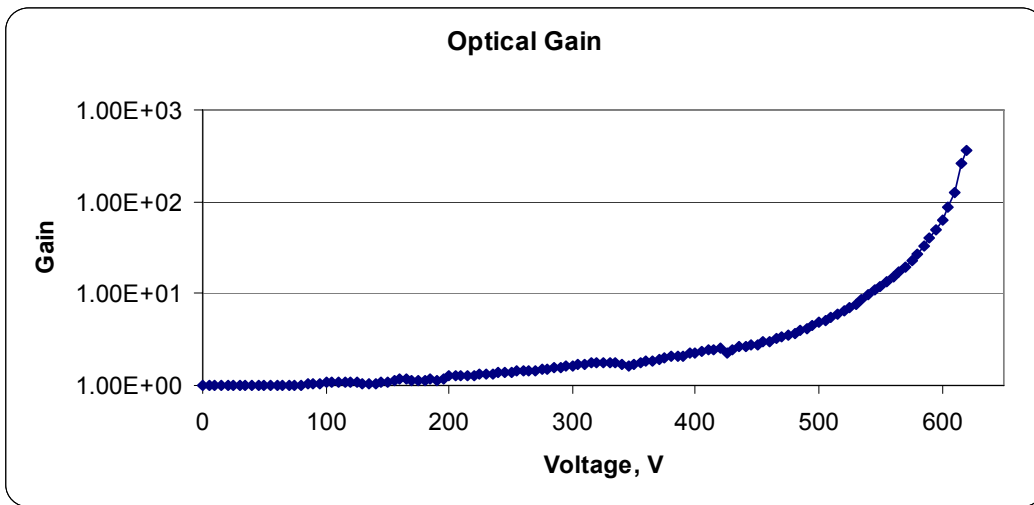
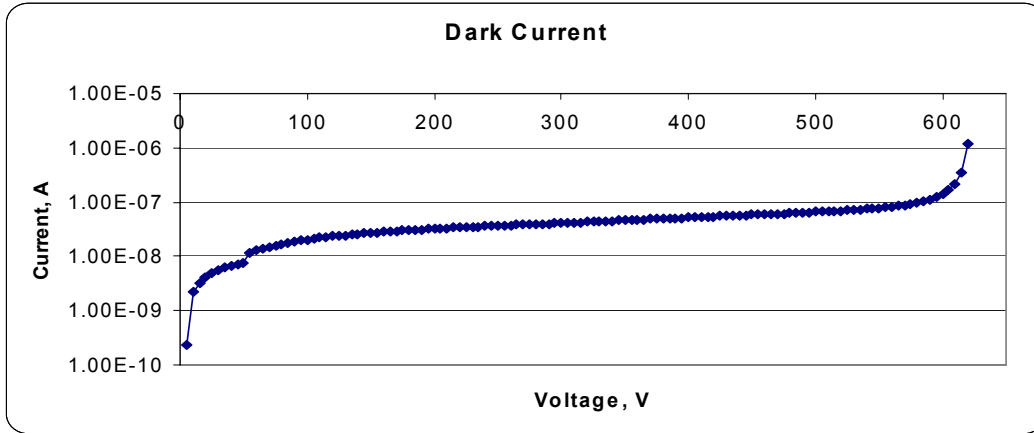


Figure 85. Dark current and optical gain curves of the APD array vs. applied voltage.

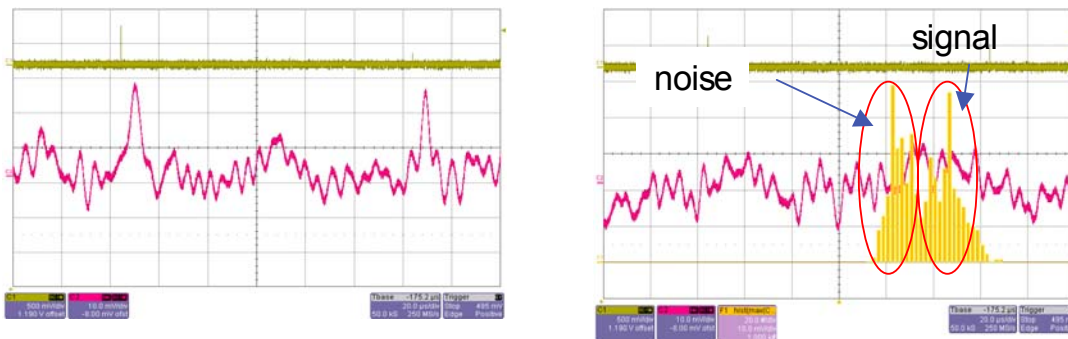


Figure 86. Optical responses of the APD array to the laser pulses

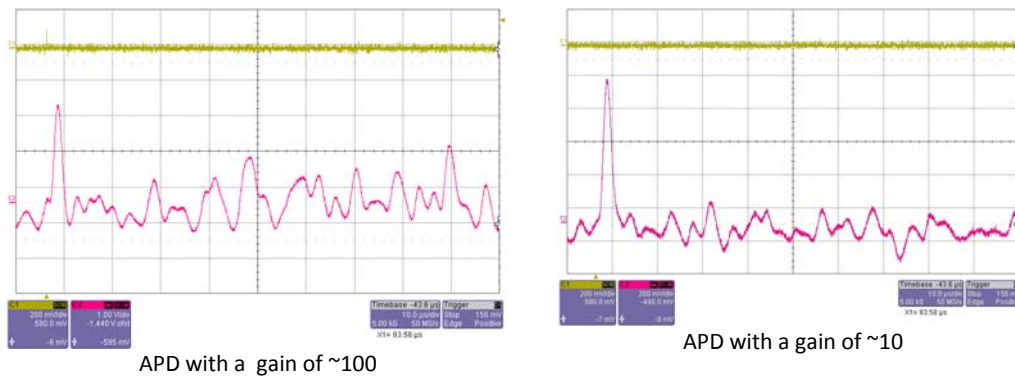


Figure 87. Optical responses of the APD array to the laser pulses at different optical gains.

Attachment of the APD array to the scintillator was accomplished at GE Reuter-Stokes using the optical coupler to adhere the sapphire window to the APD array. Evaluation at GE Research determined that treatment of the APD array surface with a monolayer of a silane coupling agent resulted in satisfactory adhesion of subsequently applied optical coupler. A fixture was assembled at GE Reuter-Stokes, and the assembly was performed by curing the optical coupler in place between the components, using the cure schedule established at GERS. The resulting assembly is shown in Figure 88.



Figure 88. Top view of gamma sensor prototype.

Individual leads were attached to the driver board to carry signals out of the metal housing (Figure 89). In parallel with this, several modifications were made to the cylindrical housing to resolve discrepancies between the housing design and the driver board design. Specifically, the inner diameter of the cylinder was enlarged to accommodate the driver board.



Figure 89. Reverse side of prototype, external wiring attached

Final assembly of the detector was modified on account of the change made to the inner diameter of the housing cylinder, which removed threading. That end of the housing was sealed with Kapton tape, shown in Figure 90. More relevantly, it was determined that a circular driver board matching the I.D. of the cylinder could be designed that would not only eliminate need of the flex interposer, but would also greatly reduce the required volume for the detector.



Figure 90. Completed gamma detector in housing.

Prior to testing the gamma APD detector with scintillator using a gamma source, a dark current of the detector was measured without the gamma source in order to verify a leakage current after housing the electronic board. Figure 91 shows the IV curves of packaged Array 016-M5 measured before and after housing. No significant change was observed that indicated a good insulation of the electrical board.

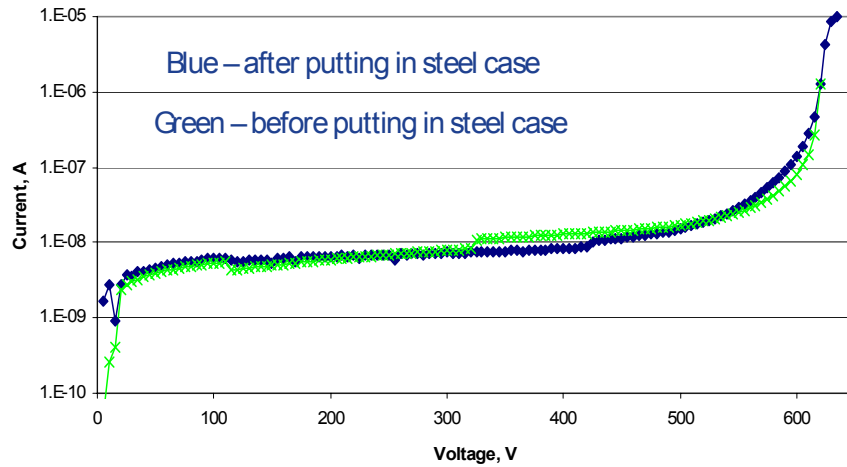


Figure 91. I-V curves of packaged Array 016-M5, before and after housing.

Three prototype units of gamma detector were assembled, two of them (with crystal) were tested with a gamma ray source at room temperature. Schematic drawings of an experimental set-up for testing the gamma detector is shown in Figure 92. Sample of Cs-137 was used as a γ -source. No response signals were detected during testing of the two assembled prototype units of gamma detectors with scintillator crystals.

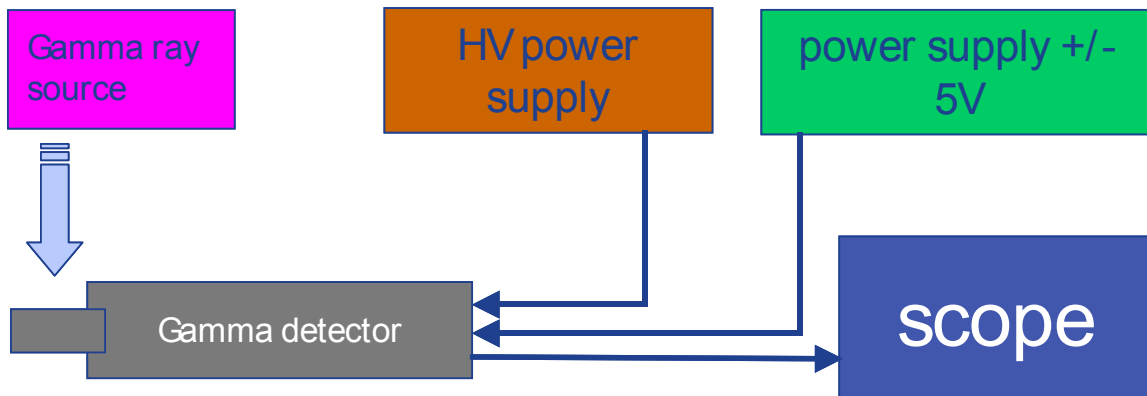


Figure 92. Schematic drawings of an experimental set-up for testing the gamma detector.

Analysis of possible reasons for not detecting a signal from the gamma source showed that detectable minimum of photoelectrons for the SiC APD arrays was 300, while an actual of absorbed photons was 12. Such a low value of can be explained by two key factors: 1) a high density of APD dark current limited an effective area of APD array and, thus, resulted in a low fill factor, 2) the scintillator crystal's light output was too low in the response spectra matching the APD absorption spectra (Figure 93).

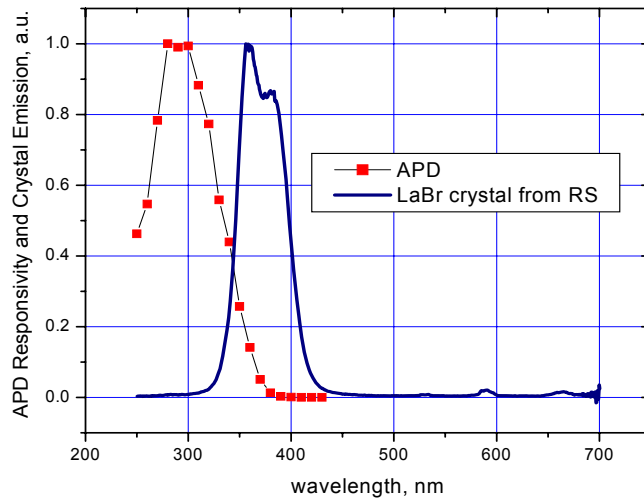


Figure 93. APD responsivity and LaBr_x crystal emission spectra.

8. Task 17 - Suggestions and recommendations for improving performance of the APD gamma sensor

As it was mentioned above, no detection of gamma radiation by the SiC APD detector can be explained by the fact that the detectable minimum of photoelectrons for the SiC APD arrays was 300, while an actual value of absorbed photons was 12. The authors expect that by improving components of the gamma sensor system, namely the SiC APDs as well as the LaX₃ scintillator, GE may revisit the system construction with better results.

This program has provided the means to understand the system model, the system design elements that have yielded success in construction as well as the overall approach to detect gammas at 200 °C. With that in mind, there are several approaches proposed in order to improve a performance of the sensor. These may be used in combination to arrive at the energy resolution requirements initially determined in our voice of the customer sessions conducted early on in the program.

These include:

1. Use a LaCl_3 crystal instead of LaBr_3 crystal as a scintillator material to make a better spectral match of the scintillator crystal's light output and SiC APD response. This will double the number of observable photons to the detector.
2. Use another poly-type of SiC with narrower bandgap (e.g. 3C-SiC) to shift an APD responsivity peak to the longer wavelength range. GE estimations showed that in this case a number of absorbed photons might be increase up to ~ 50 . Note, that a full match of scintillator and APD spectra will give approximately 100 absorbed photons considering an existing design. Thus, additional modification of the system is required to increase a number of collecting photons.
3. Enlargement of a single APD area to 2 mm^2 with sixteen devices per array will result in increase in a number of collecting photons above 300. However, this will result in a significant increase in a dark current due to a high defect density in SiC substrates ($\sim 10^4 \text{ cm}^{-2}$) and, thus, a signal-to-noise ratio will be also significantly reduced. In order to provide a leakage current for 2 mm^2 APDs with at least the same value as obtained in this project for 0.5 mm APDs, a defect density on SiC substrate must be less than $\sim 6 \times 10^2 \text{ cm}^{-2}$. CREE Co., (primary supplier of SiC substrates on market) reported recently at an International conference that they have developed 3" 4H-SiC substrates with median dislocation densities of $1.7 \times 10^2 \text{ cm}^{-2}$ (see a slide from CREE presentation in Figure 94). This opens an opportunity to build large area ($\sim 2 \text{ mm}^2$) 4H-SiC APDs with required low leakage currents.
4. Use a modified signal processing circuit by splitting the array into smaller sections and amplifying and shaping the signals from them separately. Implementing multiplication of multiple separate channels (2,3,4,5) probability of the dark counts can be reduced significantly and detection threshold can be reduced to detect weaker signals. Adding one more channel allows increasing sensitivity 2-3 times.

In the future, the gamma system model may be revisited with the optimized scintillator materials and SiC APDs, and the combined output stands well to enable a down-hole gamma system that was not achieved in this program.

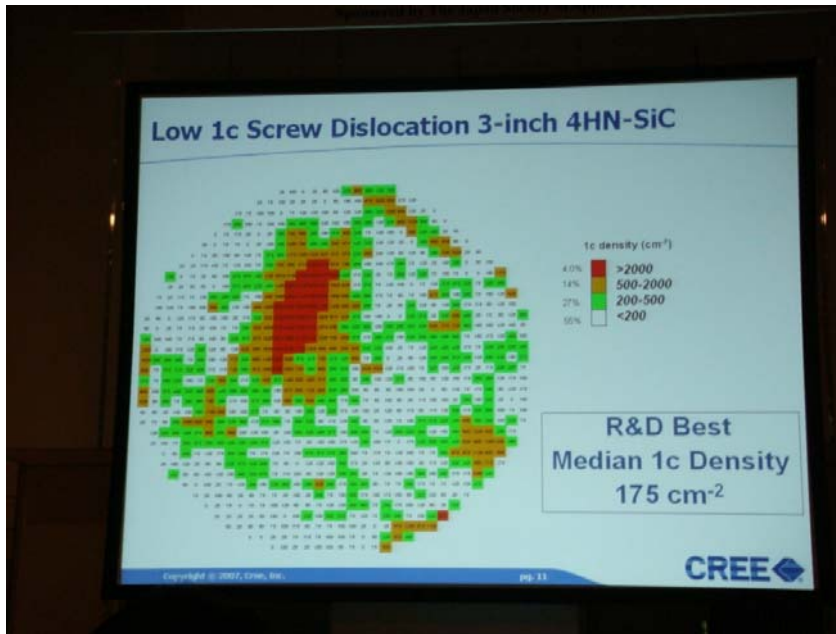


Figure 94. Slide from CREE presentation at last ICSCRM meeting on October, 19 2007 demonstrating development of SiC substrate with a low defect density.

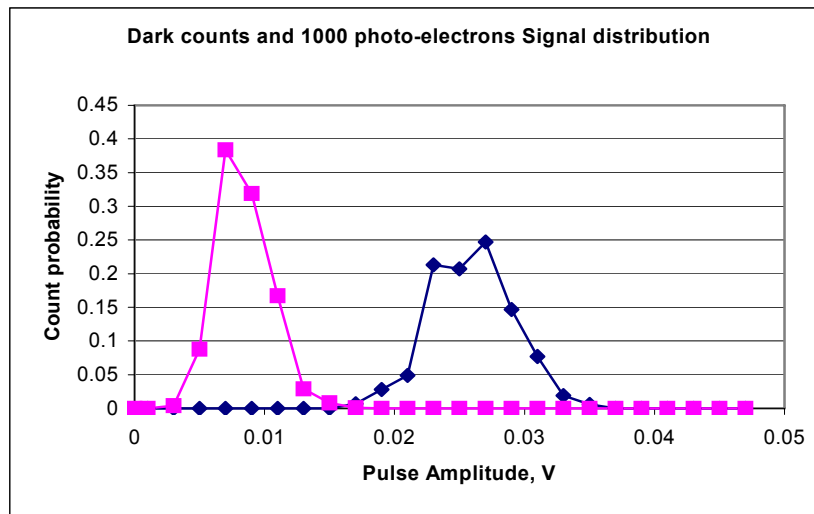


Figure 95. Dark counts and Signal pulse amplitude distribution.

Appendix A - Phase II Statement of Work

Task 8—Fabricate APDs for system development (months 1 - 6)

The recipient shall fabricate a sufficient number of APDs of the optimal design to meet packaging, development, and system demonstration needs. This activity shall focus on growing epitaxial structures and fabricating devices of the optimal design.

Milestone: The completion of >500 optimized 4H SiC APDs for testing (before yield) fabricated from a minimum of 2 SiC substrates. Completed by the end of month 6.

Task 9—Develop APD arrays and device packaging (months 4 - 9)

It is anticipated that SiC material will suffer defect densities that will limit single large device designs for the next 5 years (the material is continually improving). Therefore, APDs will have to be smaller chips arrayed to collect light efficiently from the scintillator crystal. The recipient shall develop matching criteria for chips, design array packaging, engineer layout, and process chips to produce functioning detector arrays for demonstration.

Milestone: The layout design for an array of APDs. The design will be adaptable for a range of array sizes, and will be complimented by task 16. Completed by the end of month 9.

Task 10—Evaluate reliability (months 13 - 18)

The recipient shall conduct a reliability test schedule (both the individual components and the demonstrator prototype). The components shall be tested for 1000 hours at 200° C under operating bias to demonstrate their robustness.

Milestone: A completed reliability test of the APDs and scintillator crystal at 200 °C. The results of this test will be documented in the final report. Completed by the end of phase 2, or month 18.

Task 11—Develop reflector and optical coupling design (months 1 - 6)

The recipient shall optimize the optical coupling of the APD array to the scintillator crystal for light collection efficiency and compatibility of capable materials as part of the detector system design. The recipient shall use its previous experience in UV tolerant optical materials (investigated for UV LEDs).

Milestone: The identification of optical coupling materials (for the UV) and a proposed geometry to facilitate the best possible light transfer from the scintillator to the APD, done in the UV. Completed by month 6.

Task 12—Develop full crystals of selected scintillator material (months 1 - 12)

The recipient shall select an outside vendor to grow single crystals of the selected composition(s) for characterization and use in the detector demonstrator. This task will follow directly from the work in Phase I identifying suitable candidate compounds for the scintillator.

Milestone: Growth attempts at the best candidate scintillator following from phase I efforts. This is intended to result in a good quality scintillator crystal that will be utilized in material studies as well as the final prototype system. Completion by month 12.

Task 13—Assemble and evaluate the full detector system (months 10 - 15)

The recipient shall fabricate and test the full detector assembly as a unit to determine the final performance obtained. As the detector system will be in a laboratory prototype form, testing will be conducted either at GE Global Research or GE Reuter Stokes.

Milestone: A high temperature gamma sensor prototype system will be assembled, which includes the SiC APD, optical coupling materials and arrangement and the best candidate scintillator crystal. Completed by month 15.

Task 14—Demonstrate the detector and issue the final report (months 16 - 18)

The recipient shall demonstrate the detector to DOE in its laboratory form, either at GE Global Research or GE Reuter Stokes and issue a report documenting the measured performance specifications.

Milestone: The most suitable test facility will be selected from GE Research and GE Reuter-Stokes. The test will evaluate the APD, optical coupling materials and scintillator in operation at temperatures up to 200 °C. Completed by the end of phase 2, or month 18.

Deliverable - 18 months: Complete report summarizing progress made in all areas of the program, including recommendations for continued work in this area.

Task 15—Project management (months 1 - 18)

The recipient shall provide the necessary project management support over the 18 months of Phase II.

Milestone: Monthly reports will be provided along with other appropriate documentation or samples as requested by the Department of Energy. This general task will run throughout the entire phase 2 effort.

Task 16— Identify electronic components and develop prototype amplification system (months 4 - 12)

The recipient shall design an electronic amplification system for use with the prototype system. This will be implemented for system testing with the electronics tested up to

150 C. Further, the recipient will identify necessary components for operation at 200 °C for future use.

Milestone: An electronic circuit approach will be identified in order to accommodate the operation of an array of APDs as described in task 9. We anticipate completion of this design work by month 12.

Task 17— Commercialization Plan (month 18)

The recipient shall provide the details for where system components will be manufactured, and the preferred plan as to how it will be taken to commercialization.

Milestone: At the end of phase 2, the GE team will review progress in order to generate a commercialization plan for the high temperature gamma sensor system. This will be included with the final phase 2 report, and will include recommendations for future work pending the level of success.

Appendix B – List of Publications

The following publications resulted from the work done under this program:

1. **"Observation of Luminescence from Defects in 4H-SiC APDs Operating in Avalanche Breakdown"**, S. Soloviev, P. Sandvik, A. Vertiatchikh, and Ho-Young Cha, presented at the International Conference on Silicon Carbide and Related Materials (2007).
[paper accepted for the ICSCRM Proceedings, 2007]
2. **"Comparison of 4H-SiC Separate Absorption and Multiplication Region Avalanche Photodiodes Structures for UV Detection"**, Ho-Young Cha, Stanislav Soloviev, Greg Dunne, Larry Rowland, Scott Zelakiewicz, Peter Waldrab and Peter Sandvik, to be published in the *Proceedings of the 2006 IEEE Sensors Conference* (2006).
[paper presented at the IEEE Sensors Conference, Deagu, Korea, 2006]
3. **"Study of Dark Currents in 4H-SiC UV APDs with Separate Absorption and Multiplication Regions"**, Stanislav Soloviev, Ho-Young Cha, James Grande and Peter Sandvik, *Materials Science Forum*, Vols. **556-557**, p. 953-956 (2007).
[paper presented at the European Conference on Silicon Carbide and Related Materials Meeting, Nottingham, United Kingdom, 2006]
4. **"Next Generation Gamma Sensor for High Temperature Drilling"**, Peter Sandvik, Jack Colborn, James Williams and David O'Connor, in *GasTIPS Magazine*, Vol. **12**, No. 2, p. 10-12 (2006).
5. **"SiC Photodetectors for Industrial Applications,"** Peter Sandvik, Kent Burr, Stanislav Soloviev, Stephen Arthur, Kevin Matocha, James Kretchmer, Leo Lombardo and Dale Brown, in the *Proceedings of 2005 IEEE Lasers and Electro-Optics Society Meeting*, p. 302-303 (2005).
[invited paper presented at the IEEE Lasers and Electro-Optics Society Meeting, Sydney, Australia, October, 2005]

National Energy Technology Laboratory

626 Cochrans Mill Road
P.O. Box 10940
Pittsburgh, PA 15236-0940

3610 Collins Ferry Road
P.O. Box 880
Morgantown, WV 26507-0880

One West Third Street, Suite 1400
Tulsa, OK 74103-3519

1450 Queen Avenue SW
Albany, OR 97321-2198

539 Duckering Bldg./UAF Campus
P.O. Box 750172
Fairbanks, AK 99775-0172

Visit the NETL website at:
www.netl.doe.gov

Customer Service:
1-800-553-7681

